Fuel 332 (2023) 125905

Contents lists available at ScienceDirect

Fuel

journal homepage: www.elsevier.com/locate/fuel

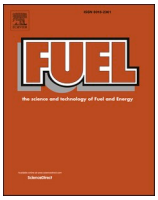

A comprehensive review of hydrogen generation by water splitting using 2D nanomaterials: Photo vs electro-catalysis

Fares Almomani [a,*], Amani Al-Rababah [a], Muhammad Tawalbeh [b,c], Amani Al-Othman [d]

[a] Chemical Engineering Department, Qatar University, Qatar
[b] Sustainable and Renewable Energy Engineering Department, University of Sharjah, P.O. Box 27272, Sharjah, United Arab Emirates
[c] Sustainable Energy & Power Systems Research Centre, RISE, University of Sharjah, P.O. Box 27272, Sharjah, United Arab Emirates
[d] Department of Chemical Engineering, American University of Sharjah, P.O. Box 26666, Sharjah, United Arab Emirates

ARTICLE INFO

Keywords:
Hydrogen evolution reaction (HER)
Water splitting
MXene
Photo-catalysis
Electro-catalysis

ABSTRACT

Transition metal carbides/nitrides (MXenes) with eccentric properties are emerging 2D nanomaterials with intriguing applications in the photo and electro-catalytic water splitting (W*sp*). MXenes have a regular planer structure with a large specific surface area (SSA), excellent hydrophilicity, metallic conductivity, and a wide range of functionalities and surface termination groups, making them a promising candidate for long-term hydrogen generation ($H_{2,\ gen}$). As a result, their use as electro and photo-catalysts in W*sp* to solve energy and environmental challenges has increased. MXenes were proposed to overcome major drawbacks of TiO_2, the most commonly used photo-catalyst in solar-driven W*sp*, such as high band gap and fast recombination of photo-induced charge carriers. MXene has been rigorously investigated based on TiO_2 modification (i.e. in-situ derived MXene-TiO_2 and MXene/TiO_2 nanocomposite) as well as Metal-MXene co-catalyst that provides simple electron channelization to improve overall electro and photo-catalytic activity (Cat_A)toward W*sp* and increase the hydrogen evolution reaction (HER). However, several issues must be resolved before practical applications may be considered, such as weak environmental capabilities and limited intrinsic catalytic activities. Although there have been a few review papers on the synthesis, properties, and applications of Mxenes in various fields, this present work focuses on the most current advances in the synthetic of MXene-derived TiO_2 and MXene/TiO_2 nanohybrid composites as well as Metals-MXene nanocomposite, clarifying the charge carrier separation mechanism in connection to the formed Schottky junction at MXene- elements interface to attaining high photo-catalytic $H_{2,\ gen}$. Furthermore, technical challenges, and enhanced catalytic performance as well as materials design and MXenes derivative with structural features and activity were presented. MXenes' catalytic mechanism is carefully outlined, along with its photocatalytic and electrocatalytic W*sp* properties. According to the literature review, Ti_3C_2 can be combined with a variety of materials to produce electro or photo-catalysis with distinct layered morphology (0D, 1D, 2D, 3D), abundant surface termination groups, and enhanced photo-electrical activities. MXene-derived TiO_2 and MXene/TiO_2 nanohybrid composites have been proposed as viable electro and photo-catalytic $H_{2,\ gen}$ alternatives. The photo-catalytic $H_{2,\ gen}$ rate from W*sp* over MXene-derived TiO_2 can range from 20 to 50, 000 $mol.g^{-1}h^{-1}$, with Co-Chl@Ti_3C_2Tx producing the most.

1. Introduction

Globally, rising energy demand has increased the consumption of fossil fuels, which is problematic given their limited supply and the significant environmental risks they pose. Wind, solar, and hydroelectric power have all been promoted as viable and environmentally friendly alternatives to fossil fuels in recent decades [1,2]. Yet, there are restrictions on the distribution of these ecologically favorable resources over time, making the creation of highly effective energy conversion and storage technologies crucial [3,4]. Hydrogen, a high-energy–density, low-carbon fuel, has been identified to be a viable medium for storing energy produced from these renewable resources[5,6]. Hydrogen is considered a promising fuel for the future [7]. Because of their cost-effectiveness and environmental sustainability, electro and photo-catalytic W*sp* have great potential among the numerous $H_{2,\ gen}$ technologies[8].

* Corresponding author at: Department of Chemical Engineering, College of Engineering, Qatar University, P. O. Box 2713, Doha, Qatar.
E-mail address: Falmomani@qu.edu.qa (F. Almomani).

https://doi.org/10.1016/j.fuel.2022.125905
Received 12 May 2022; Received in revised form 26 August 2022; Accepted 4 September 2022
Available online 14 October 2022

The HER and the oxygen evolution reaction (OER) are two half-reactions that are involved in the electro-catalytic W*sp* reaction [9–11]. In the HER, the type of electro-catalyst plays an important role in $H_{2,\ gen}$. In general, noble metal-based electro-catalysts (e.g. Ru, Ir, and Pt) were used in such applications as they exhibit high stability and excellent efficiency [9–13]. The ever-growing demand for noble metals electro-catalysts, on the other hand, has been hampered by supply constraints and increasing costs. As a result, developing low-cost, high-efficiency W*sp* catalysts is critical Three major steps are commonly involved in the photo-catalytic W*sp*: (1) light absorption by the photo-catalyst, resulting in the formation of electron-hole pairs; (2) charge transfer to the surface of the photo-catalyst; and (3) hydrogen generation ($H_{2,\ gen}$.) at the catalyst-electrolyte interface [14,15]. Charge separation and transfer are the rate-controlling stage of the photo-catalysis process. This is because electron transport is slow and electrons and holes can easily recombine. Therefore, the efficiency of photo-catalysis and solar conversion are severely limited [14–16]. Consequently, the discovery and development of highly efficient photo-catalytic materials with fast charge transfer dynamics and low electron/hole pair recombination has emerged as the primary research focus of the photo-catalytic W*sp* process [14–16].

A widely studied photo-catalyst, such as CdS, exhibits outstanding photo-catalytic performance and has demonstrated promising outcomes for photo-catalytic $H_{2,\ gen}$. throughout the years. Such a single photo-catalyst, though, has low electron-hole pair separation efficiency and is susceptible to photo-instability and photo-corrosion. CuO and ZnO, on the other hand, have been claimed to be good photo-catalysts for the production of hydrogen due to their availability, affordability, and nontoxicity. Nonetheless, their limited ability to absorb light under natural sunlight irradiation range restricts their large-scale applications for H_2 generation. To overcome the limits of solar-active semiconductors and switch to the spectrum of natural sunlight, improvements including morphological tuning, architectural designs, and bandgap engineering through the development of hybrid composites have frequently been proposed.

Two-dimensional (2D) materials have attracted increasing research interest as co-catalysts to improve photo-catalytic $H_{2,\ gen}$. since the discovery of monolayer graphene in 2004 [17,18]. Transition metal dichalcogenides (such as MoS_2 [19], WS_2 [20], g-C_3N_4 [21,22], layered double hydroxides (LDHs) [23,24]), are just a few examples of 2D materials that have good catalytic [25,26], electrical [27,28], and opto-electronic characteristics [29–31]. Furthermore, the 2D shape shortens the distance between charge carriers and the reaction site [32], which prevents charge carrier recombination and thus improves photo-Cat_A [33].

In 2011, Naguib et al. [34] discovered the 2D nanosheets ($Ti_3C_2T_x$) for the first time. The structure is composed of Ti_3C_2 layers and conical scrolls and is produced at room temperature. The excellent qualities of various MXene types, such as high levels of chemical and structural stability, high electrical conductivity, and wide SSA have led to an increased interest in these compounds [34–36]. Other layered compounds with similar properties to Ti_3C_2 were synthesized and studied shortly after. The precursors of $M_{n+1}AX_n$ (where n ranged from 1 to 3) are typically etched to form $M_{n+1}X_nT_x$, where M is a transition metal (e.g., Mo, Ta, and Ti), A is any elements from groups 13 and 14 of the periodic table, X is carbon and/or nitrogen, and T_x is any functional group of ^{-}OH, ^{-}H, ^{-}F, etc., [37–40]. So far, >30 MXene compounds, Ti_3C_2, Ti_2C, Ti_4N_3, Mo_2C, and Ta_4C_3, among others, have been successfully produced and used in a wide range of applications. In the realms of renewable energy and the environment, MXene has recently attracted a lot of attention as an electro-catalyst or photo-catalyst. In specific, many research projects have used MXenes as electro and photo-catalysts in the W*sp* process.

In this study, the recent achievements in MXene synthesis, technical limitations, and catalytic performance enhancement are discussed. The insights gained from tailoring the surface functional group of MXene via various synthesis processes are discussed. The role of MXenes in promoting electro and photo-catalytic W*sp* is constantly discussed, emphasizing the recent progress in this field. Furthermore, insights into different MXenes' catalytic mechanisms in terms of electro and photo-catalytic W*sp* are summarized. Lastly, future research directions and advancements in photo and electro-catalysts based on MXenes were presented.

2. Methodology

This review provides an overview of the findings from research works between 2010 and 2022, which focused on synthesis, technical limitations, and the use of MXene in promoting electro and photo-catalytic $H_{2,\ gen}$. via W*sp*. Two important articles published in 2004 and 2005 were also considered as they presented crucial data. Approximately, 176 articles were searched from science direct, Web of Science, Google Scholar, Scopus and ProQuest databases, with 142 relevant articles kept, and 34 discarded. The keywords used in the search were "hydrogen evolution", "electro-catalysts", "water splitting", "Layered catalysis.", "two-dimensional transition metal.", "nanocomposites.", "hetero-structured electro-catalyst.", "Hydrogen evolution reaction.", "MXenes.", "photo-catalysts." and "Layered catalysis.". The literature review is focused on the different synthesis methods of MXene as presented in section 3, the role of MXene in promoting electro and photo-catalytic $H_{2,\ gen}$. as presented in section 4. This section also includes electro-catalytic and photo-catalytic waster splitting as well as the factors affecting each process. Finally, section 5 summarizes the conclusion and future research direction on this topic.

3. Synthesis of MXenes

Mxenes are generally synthesized from the MAX phase by etching, which results in the formation of different surface functional groups (-O, -H, –OH, -T_x) on the surfaces [39]. To obtain freely swinging bonds on the surface of Mxenes, the A layer is removed during the etching process [41]. The terminal groups can bond to a vast range of functional groups, dictating the surface properties [41,42].

Combining Mxenes and other nanomaterials has been an effective way to synthesize Mxenes-based and Mxenes –derived nanocomposites and has been considered highly efficient electro-catalysts or photo-catalysts for W*sp*. In the electro-catalysis process, Mxenes are frequently used in conjunction with Nobel metals or as a substrate to form hetero-structures such as Ru [43], CdS [44], ZnO, ZnS [45], g-C3N4 [46,47], Pt [48], metal selenide [49], ZnS/Ti3C2 [50], MoS2 [51] and nickel [52]. In the photo-catalysis process, Mxenes tend to compiled with other semiconductors, such as CdS [44], TiO2 , MoS2 [51], ZnO, ZnS [45], g-C3N4 [46], PtO, HCN [54]. Mxenes-based and Mxenes-derived nanocomposites are typically synthesized using a variety of procedures such as solvothermal treatment, hydrothermal, mechanical/ultrasonic mixing, calcination and electrostatic self-assembly.

The following sections present different synthesis methods used for the development of high-performance novel photo and electro-catalysts based on Mxenes. Only the most common methods for Mxenes-based and Mxenes-derived catalysts are covered here in this part.

3.1. Hydrothermal synthesis (HT_S)

The HT_S method is the process of heating and pressurizing the reaction system with water in a special sealed container to create a high temperature and high-pressure reaction environment [15,47]. The H_S offers many benefits, such as a one-step synthetic procedure, relatively mild operating conditions, environmental friendliness, and good diffusion in solution [15,47]. Comparable to other preparation techniques, the HT_s method has a low cost in terms of quantities of raw materials, instruments, and energy needed. Furthermore, the produced materials by the HT_s method are highly pure and controlled morphology [47]. As a

result, this method has been considered a magnificent method to synthesize Mxenes-based catalysts. For example, the CdS-MoS_2-MXene photo-catalyst was manufactured by Chen et al. using a simple HT_s method [48]. Fig. 1 presents the procedure used in the synthesis of CdS-MoS2-MXene by the HT_s method. In such a process, a solution prepared by dissolving 0.3 g MoS_2 in 20 mL of water was ultrasonically dispersed. Then, the solution is mixed with 0.006 g of as-prepared MXene under continuous stirring for 30 min. Later, 2.065 g Cd $(CH_3COO)_2{\cdot}2H_2O$ and 1.4235 g CH_4N_2S were gently poured into the solution and stirred for 30 more minutes until completely dissolved. The obtained solution was then autoclaved and heated up to 160 °C for a period of 24 h. The final product was washed with ethanol and deionized water and left to dry overnight. The prepared CdS-MoS_2-MXene photo-catalyst showed high HER performance when exposed to visible light. In terms of electro-catalytic W*sp*, the unique architecture of (3D) $MoSe_2$/MXene hybrid nanoflowers with high stability and good conductivity was developed by Huang et al. [49] using a simple HT_s method. In this situation, the $MoSe_2$ is grown in situ on the ultrathin MXene. The procedure which is presented in Fig. 2 consists of dissolving 0.17 mmol of $(NH_4)6Mo_7O24$ and 2.4 mmol SeO_2 powder in 15 mL followed by 30 min of ultrasonic treatment. The homogenous mixture was then added to 25 mL of ethanediamine that was vigorously stirred for 15 min at ambient temperature. The produced material was autoclaved for 20 h at 200 °C in a 40 mL stainless-steel autoclave lined with Teflon, after which it was cooled down and centrifuged at 8000 rpm to collect the black precipitates. The products were then washed with ethanol and distilled water and dried at 60 °C. To generate the final product, the collections above were annealed in a flowing N_2 environment for 1 h at 500 °C. The obtained hybridized unique 3D $MoSe_2$/MXene nanoflowers enhanced large spaces for the exchange of ion–electron exchange and raised the number of active sites, which resulted in a good HER performance [49]. Furthermore, using $Ti_3C_2T_x$ nanosheets, an improved 3D Ru/MXene electrode with super hydrophilicity and superhydrophobicity is fabricated on porous Ni foam by the HT_s method [43]. A similar procedure was used to prepare Ru/c-Ti3C2Tx/NF electrode as shown in Fig. 3. In such procedure, 10 mL of the suspended $Ti_3C_2T_x$ was subjected to ultrasonication for 10 min. After that, the suspension was ultrasonically treated for 2 h with 20 mg of $C_{19}H_{42}BrN$ to generate c-$Ti_3C_2T_x$ nanosheets suspension. Then NF was immersed in the c- $Ti_3C_2T_x$ suspension, and heated at 130 °C for 4 h in a conventional Ru/c- $Ti_3C_2T_x$ /NF synthesis. The as-prepared c- $Ti_3C_2T_x$ /NF was then cleaned and dried for 2 h at 50 °C. The c- $Ti_3C_2T_x$ x/NF was then immersed in an ethylene glycol/H_2O solution with $RuCl_3$ of varying concentrations in a hydrothermal reaction for 3 h at 130 °C. Afterward, Ru/c-$Ti_3C_2T_x$/NF was washed repeatedly with ethanol and deionized water. The Ru/c-$Ti_3C_2T_x$/NF obtained showed outstanding W*sp* and HER performance [43].

3.2. Solvothermal synthesis (ST_S)

The ST_S method is a method by which chemical compounds are produced in the same manner as the hydrothermal route. Only organic solvents are used instead of aqueous solutions. The ST_S method has been recognized as an important approach used for the preparation of MXene-derived and MXene-based nanocomposites with different morphologies. For instance, Tie et al. [50] fabricated ZnS/Ti_3C_2 photo-catalyst by the solvothermal reaction. The procedure involves the preparation of a suspension of 0.02 mol TAA in 50 mL of the ethanol-glycerol at room temperature using a magnetic stirrer for 5 min. Afterward, a known amount of Ti_3C_2 nanosheets and 0.01 mol of $ZnCl_2$ dissolved in water were added to the suspension. The obtained solution was then autoclaved at 180 °C for 10 h. After cooling, the product was rinsed thrice alternately with alcohol and deionized water. The resulting sample was kept at 60 °C to dry and attain the final product. The charge transfer is aided by decorating the ZnS nanoparticles in situ with Ti_3C_2 nanosheets, which increases the efficiency of H_2 generation [50]. The 1D CdS/2D Ti_3C_2 MXene nanocomposites are synthesized easily through the ST_S method [51]. A certain amount of ultrathin Ti_3C_2 MXene nanosheets dissolved in 30 mL ethanediamine was ultrasonicated for 3 h to obtain a homogenous solution. Another solution consisting of 4.62 g of Cd $(NO_3)_2{\cdot}4H_2O$ dispersed in 20 mL of ethanediamine was prepared. The second solution was added dropwise into the homogenous solution that contains Ti_3C_2 MXene nanosheets, and the obtained mixture was left to settle overnight under stirring at room temperature. A third solution of 3.43 g of thiourea dissolved in 22 mL of ethanediamine was prepared. The third solution was gently added into suspension while stirring for 2 h. The mixture was then transferred into a 100 mL autoclave (Teflon-lined), and continuously heated for 48 h at a temperature of 160 °C. Following centrifugal separation and several rinsing with ethanol and deionized water, the product is obtainable after cooling. Lastly, the product was collected after drying in a vacuum for 12 h. The hybrid material obtained shows excellent photo-catalytic HER activity, while the metallic Ti_3C_2 nanosheets provide excellent electron and ion shuttles. The FeNi@$Mo_2TiC_2T_x$@NF hybrid bifunctional electrocatalyst was made using a mix of ST_S and annealing methods, with nickel as the Ni source and substrate [52]. Commercial NFs (1 cm × 1.5 cm) were

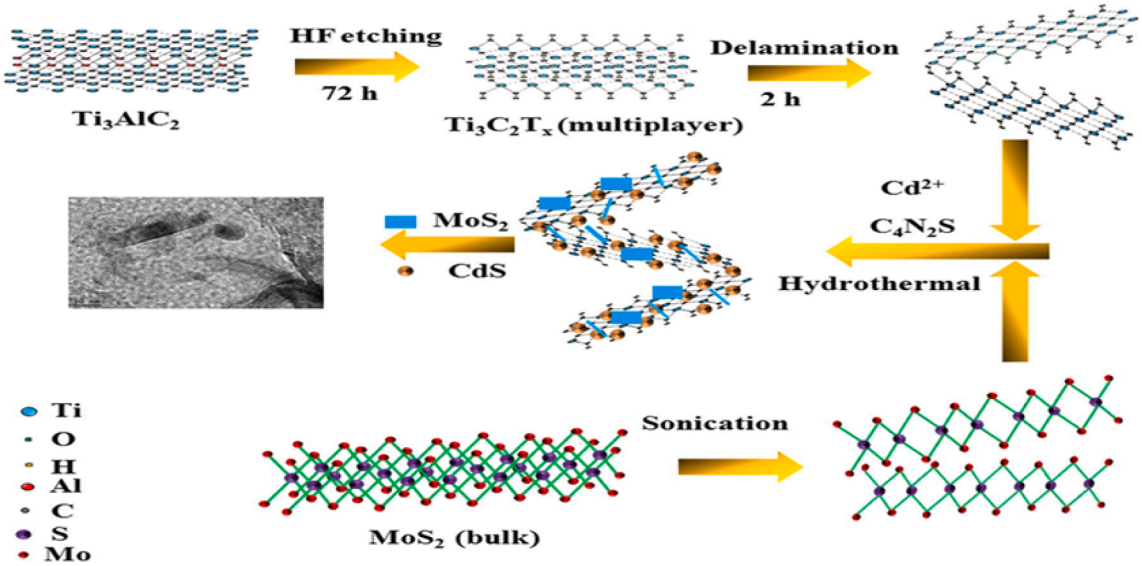

Fig. 1. Hydrothermal (HT_s) method to prepare CdS-MoS_2-MXene by [48].

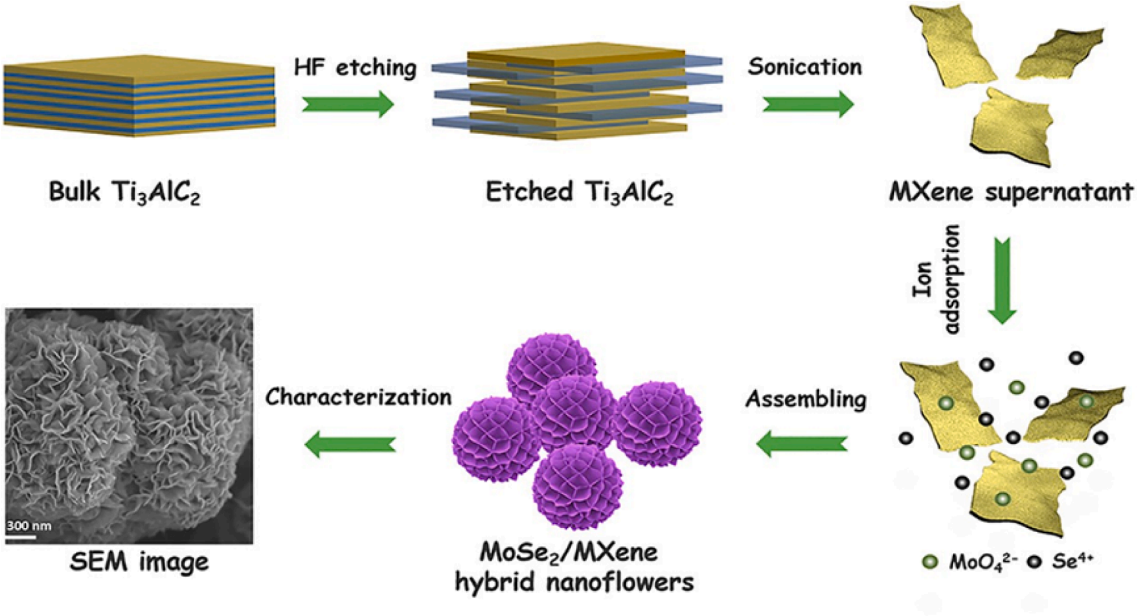

Fig. 2. Schematic of the synthesis route of $MoSe_2$/MXene hybrid nanoflowers. Reprinted with permission from Ref. [49].

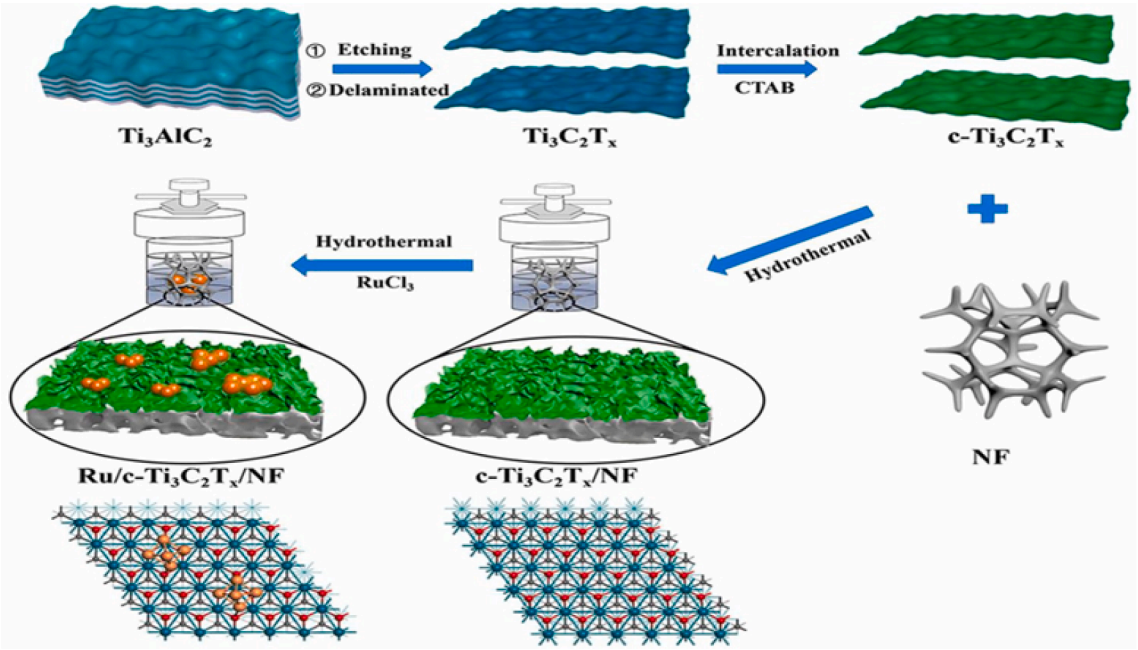

Fig. 3. Steps used for the synthesis of a Ru/c-$Ti_3C_2T_x$/NF electrode. Reprinted with permission from Ref. [43].

treated for 20 min with a 6 M strong HCl solution, then rinsed numerous times with distilled water and acetone. A 38 mL ethylene glycol and 2 mL 125 mM solution of NaOH was produced respectively, and 100 mg $Mo_2TiC_2T_x$ MXene was scattered in it. The mixture was sonicated for 30 min. After that, the treated NF and the suspension were autoclaved for 18 h at 140 °C. In addition, after naturally cooling the autoclave to ambient temperature, the product desiccated for 2 h at 80 °C. 71.2 mg of ferrous chloride tetrahydrate ($FeCl_2{\cdot}4H_2O$) was added to 200 μL of $Mo_2TiC_2T_x$ MXene@NF, and 1 mL ethanol was added simultaneously. After that, the MXene@NF was dried under vacuum at room temperature and annealed for 2 h at 550 °C in a percent H_2/N_2 atmosphere. FeNi@$Mo_2TiC_2T_x$@NF, as obtained, has outstanding electro-catalytic HER performance and shows an excess of 160 mV overpotential (**η**) with a current density (J_A) of 10 mA/cm^2 and small Tafel slope (T_s) of 103.46 mV.dec^{-1}. A large amount of surface active sites and high activity resulted from the electrical interaction between $Mo_2TiC_2T_x$ MXene distributed over FeNi NPs and nickel foam. On the Mo sites of $Mo_2TiC_2T_x$, HER is more likely to develop due to synergistic impact of $Mo_2TiC_2T_x$ and FeNi NPs, and because of this, it can served as a bi-functional electro-catalyst. It can drive W*sp* in alkaline solutions, for example, indicating that it could be used to generate renewable energy.

3.3. *Electrostatic self-assembly and mechanical/ultrasonic mixing*

The most basic method for producing MXene-based hybrids was mechanical mixing. The samples were created by either combining the two components in a liquid phase or using grounding forces. Surprisingly, the surface functional groups created during the etching

procedure result in additional negative charges on the surface of the MXenes. It provides the basis for electrostatic self-assembly to take place [53–56]. Electrostatic self-assembly was used to create TiO_2/Ti_3C_2 composites [55]. In distilled water, a particular amount of TiO_2 NFs was spread and sonicated for one hour. After that, 10 mg of Ti_3C_2 nanosheets were sonicated for 1 h in 10 mL distilled water. The TiO_2 solution was then put into the Ti_3C_2 solution in a homogenous state. The mixture was then continuously agitated for 12 h. Finally, the TiO_2/Ti_3C_2 powder was washed thrice with distilled water before being dried for 24hrs at 80 °C, as shown in Fig. 4. The TiO_2/Ti_3C_2 acts as a photo-catalyst for $H_{2,\ gen.}$ at a maximum rate of6.979 mmol h^{-1} g^{-1}, which is 3.8 times higher than pure TiO_2 nanofibers (NFs). The increase in photo-catalytic $H_{2,\ gen.}$ using TiO_2/Ti_3C_2 is due to the heterogeneous interface between Ti_3C_2 and TiO_2 NFs nanosheets. Additionally, *In-situ* electrostatic assembly was used to synthesize the Schottky-junction of Ti_3C_2 MXene/O-doped g-C_3N_4 [54] as indicated in Fig. 5. The bulk g-C_3N_4 (also known as CN) was created first. The O-doped CN nanosheets were made by calcining the CN at 550 °C for 1 hr. Thereafter, 300 mg of protonated O-doped g-C_3N_4 nanosheets (known as HCN) were dissolved ultrasonically in 30 mL DI water and mixed for 3 h. After that, a precise amount of Ti_3C_2 MXene nanosheets solution was put into the HCN solution and stirred for another 12 h. The resultant sample was washed and dried at 80 °C. The Ti_3C_2 MXene/O-doped g-C_3N_4 Schottky-hydrogen junction's evolution rate was increased to 25124 mol/g/h compared to 15573 μmol h^{-1} g^{-1} generated by pristine Ti_3C_2 MXene/pristine C_3N_4 and 13745 μmol h^{-1} g^{-1} generated by O-doped g-C_3N_4. The improved photo-catalytic performance is linked to the synergy effect of intimate 2D/2D interfacial contact and the Schottky-junction construction that decrease the charge transport distance and enhance the photo-generated charge.

3.4. Hydrothermal oxidation (HT_O)

The HT_O method, which is most typically used in synthesizing the MXene-derived photo-catalysts by in-situ oxidation of the MXene precursors, can be used to entirely or partially oxidize MXenes into TiO_2/MXene or TiO_2 composites. As an example, Peng et al. [57] fabricated Cu/TiO_2@$Ti_3C_2T_x$ photo-catalyst by the HT_O method. Fig. 6 shows the Cu_y/TiO_2@ $Ti_3C_2T_x$ synthesis technique. In summary, the HT_O method forms TiO_2 nanosheets on $Ti_3C_2T_x$, which is followed by copper species' in-situ photo-deposition. In the first step, 100 mg TiO_2@ $Ti_3C_2T_x$ has added to 10 mL deionized water and 100 % 190 mL ethanol. The required amount of Cu/$2H_2O$ was added and was dispersed ultrasonically for 30 min. Then, the suspension was stirred. After which the powder was filtered and dried in a vacuum. In the TiO_2@ $Ti_3C_2T_x$ composite, the percentage weight of Cu was developed as y percent TiO_2. Cu_y/ TiO_2@ $Ti_3C_2T_x$ (y = 1, 2, 4, 6, and 10) are the photo-catalysts obtained. The Cu/TiO_2@ $Ti_3C_2T_x$ photo-catalyst showed an excellent W*sp* efficiency and generated hydrogen at a rate of 860 μmol $g^{-1}h^{-1}$.

The production of peculiar 2D-2D-2D composite via the HT_O method of Ti_3C_2@TiO_2@MoS_2 is shown in Fig. 7 [58]. The preparation procedure includes two aqueous solutions. The first includes 15 mg of $Na_2MoO_4{\cdot}2H_2O$ dissolved in 20 mL of water, and the other contains 30 mg CN_2H_4S in 20 mL of deionized water. The two aqueous solutions were mixed to generate a clear solution. After that, 60 mg of Ti_3C_2@TiO_2 composites were mixed with the solution above and stirred to produce the suspension of Ti_3C_2@TiO_2@MoS_2 composite. This was followed by hydrothermal treatment of the composite for 24 h at 200 °C in a 25 mL stainless-steel autoclave (Teflon-lined). The composite was then cooled down to ambient temperature, collected by vacuum filtration, thoroughly washed with distilled water, and left to dry in a vacuum oven for 12 h at 50 °C. The HER activity of this photo-catalyst was substantial with a rate of 6425.297 μmol $g^{-1}h^{-1}$.

3.5. Calcination

Calcination is a method of heating a substance at a regulated temperature in a controlled environment. It is often used to synthesize g-C_3N_4 photo-catalysts and electro-catalysts (See Fig. 8). one-step calcination process was used to create the g-C_3N_4/Ti_3C_2 hybrids [59]. In this procedure, 3 g of melamine powder was suspended in 100 mL of deionized water and agitated for 3 h at 60 °C. After cooling the suspension to ambient temperature, 0.5 g of Ti_3C_2 was added to the resulting solution and mixed for 0.5 h to properly disperse Ti_3C_2 powder. Then, the temperature was set at 100 °C until the solution dried. Furthermore, the g-C_3N_4/Ti_3C_2 composite was subjected to thermal annealing for 2 h at 550 °C at a rate of 5 °C min¯1 under nitrogen. The g-C_3N_4 strongly interacts with Ti_3C_2, and the resulting composites show an increase in charge separation efficiency compared with pure g-C_3N_4. The rate of generation of photo-catalytic H_2 of the optimized g-C_3N_4/Ti_3C_2 composite was thrice higher than pure g-C_3N_4. Another hybrid composite of $TiO_2C@CN_x$ was developed by He et al. [60] through the calcination of melamine–cyanuric acid and $Ti_3C_2T_x$ at separate temperatures. The Hybrid $TiO_2C@CNx,_{950}$ (produced by calcination at 950 °C) displays excellent electro-Cat_A for HER due to the use of a combination of the high electro-catalytic performances of TiO_2 nanoparticles and superior electrochemical activity of the graphene-like nanostructure. The HER which was carried out in a 0.1 M KOH solution and showed that the $TiO_2C@CN_{x,950}$ required low **η** and J_A of − 254.5 mV and 10 mV cm^{-2}, respectively with a small value of $T_s \approx 60$ mV dec^{-1}, which is less than most of the metal oxide catalysts. Fig. 9 presents the preparation of trifunctional electro-catalysts TiO2C@CN_x nanosheets that can be effectively used for HER, OER, and ORR. The procedure involves thermal treatment of the MCA@$Ti_3C_2T_x$ composite

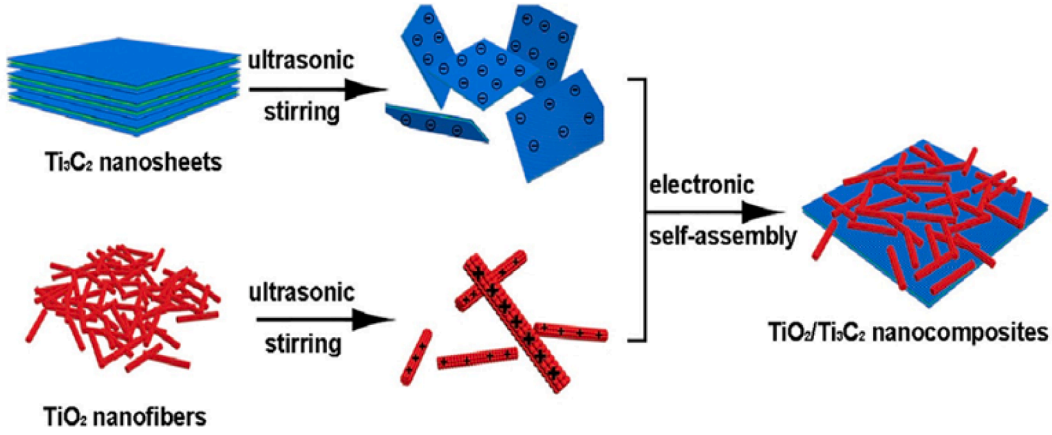

Fig. 4. Schematic of the formation of Ti_3C_2/TiO_2 nanocomposites. Reprinted with permission from Ref. [55].

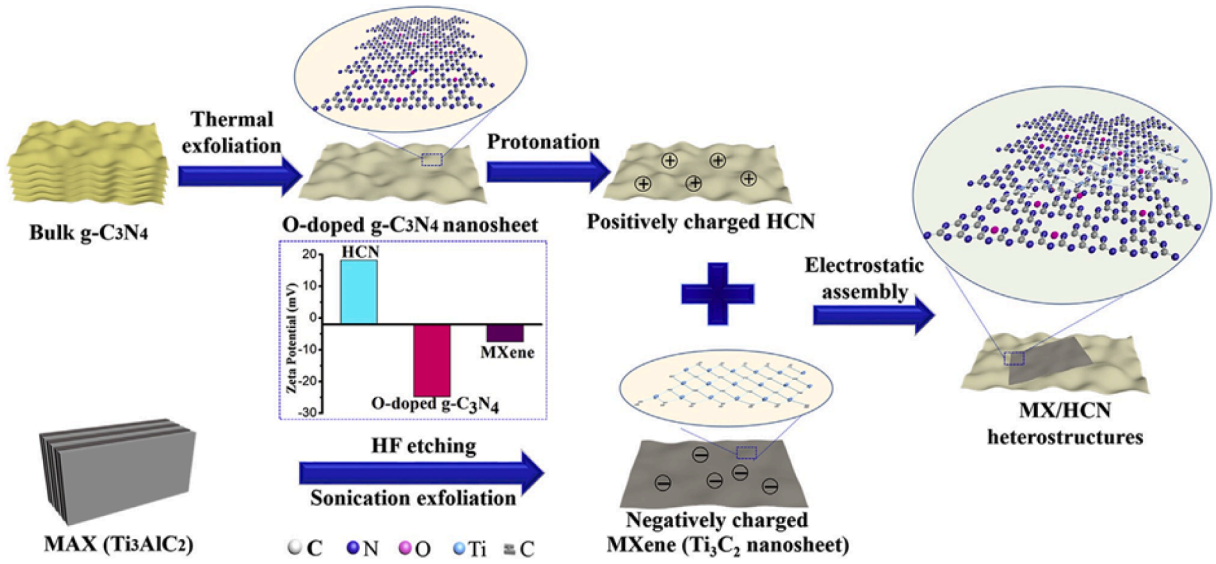

Fig. 5. The procedure used in the preparation of 2D/2D MX/HCN Schottky-junction. Reprinted with permission from Ref. [54].

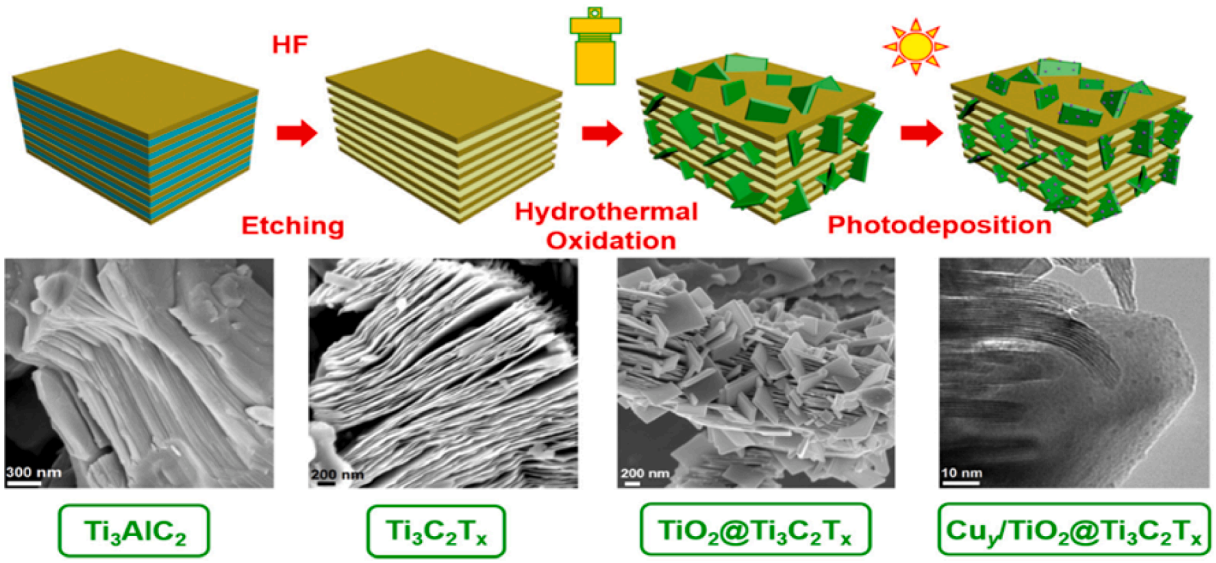

Fig. 6. Schematic of the preparation of $Cu_y/TiO_2@Ti_3C_2T_x$. Reprinted with permission from Ref. [57].

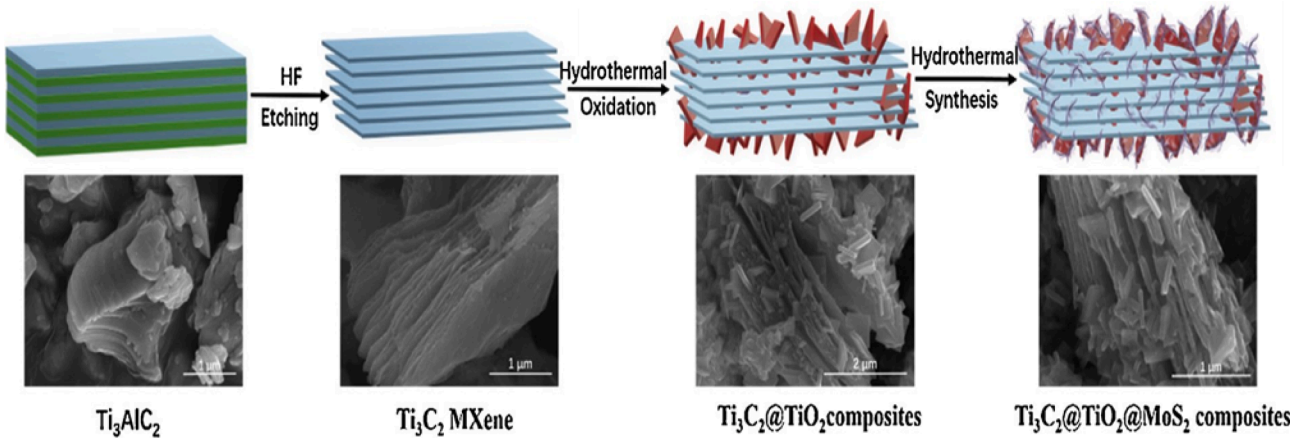

Fig. 7. Schematic of the production of $Ti_3C_2@TiO_2@MoS_2$ composites. Reprinted with permission from Ref. [58].

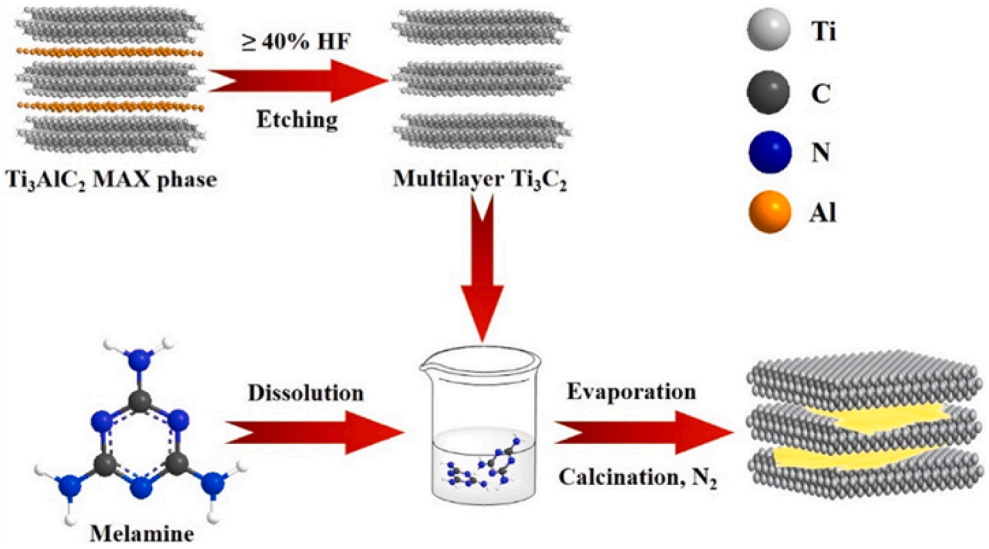

Fig. 8. Steps used in the fabrication of g-C_3N_4/Ti_3C_2 composites. Reprinted with permission from Ref. [59].

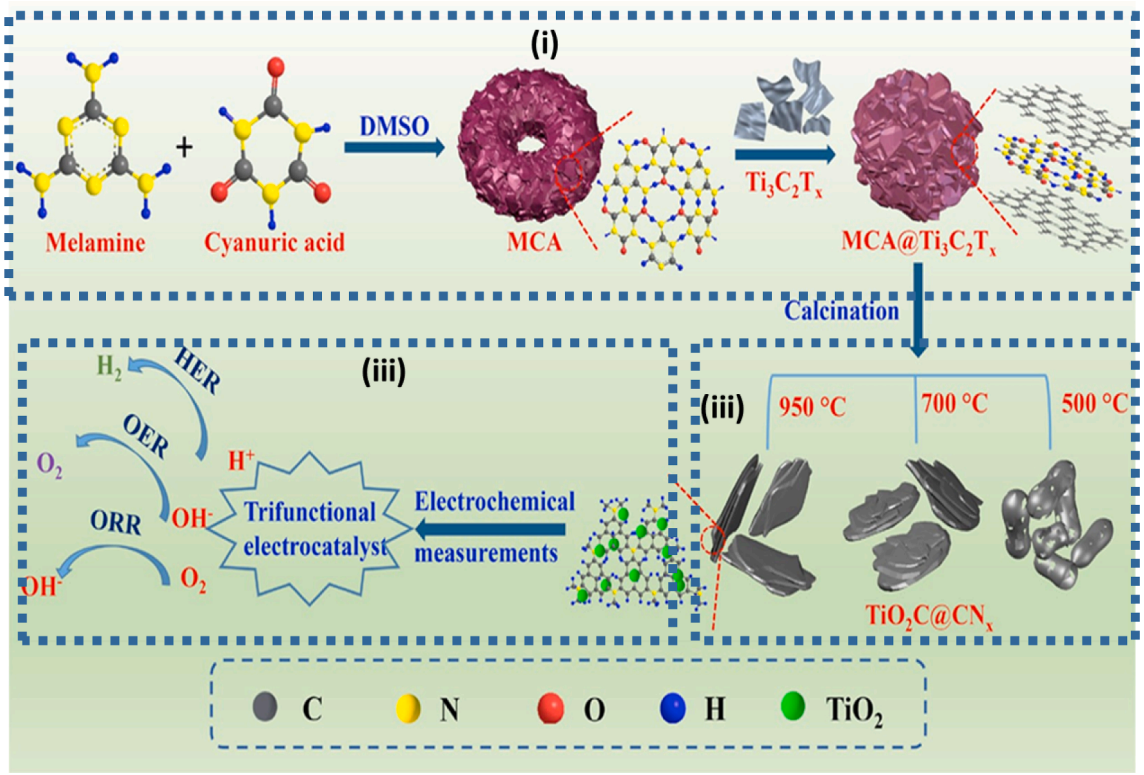

Fig. 9. The preparation of trifunctional $TiO_2C@CN_x$ nanosheets, (i) the synthesis process of MCA and MCA@$Ti_3C_2T_x$ (ii) calcination process and (iii) testing of generated electro-catalysts. Reprinted with permission from Ref. [60].

under Argon flow for an hour. The thermal treatment can be performed at 500, 750, or 950 °C at a heating rate of 5 °C min^{-1} producing different composite structures ($TiO_2C@CN_x$,950, $TiO_2C@CN_x$,700, and $TiO_2C@CN_x$,500) with distinct reactivity.

4. Hydrogen generation via water splitting (W*sp*) using mxenes

4.1. Electrolysis process

Electrochemical W*sp* is one of the most environmentally sustainable and cost-cutting ways to produce hydrogen as. a viable energy source [61]. Because of their rich adjustable surface chemistry, conductivity, and atomic thickness with significantly exposed active sites, MXenes are regarded as promising electro-catalysts for HER [62–65]. This section illustrates how MXenes can be employed as electro-catalysts in electricity-powered $H_{2,\ gen}$. Within the water electrolysis process, a two-electron HER is produced on the cathode by a combination Volmer–Tafel or Volmer–Heyrovsky mechanism. One intermediate's adsorption–desorption process with a two-electron transfer is typically recognized as an HER [66–68]. The $H_{2,\ gen}$. involves three steps (1) Volmer step where one proton adsorbs on the surface of the electro-catalyst in acidic conditions, followed by one electron deduction,

generating the adsorbed intermediate H* following reaction (1). Where the (*) is denoted as adsorbed active site, (2) The Heyrovsky step where the adsorbed H* subsequently interacts with another H^+ and removes one electron, resulting in the formation of one hydrogen molecule following Reaction (2) and (3) the Tafel step which occurs under high coverage of surrounding H*. in this step two adsorbed H* are joined to create hydrogen molecule as per reaction (3).

$$H^+ + e^- \rightarrow H^*(Volmer) \quad (1)$$

$$H^* + H^+ + e^- \rightarrow H_2(Heyrovsky) \quad (2)$$

$$2H^* \rightarrow H_2(Tafel) \quad (3)$$

Regardless of whether the Volmer–Heyrovsky or Volmer–Tafel methods are used, the hydrogen adsorption free energy (ΔG_{H^*}) is widely acknowledged as the yardstick of HER activity [69,70]. In general, an effective electro-catalyst must meet two requirements: Firstly, the value of ΔG_{H^*} should be close to zero. The general trends show that the ΔG_{H^*} value increases with the improvements in hydrogen coverage. If the electro-catalyst has a negative ΔG_{H^*} requires high hydrogen coverage to increase its activity. In contrast, if the ΔG_{H^*} is positive high hydrogen coverage would result in the deactivation of the catalyst. Large positive and negative values result in difficult proton attraction and hydrogen release, respectively. Secondly, the T_s should be small to promote a high charge transfer rate.

4.2. Mxenes as electro-catalysts for water splitting

MXenes have superior physical and chemical characteristics, and a higher potential compared to other nanoparticles. Therefore, they are considered excellent materials-based electro-catalysts for HER. MXenes' surface has many $^-$OH and $^-$O groups, which can form a powerful bond with different semiconductor surfaces. Mxenes have a high electrical conductivity, which makes charge-carrier transport more efficient because metal sites at the terminals of MXenes have higher redox activity than carbon. Furthermore, Mxenes' high hydrophilicity ensures that they make appropriate contact with water molecules. Therefore, MXenes exhibit exceptional structural and chemical stability in aqueous solutions, [15]. Table 1 displays the typical MXene-based and MXene-derived electro-catalysts used in HERs. It can be observed that most of the MXene presented in the table has an **η** in the range 37 to 398 mV and T_s in the range 45 to 100 mV dec^{1}which represents excellent properties for HER. Li et al. [71] reported the HER performance of Ti_2CT_x nanosheets in a solution of 0.5 M H_2SO_4. An Ultrathin Ti_2CT_x nanosheets with rich surface fluorine termination groups is proposed. Where T_x is the surface termination groups ($^-$O, $^-$OH, $^-$F). Different studies and electrochemical measurements have shown that Ti_2CT_x nanosheets with $^-$F termination group can accelerate the kinetics of proton adsorption and minimize the resistance of charge transfer, resulting in favorable electrode kinetics and improved active site reactivity. Furthermore, the thickness of the Ti_2CT_x nanosheets enables high-density active sites required for HER. The rich F-terminated Ti_2CT_x nanosheets have a small **η** of 75 mV, and a T_s of 100 mV dec^{-1}, which are smaller than that of the layered Ti_2CT_x (265 mV and 138 mV dec^{-1}), respectively. These characteristics could enhance the electrochemical hydrogen as suggested by Li et al. [71]. Similarly, Tan et al. [72] introduced $Nb_4C_3T_x$ as an electro-catalyst, and reported the HER performance of $Nb_4C_3T_x$ under acidic and alkaline conditions, approving that $Nb_4C_3T_x$ has high Cat_A similar to other potential 2D materials and superior to most other MXenes. In addition, the excellent electro-chemical stability of $Nb_4C_3T_x$ provides a new option for MXene materials in the HER field. According to a theoretical calculation, Nb-based MXenes, particularly $Nb_4C_3T_x$ exhibit excellent conductivity, and the H-adsorbed Gibbs free energy (DG_H) of OH-terminated $Nb_4C_3T_x$ is near zero, indicating its potential

Table 1
The typical MXene-derived and MXene-based electro-catalysts for Hydrogen gas (H_2) evolution performance are listed below.

Catalyst	Structure of the electrode	Electrolyte	HER (**η**@10 mA cm^2)	Tafel slope (T_s)	Ref.
Ti_2CT_x	F- terminated nanosheets	0.5 M H_2SO_4	75 mv	100 mV dec^{-1}	[71]
$CoMoS_2/Mo_2CT_x$	Mxene	in 1 M KOH	112 mV	82 mV dec^{-1}	[75]
Ti_3C_2 NFs	Nanofibers MXene Nanofibers as Highly Active	0.5 M H_2SO_4,	169 mV	97 mV dec^{-1}	[76]
Ru/c-$Ti_3C_2T_x$/NF	3D nanoplates Synergetic control of Ru/MXene 3D	1.0 M KOH	37 mV	60 mV/dec^{-1}	[43]
TBA-$Ti_3C_2T_x$-Pt	surface terminals (Ti−OH or Ti−O) of the modified $Ti_3C_2T_x$ Achieving Highly Efficient	0.5 M H_2SO_4	55 mV	65 mV dec^{-1}	[66]
Pt/$Ti_3C_2T_x$	Nanoparticles on nanosheets Platinum Nanoparticle-Deposited Ti_3C_2Tx	0.5 M H_2SO_4	67.8 mV	69.8 mV dec^{-1}	[77]
0D/2D NiS_2/V-MXene (V_2CT_x)	sandwich-like structure 0D/2D NiS_2/V-MXene composite	1.0 M KOH	85 mV	100 mV dec^{-1}	[78]
Ni-doped $MoSe_2/Ti_2NT_x$	nanolayers Ni-doped $MoSe_2$ nanohybrids with heterostructure nanohybrids	1.0 M KOH	92 mV	79.7 mV dec^1	[79]
MoS_2-Ti_3C_2 MXene	nanosheets MoS nanosheets with a high percentage of 1T - phase on the edges	0.5 M H_2SO_4	98 mV	45 mV dec^{-1}	[80]
Mo_2CT_x/2H-MoS_2 nanohybrid	Nanohybrid layers Efficient and Long-Lasting Electrocatalysis with 2H-MoS_2 on Mo_2CTx MXene Nanohybrid	0.5 M H_2SO_4	119mv	60 mV dec^{-1}	[81]
FeNi@$Mo_2TiC_2T_x$@NF	FeNi nanoparticles on Mxene NF FeNi@$Mo_2TiC_2T_x$@NF	0.5 M H_2SO_4	160 mV	103.46 mV·dec^{-1}	[59]
$MoSe_2$/MXene	3D-nanoflowers simple method to produce MoSe2/ MXene	0.5 M H_2SO_4	180 mV	91 mV dec^{-1}	[49]
$TiOF_2$@$Ti_3C_2T_x$	nanospheres $TiOF_2$ nanospheres stabilize Ti_3C_2Tx-MXenes	0.5 M H_2SO_4	197 mV	56.2 mV dec^{-1}	[82]
nickel–iron/MXene	NiFe-LDH nanosheets in a mesoporous network over a macroporous	1 M KOH	205 mV	70 mV dec^{-1}	[61]
3 NiFe-LDH/MXene/NF NF=Ni foam LDH= Layered double hydroxides	MXene/NF frame				
Mo_2CT_z MXenes	2D flakes Stoichiometry and surface	0.1 M $HClO_4$	239 mV		[74]
$Nb_4C_3T_x$	nanosheets$Nb_4C_3T_x$ Mxene	1 M KOH	398 mV	122.2 mV dec^1	[72]
$TiO_2C@CN_x$	nanosheets Titanium dioxide encapsulated carbon-nitride nanosheets	0.1 M KOH	(−254.5 mV)	60 mV dec^{-1}	[60]
LSTN/MXene LSTN: $La_{0.4}Sr_{0.4}Ti_{0.9}Ni_{0.1}O_{3-d}$ (LSTN)	Nanoparticles within nanosheets Interlaced two-dimensional MXene nanosheets contain a highly efficient A-site deficient perovskite.	1 M KOH	Large when compared with Mxene (about 190 mV)	Low as compared to LSTN	[76]

usage as catalyst for HER [73]. $Nb_4C_3T_x$ with a 10 mA cm^{-2} as J_A has the **η** of 398 mV, which is significantly lower than T_s of 122.2 mV dec^{-1} of other known MXenes [72]. Furthermore, in both alkaline and acidic conditions, $Nb_4C_3T_x$ has long-term stability and excellent cycling performance. The **η** of $Nb_4C_3T_x$ significantly dropped by nearly 30 mV after 1000 CV cycles [72]. Moreover, Intikhab et al. [74] have demonstrated that Mo-based MXenes are promising as HER catalytic materials. They assessed the stoichiometry of $Mo_{1.33}CT_z$ vs Mo_2CT_z and their atomic surface structure and found it to be critical for catalytic activity, but not for operational durability [74]. As a result of changes in both the electrical characteristics of the surface as well as a drop in the fraction of the optimal -O terminated, hcp sites with a core sixfold coordinated C atom, $Mo_{1.33}CT_z$ is less active for the HER than Mo_2CT with **η** of 422 mV and 239 mV at a J_A of 10 mA/cm^2, respectively [74].

In another study, Yuan et al. [66] added Pt to a series of customized Ti_2CT_x -based (T = F, O, OH; MXene) supports to enhance HER. This Pt-based electro-catalyst is highly effective for producing hydrogen from W*sp* process. The produced catalyst (Pt- Ti_2CT_x) generates an **η** of 55 mV, a J_A of 10 mA cm^{-2} and T_s of 65 mV dec^{-1} [66], which are much less than Ti_2CT_x nanosheets. The **η** is mostly determined by Pt electronic state, which is controlled by the modified Ti_2CT_x 's surface terminals (TiOH or TiO). The HER kinetics are accelerated by the increment in charge transfer between Pt and O terminals and, as a result, overall catalytic performance [66].

Mxenes heterostructure engineering provided a high-efficiency electro-catalyst with a low cost [49,78,79,81]. For example, $MoSe_2$/MXene hybrid nanoflowers as we described above in (section 3.1), demonstrated better HER performance under acidic conditions compared to single-component electro-catalysis as shown in Fig. 10a and reported by Huang, et al. [49]. The voltammogram curves in Fig. 10a show the improvement in HER performance using $MoSe_2$/MXene hybrid nanoflowers compared with their single-component counterparts. The electro-Cat_A of this electro-catalyst depends on the MoSe2/Ti3C2 ratio. Increasing the MoSe2/Ti_3C_2 ratios from 2:1 to 50:1 first increases the catalytic activity (Cat_A) and then decreases, achieving the maximum H_2 generation when Mo/Ti reaches 10/1. In addition, the **η** was found to be 61 mV, which is substantially lower than that of single-component (e.g. $MoSe_2$ ~ 200 mV) and the 2D Ti_3C_2 (~380 mV). Around 6-fold J_A increase was achieved at − 300 mV compared with MoSe2. This excellent H_2 generation rate exceeds different MXene-based electro-catalysts. In addition, It was observed that the polarization curves of this electro-catalysis before after 2000 cycles exhibited a small change (See Fig. 10b). Such behavior confirms the remarkable stability of the hybrid Mo_{10}/Ti nanoflower electrocatalyst. In addition, this electro-catalyst exhibited a high J_A of 10 mA cm^{-2}, a low onset potential of 61 mV, and a relatively low **η** of 180 mV and T_s of 91 mV. dec^{-1} [49]. It was observed that for nano-catalysts with low T_s the required **η** for $H_{2,gen}$. is less. This is established in Fig. 10c, where the nanohybrid electro-catalyst has significantly lower T_s of 91 mV compared with control samples of $MoSe_2$ and Mxenes (200 mV dec^{-1}), indicating that nanocomposites are better for rapid charge transfer and HER [49]. Furthermore, $Ti_3C_2T_x$ nanosheets modified with cetyltrimethylammonium bromide (CTAB) were used; Kong et al. [43] produced an electro-catalyst of Ru-based for overall W*sp* (c- $Ti_3C_2T_x$). The c-$Ti_3C_2T_x$ not only makes it easier to create a Ni foam with a hydrophilic and wrinkled surface, but it also enhances the Ru-based complex's HER activity. The HER in 1.0 M KOH solution using Ru/NF/c-$Ti_3C_2T_x$ electrode displays a 37 mV low **η** with J_A of 10 mA/cm^{-2} in comparison to

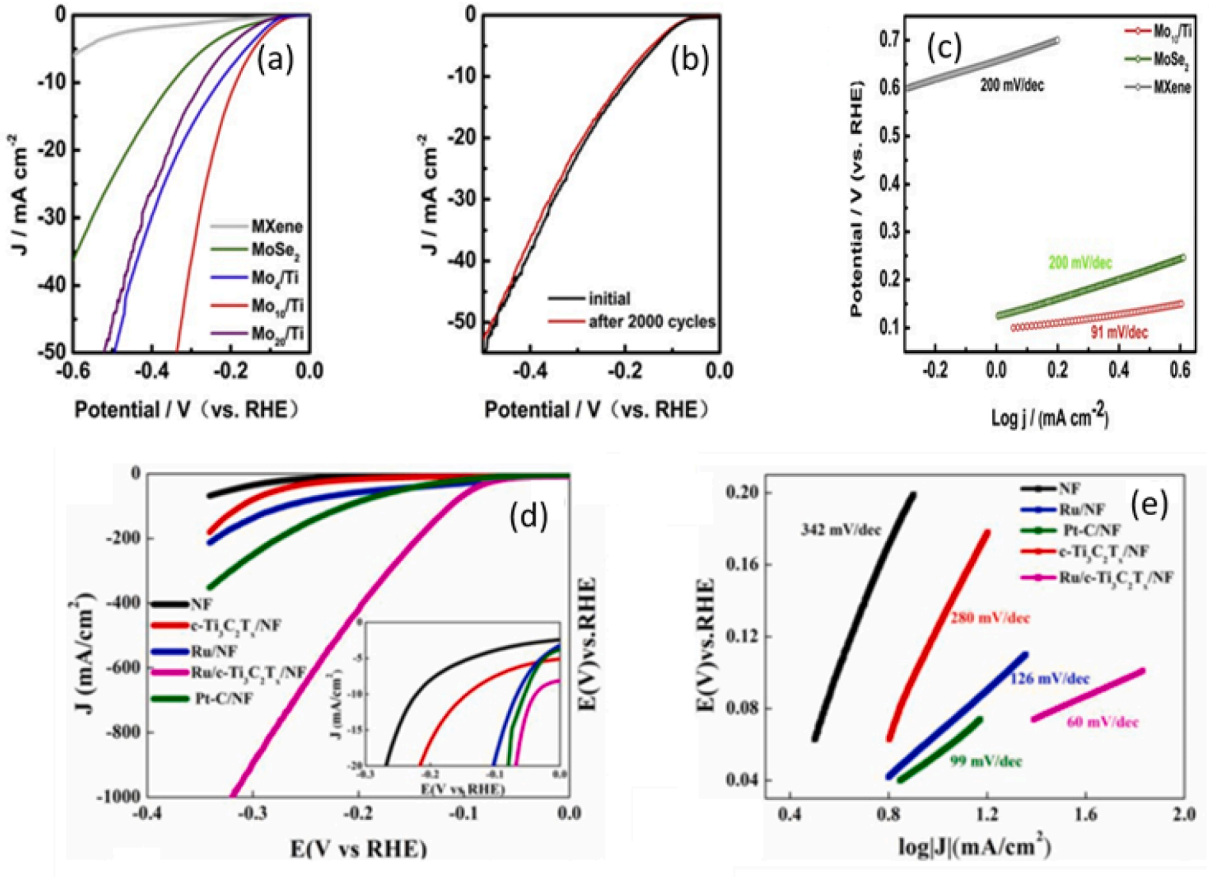

Fig. 10. (a) the current density (J_A) vs potential curves of the produced hybrid nanoflowers (Ti_3C_2 MXene and $MoSe_2$/MXene); (b) initial and final J_A vs **η** Mo_{10}/Ti at a scanning rate of 50 mV s^{-1}. (c) T_s of $MoSe_2$, MXene and Mo_{10}/Ti [49] (d) J_A vs voltammogram curves of the nanoflowers and (e) T_s of NF, Ru/NF, c-$Ti_3C_2T_x$/NF, Pt-C/NF and Ru/c- $Ti_3C_2T_x$ /NF in 1.0 M KOH. Reprinted with permission from Ref. [43].

other tested electrodes which includes c-$Ti_3C_2T_x$/NF (144 mV), NF (222 mV), and Ru/NF (67 mV). The electro-ctalyst showed a relatively low T_s of about 60 mV dec^{-1} in comparison to Ru/NF (126 mV dec^{-1}), NF (328 mV dec^{-1}), c- $Ti_3C_2T_x$ /NF (280 mV dec^{-1}), Pt-C/NF (99 mV dec^{-1}), and Ru/c- $Ti_3C_2T_x$ /NF (126 mV dec^{-1}) as depicted in (Fig. 10 d & e) [43]. The Ru/$Ti_3C_2T_x$ electro-catalyst has a much lower hydrogen adsorption free energy (ΔG_{H^*})after inclusion of Ru into $Ti_3C_2T_x$, compared to $Ti_3C_2T_x$. The near-optimal value of zero improves the subsequent hydrogen evolution phase by optimizing the adsorption and desorption energetics [43].

The Ni doped $MoSe_2/Ti_2NT_x$ (abbreviated as Ni e$MoSe_2$/ Ti_2NT_x) was proposed by Zong et al. [79] as an effective W*sp* photo-catalyst. The Ti_2NT_x improved the electron transfer, prevented $MoSe_2$ aggregation as a 2D conductive substrate, and increased the number of active sites. Adding the metallic Ni to this photo-catalyst improved the Cat_A of Ni e$MoSe_2/Ti_2NT_x$ by successfully modifying the $MoSe_2/Ti_2NTx$ hetero-junction's structure and demonstrated outstanding catalytic and synergistic effects in alkaline media. The performance of Ni e$MoSe_2$/ Ti_2NT_x in HER in alkaline media has the **η** of 92 mV, J_A of 10 mA cm^{-2} and a T_s of 79.7 mV dec^{-1} [79]. This HER performance exceeds the performance of $MoSe_2$/MXene hybrid nanoflowers. Lim et al. [81] synthesized and tested a new Mo_2CT_x/2H-MoS_2 nanohybrid MXene for HER. The Mo_2CT_x MXene was directly sulfided to produce this compound without the use of any other Mo precursors. As a result, the MXene is converted into a layer of 2H-MoS_2 oxide at the nanohybrid interface thereby removing harmful MoO_3 oxides. In comparison with the physical mixing of the individual components (d- Mo_2CT_x + 2H-MoS_2), there was a 22-fold reduction in charge transfers due to the intimate relationship resistance and 16 times higher HER. The presence of highly linked 2H MoS_2 on Mo_2CT_x prevents additional oxidation on the surface of the catalyst, resulting in long-lasting active regions for stable HER catalysis [81]. The Mo_2CT_x/2H-MoS_2 nanohybrid displayed enhanced HER activity in an acidic medium, requiring a J_A of 10 mA cm^{-2}, and an **η of** 119 mV with a very low T_s of 60 mV dec^{-1} [81]. To generate MoS_2 clusters, both Mo and S precursors were previously added on the MXene surface in Co-doped MoS_2 coupling with Mo_2CT_x MXene, resulting in a weakened interface and subsequent MoS_2 obstruction during HER testing, generating a higher **η** of 218 mV at a J_A of 10 mA cm^{-2} in an acidic media [75].

Despite their unique surface properties, Mxenes have low oxidation resistance and can be easily oxidized in water and humid environments, resulting in a significant loss of electrical characteristics and surface reactivity. To increase the catalyst oxidation resistance and enhance the HER performance, Wang et al. [82] used hydrothermal hydrolysis to produce $TiOF_2$ nanospheres on the surface of $Ti_3C_2T_x$ sheets, expanding the electrochemical reaction area and enabling the quick transfer of composite interface charge. This method produces a $TiOF_2$ @ $Ti_3C_2T_x$ photo- catalyst that effectively stabilizes the oxygen-containing terminal on the substrate's surface has great oxidation resistance, and has excellent HER catalytic activity. Experiments have demonstrated that the $TiOF_2$ @ $Ti_3C_2T_x$ generated has a lower **η** and T_s of197 mV and 56.2 mV dec^{-1} at a J_A of 10 mA cm^{-2}, respectively, which are lower than pure $Ti_3C_2T_x$ and $TiOF_2$. [82]. Fig. 11a and b show the FE-SEM image of $Ti_3C_2T_x$ and the $TiOF_2$@ $Ti_3C_2T_x$ composite prepared by Wang et al., after hydrothermal etching. The $TiOF_2$ nanospheres were placed consistently between the layers of $Ti_3C_2T_x$. A cross-section of the $TiOF_2$@ $Ti_3C_2T_x$ monolayer and a rainbow map of the in-situ composition distribution for the same site are shown in Fig. 11c and d. It can be seen that the $TiOF_2$ nanospheres were grown on the Ti3C2 substrate in a single layer 30 nm thick. The HER polarization curves of $Ti_3C_2T_x$ MXene, $TiOF_2$, and $TiOF_2$@ $Ti_3C_2T_x$ composite are shown in Fig. 11e. It was observed that the $Ti_3C_2T_x$ and $TiOF_2$ exhibit high onset potentials of 718 mV and 430 mV, respectively. Both composites had low HER activity. In comparison, the compound $TiOF_2$@ $Ti_3C_2T_x$ demonstrates significant HER activity. The homogeneous distribution of $TiOF_2$ nanospheres on a two-dimensional substrate with good layering decreases the onset potential to 103 mV [82]. Furthermore, the $Ti_3C_2T_x$ with excellent conductivity can give an abundance of electrons for interlayer electron transport to produce the combination of H^+ and O sites [83]. This was confirmed by Tafel plots of $Ti_3C_2T_x$ MXene (T_s = 63.4 mV dec^{-1}), $TiOF_2$ (109.1 mV dec^{-1}), $TiOF_2$@ $Ti_3C_2T_x$ composite (T_s = 56.2 mV dec^{-1}) as shown in Fig. 11 f [82]. Furthermore, The HER was significantly improved by coupling mesoporous NiFe-LDHs nanosheets (NiFe layered double hydroxides) with a favorable-kinetics three-dimensional MXene frame that is scaffolded using macroporous nickel foam (NF) (represented by NiFe LDH/MXene/NF). Yu et al. [61] reported a 3D electro-catalytic hierarchically structured electrode that is used to increase HER activity over NiFe-LDHs at high current densities. The synthesis method of NiFe-LDH/MXene/NF is presented in Fig. 12a. A panoramic SEM picture demonstrates that the NiFe-LDH/MXene/NF frame retains the MXene/NF frame's linked 3D architecture without recording the macropores (see Fig. 12b). At greater magnification, SEM and TEM analyses show the formation of a dense network of amorphous NiFe-LDH nanosheets with thicknesses in the range 100–130 nm with mesopores of tens of nanometers between them on the MXene surface (Fig. 12c–e). The 3D MXene frame improves charge transfer kinetics and water molecule adsorption/activation on electro-catalysts based on NiFe-LDH, which has highly conductive, reactive, and hydrophilic features, offering excellent HER in an alkaline solution. During high J_A and robust electro-catalytic reactions, the 3D linked macroporous structure enables quick access to the electrolyte as well as rapid gas release [61]. Fig. 12 f

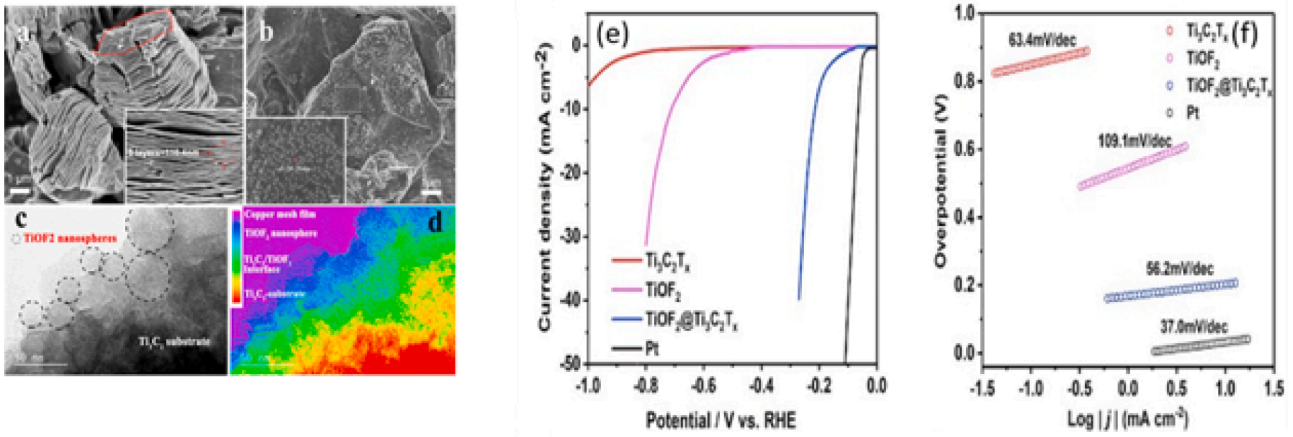

Fig. 11. Morphology of $Ti_3C_2T_x$ (a) SEM image at Medium-magnification, (Inset) SEM image at high-magnification (b) Top view of the $TiOF_2$@$Ti_3C_2T_x$ grain. (Inset) high-magnification SEM image of the composite nanosheet. (c and d) Cross-section of the monolayer of the $TiOF_2$@$Ti_3C_2T_x$ sheet and the rainbow map showing in situ composition distribution. (e) HER polarization curves. (f) The corresponding Tafel plots. Reprinted with permission from Ref. [82].

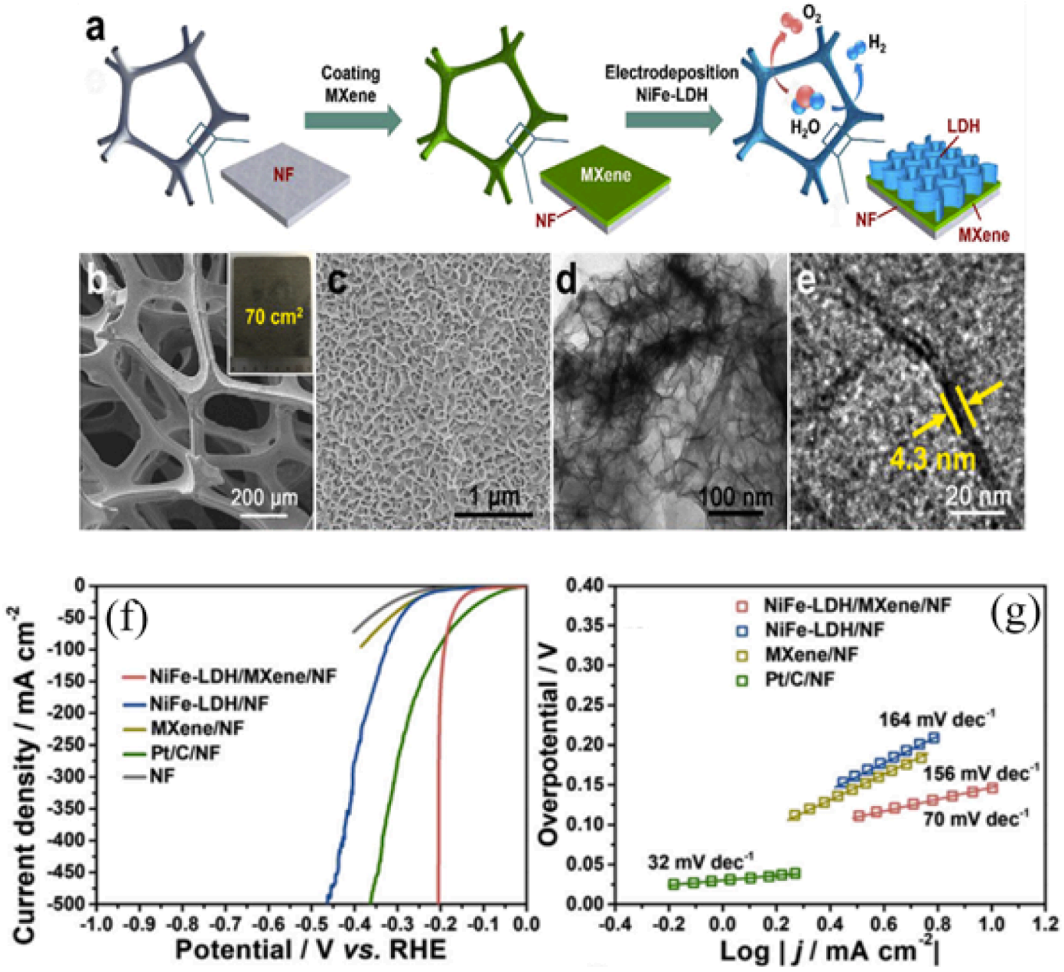

Fig. 12. Preparation, characteristics and electro-catalytic properties of the 3D hierarchically structured NiFe-LDH nanosheets (a) Procedure used in the fabrication of, (b) Surface morphology of NiFe-LDH/MXene/NF. (inset) optical image of the surface area, (c) Surface morphology of NiFe-LDH nanosheets on MXene/NF frame, (d) Surface morphology of NiFeLDH/MXene peeled off from NF, (e) Surface morphology of the amorphous texture of NiFe-LDH nanosheets, (f) voltammogram curves of different 3D hierarchically structured at a scan rate of 10 mV s^{-1}, (g) Tafel plots of different 3D hierarchically structured electro-catalysts. Reprinted with permission from Ref. [61].

displays the NiFe-LDH/MXene/NF polarization curves at a scan rate of 10 mV s^{-1}. The NiFe-LDH/ MXene/NF when compared to the Pt/C catalysts may be utilized directly as an electro-catalytic electrode to obtain high J_A up to 500 mA cm^{-2} for HER in 1.0 M KOH and a moderate **η** and T_s of 205 mV and of 70 mV dec^{-1}, respectively (see Fig. 12) [61].

4.3. *Factors affecting electro-catalytic properties*

The Cat_A of MXene's is influenced by many different factors including surface morphology, termination groups, the presence of transition metals, working functions, and doped elements. All these factors increase the number of active sites and improve the kinetics of the electrodes [71]. Surface morphology significantly affects the electro-catalytic performance of Mxenes. Yuan et al. [84] used hydrolyzed bulk MAX ceramics followed by an HF etching process to manufacture a highly active MXene nanofiber electro-catalyst with an SSA. Fig. 13 a to c) depict the morphologies of Ti_3C_2 NFs under different magnifications. The NF structure of Ti_3C_2 MXene was clearly visible in the TEM images Fig. 13c. The Ti_3C_2 MXene was prepared with Ti_3AlC_2 particle with a bulk thickness of ~2 – 5 μm and size in the range ~5 – 20 μm. These particals were easily influenced by the OH^- ions, which acted as a scissor forming a crack in the 2D Ti_3AlC_2 framework. The 2D Ti_3AlC_2 framework was then etched in hydrofluoric acid (HF) to remove Al out and generate Ti_3C_2 MXene NFs with rich functional groups. MXene nanofibers had a significantly higher SSA and low electrochemical resistance, which can reveal greater active sites than typical MXene flakes and improve the HER activity with a low **η** and T_s of 169 mV and 97 mV dec^{-1} at a J_A of 10 mA cm^{-2}, respectively (Fig. 13 d and e), [84].

The successful coupling of CN_x and TiO_2@C witnesses the fabrication of $TiO_2C@CN_x$ as confirmed by XRD, XPS, FT-IR, Raman, TEM, and SEM tests [60]. It was reported that during the calcination process, this coupling process generates a visible interaction between C, Ti, and graphene-like CN_x as a result of the pore structure. The $TiO_2C@CN_x$ is projected to have a large electrochemical active surface area (ECSA). In addition, when carbon nitride is paired with deficient TiO_2, the formed transport route is effective, boosting the electron transfer efficiency and leading to superior electrochemical performance [85,86]. As a result, $TiO_2C@CN_x$ nanosheets have the potential as a highly active HER catalyst.

The nitrogen-doped graphene-like support also showed an excellent HER activity. These trends contributed to the presence of Ti core synergetic effects with high content of oxygen vacancies and extra active sites created by manipulating carbon's electronic states during the doping of metal cores with nitrogen [60].

Another thin nanosheet model (Ti_2CT_x, where T_x stands for surface termination groups; -O, –OH, and -F) that has an abundance of surface fluorine termination groups is proposed by Li et al. [71] as shown in

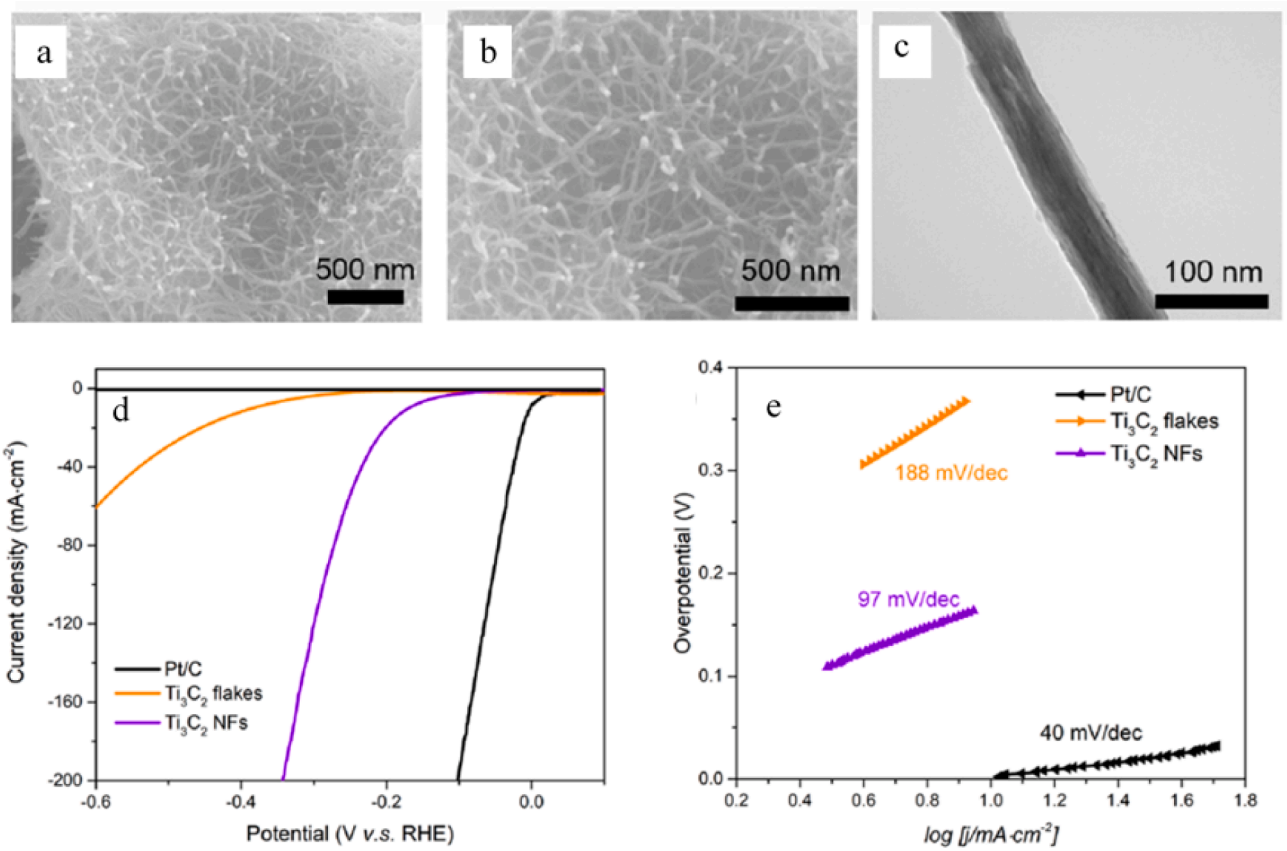

Fig. 13. (a) Procedure used in the synthesis of Ti_3C_2 NFs (b) Surface morphology of Ti_3C_2 NFs electro-catalysts (SEM image (c) High magnification SEM image of Ti_3C_2 NFs. (d) LSV and (e) T_s of Ti_3C_2 NFs, Ti_3C_2 flakes, and Pt/C electrodes. Reprinted with permission from Ref. [84].

Fig. 14a. This nanosheet was manufactured with high modulation synergy between the number of active sites and reactivity. The surface morphology and characteristics of the layered Ti_2CT_x nanosheets are shown in Fig. 14b-d. The Images showed well-defined layered exfoliated Ti_2CT_x nanosheets with a length $\leq$ 1.35 nm. The polarization curves of Ti_2CT_x nanosheets reveal a very tiny onset **η** of 75 mV (see Fig. 14e). The electrochemical measurements revealed that the numerous F terminations groups on the surface of Ti_2CT_x nanosheets lower the charge-transfer resistance and enhance proton adsorption kinetics, which leads to functional electrode kinetics and higher active site reactivity [71]. Furthermore, Ti_2CT_x nanosheets' ultrathin thickness provides active sites of high density for HER. The Gibbs free energy (ΔG_H) is an effective descriptor of the performance of HER. An ideal electro-catalyst should have a near-zero value [87,88]. The effect of abundant F termination groups on the activity of H adsorption on the Ti_2C surface with varying numbers of F termination atoms was studied using density functional theory DFT calculations. This method shows how the Ti_2C surface with varying numbers of F reacts to produce a unique form of H-adhesion. It was observed that the value of ΔG_H continues to drop from 0.66 to 0.34 eV as the number of terminated F atoms increases. The Ti_2CF_6 is an improved version of Ti_2CF_2 with faster proton adsorption kinetics, resulting in higher cathodic J_A and outstanding HER activity. As a result, the richly F-terminated Ti_2CT_x nanosheets have a low overpotential of 170 mV at a J_A of 10 mA cm^{-2} and T_s of 100 mV dec^{-1} (see Fig. 14f), indicating that they would be more useful in real-life applications [71].

he HER activity for Mxenes is also determined by the electrical properties of various transition metal components. Kuang et al. [78] investigated both experimental and theoretical research on the intrinsic electrochemical and structural properties of V-MXene-based hybrid (NiS_2/V-MXene) (Fig. 15a) to assess the viable use of V-MXene-based hybrid (NiS_2/V-MXene) as a promising electro-catalyst for HER. NiS_2/-Ti-MXene and NiS_2/V-MXene have been developed and compared experimentally. Fig. 15 shows the side view structure of both Ti-MXene and V-MXene. The Procedure used in the synthesis of NiS_2/V-MXene includes etching with HF, electrostatic adsorption of Ni^{2+}, hydrothermal reaction and *in-situ* CVD treatment. While NiS_2/V-MXene was proven to be a stronger HER electro-catalyst than NiS_2/Ti-MXene because of its favorable contacts and quick electronic transfer.V-MXene is protected from restacking with the tight cover of NiS_2 nanoparticles, which also favors the exposure of extra active sites that speeds up the process of electrolysis. During electrolysis, a sandwich-like design with more paths for electron migration and mass diffusion, and a wider contact interface is highly preferred as shown in (Fig. 15 b). Moreso, the expected electron transport from V-MXene to NiS_2 is validated experimentally with photo-electron spectroscopy of X-ray. The planar-averaged charge density differential along the Z direction (Dq (z)) for NiS_2/V-MXene and NiS_2/Ti-MXene is shown in Fig. 15c and d, indicating that NiS_2/V-MXene has greater electron transport. In the differential charge density maps, the electron transport trails may also be seen (Fig. 15e and f), where electrons are drawn to travel from MXene to NiS_2. Furthermore, NiS_2/V-MXene has shown excellent reaction kinetics and catalytic performance with a lower **η** and T_s of 179 mV and 85 mV dec^{-1} at J_A of 10 mA cm^{-2}, respectively. This excellent HER reactivity is better than NiS_2//Ti-MXene, NiS_2/, V-MXene, and Ti-MXene [78].

The simulations of density functional theory show that the HER activity of V-MXene is superior to Ti-MXene (see Fig. 16 a) and other known MXenes. Fig. 16b-d illustrates the correlation between reaction coordinate and ΔG_H. The estimated values of ΔG_H were −0.37 and −0.45 eV for AO terminated V-MXene and Ti-MXene, respectively, indicating strong adsorption of the H atom. On the other hand, the AF terminated V-MXene and Ti-MXene exhibit ΔG_H values of 2.0 and 2.8

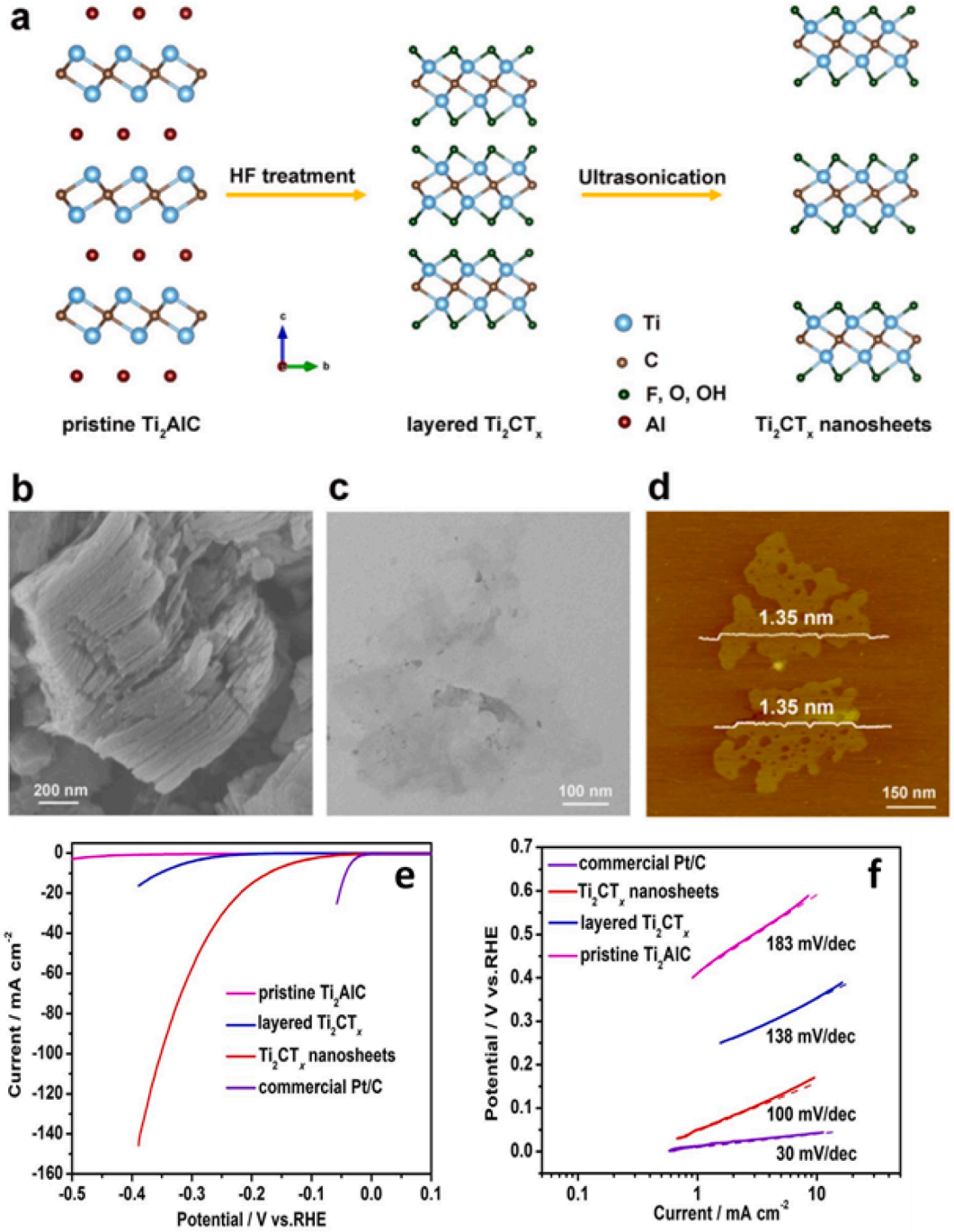

Fig. 14. (a) Procedure used in the synthesis of Ti_2CT_x nanosheets. (b) Layered Ti_2CT_x SEM image. (c) Surface morphology of the layered Ti_2CT_x (TEM image) and (d) AFM image of the as-exfoliated Ti_2CT_x nanosheets. (e) Polarization curves. (f) Corresponding T_s of the Ti_2CT_x nanosheets at scan rates from 10 to 100 mV s^{-1}. Reprinted with permission from Ref. [71].

eV, respectively. The higher work function and lower adsorption free energy of hydrogen determine the superior Ti-MXene activity compared with MXenes as shown in Fig. 16e. The AO/AF terminated MXenes have a higher determined WF than their corresponding bare structures. As an illustration, the WF values of AO terminated V-MXene and Ti-MXene are 6.26 and 5.64 eV, respectively. These values are greater than the comparable bare counterpart values of 4.49 and 4.20 eV, respectively. V-MXene and Ti-MXene have WF values that are between bare and AO terminated MXenes (5.13 and 4.52 eV, respectively) [78]. Fig. 16d depicts the correlation between reaction coordinate and ΔG_H for F, O bare, and terminated Ti-MXene and Vi-MXene. It is challenging to create MXenes with desired surface terminations due to the challenges involved in the experimental control of the MXene surface terminations. As a result, mixed termination groups V-MXene and Ti-MXene were produced, and their WF values were measured. The WF values were determined for V-MXene and Ti-MXene with mixed termination groups (Fig. 16f). The computed values of ΔG_H are 0.45 eV and 0.37 eV for O terminated Ti-MXene and V-MXene, respectively.

The substantial positive values of F terminated MXenes show an obvious indication of weak hydrogen adsorption [78]. Zong et al. [79] examined the HER Tafel slopes and **η**s of $NieMoSe_2/Ti_2NT_x$, $MoSe_2$, Ti_2NT_x, $NieMoSe_2$, $NieTi_2NT_x$, and $MoSe_2/Ti_2NT_x$ electro-catalysts. It

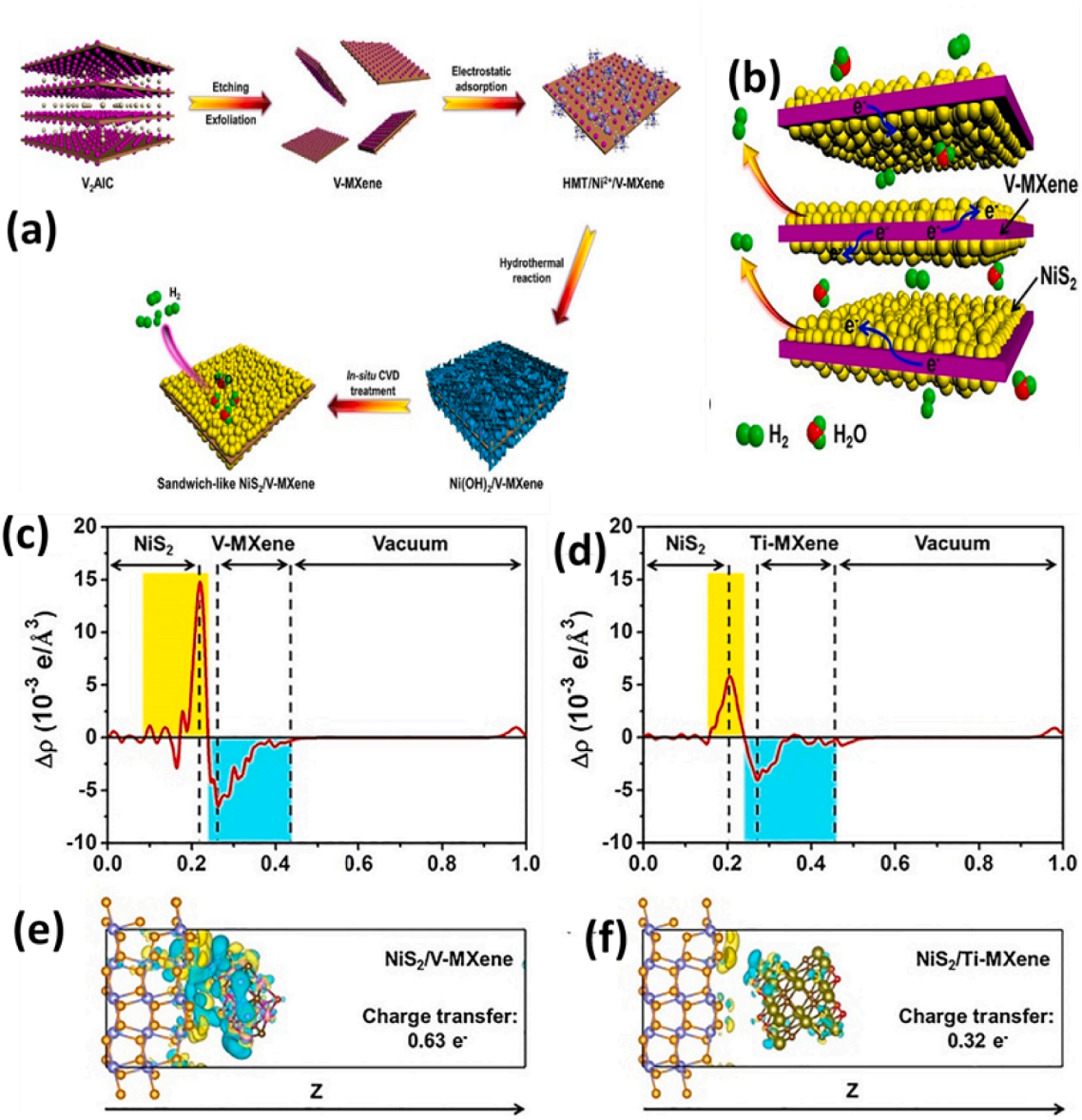

Fig. 15. (a) Procedure used in the synthesis of NiS_2/V-MXene, (b) electron transfer diagram of NiS_2/V-MXene (c, d) Planar and mean electron density difference, and (e, f) differential electron density map of NiS_2/V-MXene and NiS_2/Ti-MXene. Reprinted with permission from Ref. [78].

was shown that the $NieMoSe_2/Ti_2NT_x$ catalysis has a low **η** of 92 mV at $J_A$of 10 mA cm^{-2}. In comparison, $MoSe_2$, Ti_2NT_x, $NieMoSe_2$, $NieTi_2NT_x$, and $MoSe_2/Ti_2NT_x$ catalysts require greater **η**s to arrive at the same J_A of 10 mA/cm^2, and **η**s of (334, 293, 238, 262 and 139 mV, respectively). $NieMoSe_2$ has a lower **η** than $MoSe_2$, indicating that the presence of Ni in the catalysis of $MoSe_2$ can accelerate HER in an alkaline environment. The number of active centers is increased by doping Ni, and the number of catalytic sites is increased by combining $MoSe_2$ nanoflowers with a large number of catalytic sites.

4.4. Photo-catalysts water splitting using mxenes

Several research have suggested that MXenes are likely good co-catalysts in photo-catalytic W*sp* to produce H_2 and could be excellent candidates for highly efficient noble-metal catalysts with low cost and high stability. The charge separation is a critical factor in photo-catalytic systems [89–91]. Low-efficiency charge separation typically results in quick recombination of the photo-generated carriers as well as impairing the photo-catalytic capabilities [92,93]. As a result, efficient charge separation has been prioritized in the design of successful photo-catalytic devices [44,94–96].

According to current studies, using very high conductive metallic Ti_3C_2, the first and most widely used MXene, as semiconductors co-catalyst promotes the mobility of charge carrier and enhances the interfacial coupling by forming effective Schottky junctions [97–99]. Consequently, MXene-based photo-catalysts were observed to have greatly increased HER performance under visible light irradiation. This was aimed at the formation of Schottky-based heterojunction on the as-prepared *n*-type MXene/semiconductors [16,97,100]. The heterojunction can enhance electron mobility, boost the quantity of photo-generated carriers, and thus improve the photo-catalytic efficiency and the production of hydrogen even under visible light irradiation [101–103]. MXene composites and metal sulfiude have recently been proposed as effective photo-catalytic for HER [104]. For example, 1D/2D CdS nanorod@Ti_3C_2 MXene (CdS@Ti_3C_2) composites were synthesized using the hydrothermal technique [105]. The accordion-like multilayer photo-catalyst adds reactive sites on the surface of Ti_3C_2 MXene NSs with strong electronic transfer characteristics, inhibiting carrier recombination and establishing a good photo-catalytic for HER at a rate of 63.53 μmol h^{-1} at an apparent quantum efficiency of 2.28 %

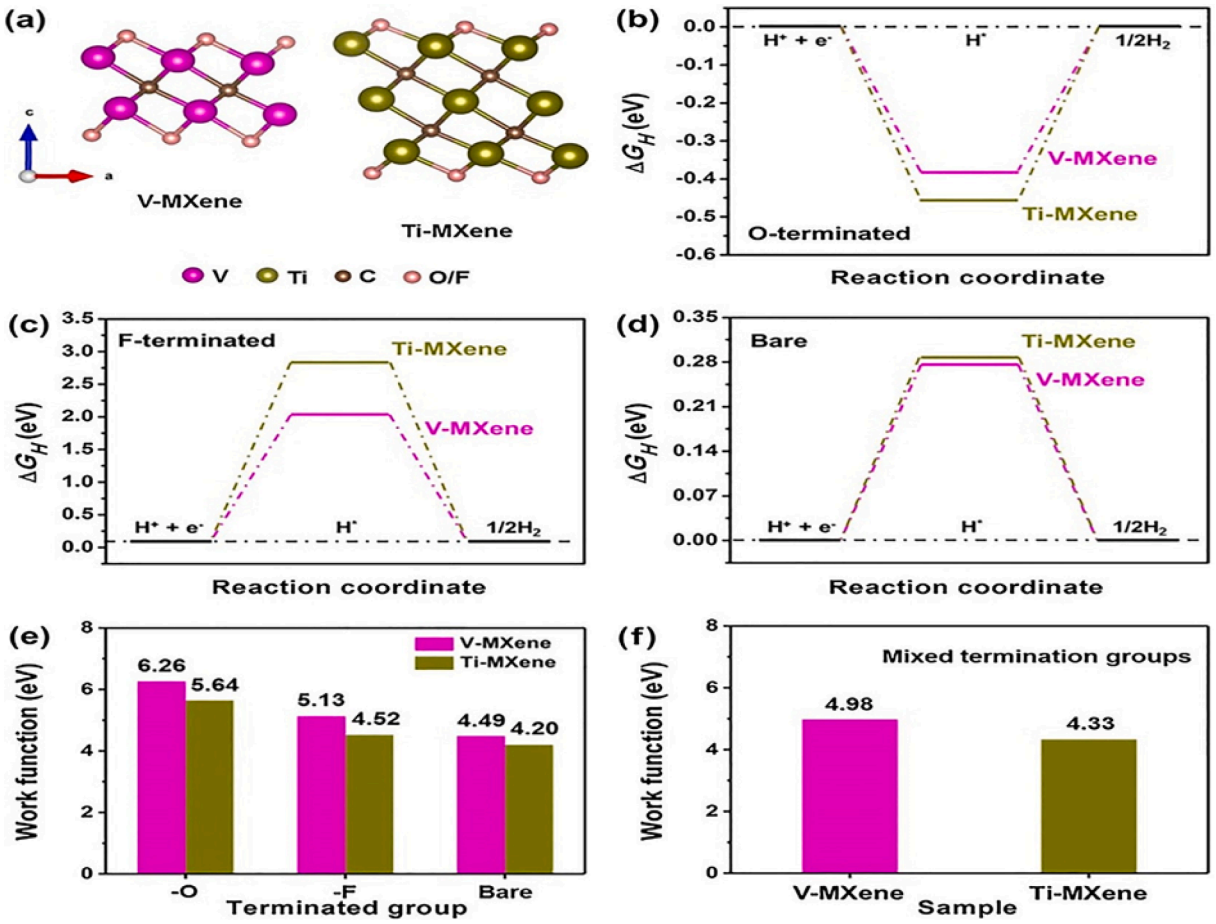

Fig. 16. (a) the Side view structure of Ti-MXene and V-MXene. (b) ΔG_H of AO terminated Ti-MXene and V-MXene, (c) ΔG_H of AF terminated Ti-MXene and V-MXene and (d) ΔG_H of bare V-MXene and Ti-MXene, respectively. (e) calculated Work function (WF) of AF, AO bare and terminated V-MXene and Ti-MXene, respectively. (f) calculated WF) of mixed termination groups in Ti-MXene and V-MXene. Reprinted with permission from Ref. [78].

[105]. The ST_S method was used in the preparation of 1D/2D CdS nanorod@Ti_3C_2 because it can provide Schottky heterojunctions with quicker charge separation and reduced Schottky barriers [51]. These characteristics enhanced the solar-driven HER from W*sp* and exhibited an excellent rate of 2407 μmol $g^{-1}h^{-1}$, which is seven times higher than the efficiency of pure CdS nanorods [51], and much more efficient than hydrothermally produced 1D/2D CdS nanorod@Ti_3C_2. Another metal sulfide (CdS@Mxene) was fabricated by Zhang et al. [106] using ultrasonic treatment. The newly proposed method was used to increase the active sites on the nanocomposites by using co-catalysts that are large-sized Mxene nanosheets, and the photo-catalysts are small-sized CdS nanosheets, resulting in excellent properties of nanocomposites. The high number of transfer channels helped in the separation of electrons from CdS nanosheets and their transport to large-scale Mxene nanosheets. The developed nanocomposites increased the $H_{2,\ gen.}$ under visible light from 2.8 mmol/g for pure CdS nanosheets to 17.5 mmol/g for the CdS@Mxene nanocomposites, reporting an 83 % increase in the [106]. Another nanocomposite (Mo_2CMXene/CdS) was reported by Jin et al. [107]. According to theoretical calculations, the Mo sites in the Mo_2C-MXene/CdS heterostructure provide an efficient reaction site for HER. According to the electrical structures, the heterostructural band edge and band gap position are conducive for W*sp*. This nanocomposite produces H_2 at a rate of 17 964 μmol $g^{-1}h^{-1}$. The H_2 production is approximately 20 % greater than previously published values for Ti_3C_2 MXene photo-catalyst. The $CdLa_2S_4/Ti_3C_2$ nanocomposite was also used in photo-catalytic $H_{2,\ gen.}$ To synthesize the $CdLa_2S_4/Ti_3C_2$ nanocomposites, the $CdLa_2S_4$ nanoparticles were grown in situ on the Ti_3C_2 nanosheets [108]. The $CdLa_2S_4/Ti_3C_2$ nanocomposites produced H_2 from W*sp* with excellent photo-Cat_A under visible light irradiation. The maximal $H_{2,\ gen.}$ rate achieved by this nanocomposite was 11182.4 μmol $g^{-1}h^{-1}$, which is 13.4 times greater than pure $CdLa_2S_4$ and also exceeded Pt-loaded $CdLa_2S_4$. The apparent quantum efficiency of $CdLa_2S_4/Ti_3C_2$ nanocomposite at 420 nm was found to be 15.6 %. The strong photo--Cat_A of $CdLa_2S_4/Ti_3C_2$ was aimed to the enhanced conductivity, which influenced the separation and migration of the photo-generated charge carriers. Recently, a simple electrostatic assembly technique was used to fabricate unique ultrathin $Cd_xZn_{1-x}S/Ti_3C_2$ MXene composites [56]. Spectroscopic characterization analysis and band theory discussion were used to demonstrate the impacts of Schottky barrier and the electronic interaction originating from close contact of Ti_3C_2 MXene and $Cd_xZn_{1-x}S$ on the rapid separation of photo-induced electron-hole pairs as shown in Fig. 17a. When exposed to visible light, the ultrathin $Cd_xZn_{1-x}S/Ti_3C_2$ MXene composite exhibited a high rate of HER of 15035.81 mol $g^{-1}h^{-1}$, which was 2.7 times higher than pure $Cd_xZn_{1-x}S$ (with 5566.35 μmol $g^{-1}h^{-1}$) as shown in Fig. 17b.

Tie et al. [50] designed a hybrid photo-catalyst of Zinc Sulphide nanoparticles using Ti_3C_2 MXene nanosheets to improve the photo-catalytic generation of H_2 [50]. Under ideal conditions, the addition of Ti_3C_2 to Zinc Sulphide increases charge transfer, leading to an increased H_2 generation yield of 502.6 μmol $g^{-1}h^{-1}$, which is about 4-times higher than that of pure ZnS (124.6 μmol $g^{-1}h^{-1}$). In another work, the ultrasonic oscillation was used to prepare ZnS NPs/MXene by incorporating the novel Ti_3C_2Tix with ZnS nanoparticles [109]. The resultant ZnS NPs/MXene composite showed an enhanced $H_{2,\ gen.}$ yield of 212 μmol $g^{-1}h^{-1}$ under visible light in comparison to pure ZnS NPs. Terminated Mxene $Ti_3C_2Ti(O, OH)_x$ was also used as a 2D template for in

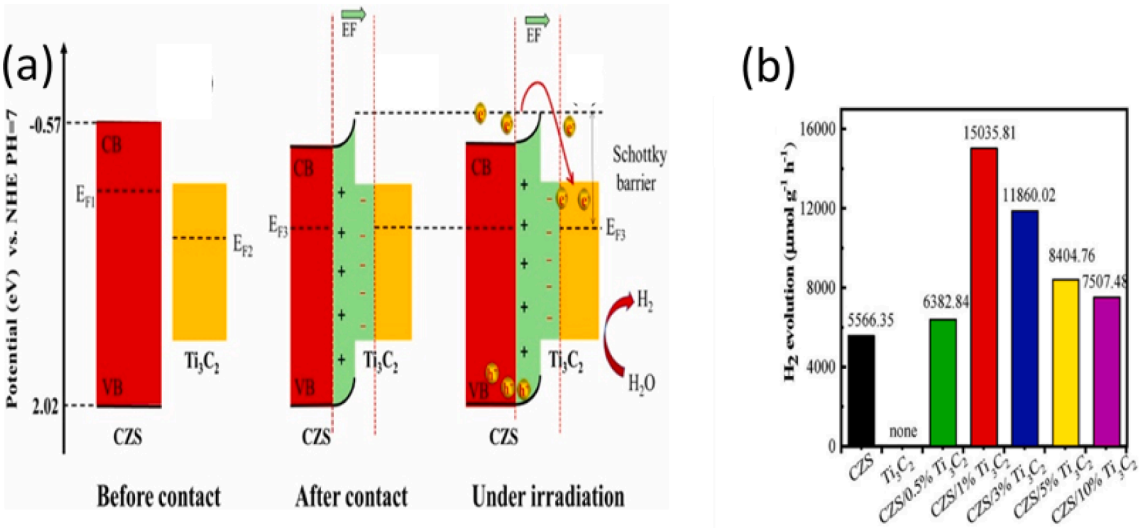

Fig. 17. (a) Mechanism for enhancing CZS/Ti_3C_2 photo-catalytic activity, (b) HER over different catalysts. Reprinted with permission from Ref. [56].

situ growth of flower-like $Zn_2In_2S_5$ microspheres under anaerobic hydrothermal conditions, resulting in hierarchical hybrids $Zn_2In_2S_5/Ti_3C_2(O, OH)_x$ structure [110]. The photo-generated electron transfer efficiency from hybrids $Zn_2In_2S_5$ to $Ti_3C_2(O, OH)_x$ was 33.0 %. Important details about the microstructure and morphology of the hybrids $Zn_2In_2S_5$ are shown in Fig. 18 a-e. The $Zn_2In_2S_5$ to Ti_3C_2 exhibited uniformly flower-like microspheres with numerous layers/sheets. It was observed that the microspheres have dimeter ≤ 1 μm and the thickness ≈60 nm. The developed layered morphology helped in the formation of an interconnected structure with high number of micto-channels that will help the movement and diffusion of ions. The negatively charged $Ti_3C_2T_x$ developed a hydrophilic surfaces with ^{-}OH, ^{-}O or ^{-}F functional groups (i.e). The layered $Ti_3C_2T_x$ allows for immobilization of cationic metals such as Zn^{2+} in aqueous solution. Results showed that the photo-Cat_A of the hybrids $Zn_2In_2S_5$ -$Ti_3C_2(O, OH)_x$ depends on the mass of $Ti_3C_2T_x$ added during the synthesis process. For example, the addition of use of 8 mg of $Ti_3C_2(O, OH)_x$ during the preparation process (ZIS0MX-8 in Fig. 18f) increased the $H_{2,\ gen}$ yields up to 12,983.8 μmol $g^{-1}h^{-1}$ under visible light, which was 1.97 times higher than pure $Zn_2In_2S_5$ (6581.8 μmol g − 1, ZIS in Fig. 18f). The apparent quantum efficiency at 420 nm was found to be 8.96 %. Fig. 18f. also shows that the cumulative production of H_2 increased as a function of time and as the mass of $Ti_3C_2(O, OH)_x$ used during the preparation increased to 8 mg. However, a mass of $Ti_3C_2(O, OH)_x \geq 8$ mg did not show further photo-Cat_A improvement. The Photo-catalytic performance of $Zn_2In_2S_5$ (i.e. ZIS) was significantly improved upon coupling with $Ti_3C_2(O, OH)_x$, supported by the increase in the $H_{2,\ gen}$ rate over $Zn_2In_2S_5$ -$Ti_3C_2(O, OH)_x$ composites with increasing $Ti_3C_2(O, OH)_x$ content, attaining a maximum HER rate of 12,983.8 μmol g^{-1}. Fig. 18 g shows the proposed mechanism for the generation of hydrogen by the $Zn_2In_2S_5/Ti_3C_2(OH, O)_x$ hybrids under visible light irradiation.

Upon exposure to the visible light, the photo-generated electrons from the hybrid composite excited from the valance band (VB) to the conduction band (CB) to produce the electron-hole pairs. This is also accompanied by the migration of electrons from the CB of $Zn_2In_2S_5$ to $Ti_3C_2(O, OH)_x$ via the heterojunction interface. Therefore, the Photo-induced electrons accumulate on the $Ti_3C_2(O, OH)_x$ because the CB potential of $Zn_2In_2S_5$ is more negative than the Fermi level (E_f) of $Ti_3C_2(O, OH)_x$ and the in-plane electrical conductivity of $Ti_3C_2(O, OH)_x$ is one order-of-magnitude higher than the vertical basal plane. After that, the in-plane accumulated electron reacts with immobilized O_2 and generate O_2^-, which is reduced later on to generate HO^- and contribute to the HER.

The use of noble-metal-free co-catalysts for solar-powered photo-catalytic W*sp* has gained a lot of interest. MoS_2 has shown potential as a viable alternative co-catalysts for HER as an efficient co-catalyst in photo-catalytic processes [111]. Nanoscale MoS_2 has an excellent catalytic active site and a large SSA [112–114]. The MoS_2 catalytic active sites, on the other hand, are only found along the margins of the MoS_2 layers [115]. Recent theoretical and practical studies have shown that the active sites of MoS_2 can be increased with defect-engineering [116]. The density of molybdenum vacancies and the number of MoS_2 edges are thought to be important determinants in adjusting Cat_A [117]. The hydrothermal approach was used to produce a new MoS_2/Ti_3C_2 catalyst having a distinct sphere/sheet heterostructure. The MoS_2/Ti_3C_2 heterostructure loaded with 30 % Ti_3C_2 showed a maximal $H_{2,\ gen}$. rate of 6144.7 μmol $g^{-1}h^{-1}$, which is 2.3 times greater than that of pure MoS_2. The heterostructure significantly improved the hole separation and photo-generated electron, while providing additional activation sites, thereby increasing photo-catalytic HER. The Ti_3C_2 interacts closely with MoS_2 to achieve a high H_2 photo-catalytic generation activity under the irradiation of visible light due to its logical design and shape adjustment. MoS_2/CdS catalysts are not efficient in W*sp* to produce H_2 because of many challenges, including poor electrical conductivity, a shortage of reactive sites on MoS_2, and limited charge carrier mobility [48]. The production of CdS-MoS_2-MXenes was firstly described for photo-catalytic H_2 generation using a simple hydrothermal technique by Chen et al. [48]. In comparison to CdS or CdSMoS_2, the CdS-MoS_2-MXenes showed a substantial improvement in H_2 production at the rate of 9679 μmol $g^{-1}h^{-1}$ as shown in Fig. 19. The average H_2 production rate was increased during 4 h measurement from 3329 μmol·g^{-1}·h^{-1} for pure CdS to 9679 μmol·g^{-1}·h^{-1} when CdS- MoS_2-MXene was used. This was due to the shortage in reaction active sites and fast recombination of photo-generated electron-holes pair on the surface of CdS. In addition, the adding MoS_2 promotes electrons transmission and reduces the possibility of recombination of photo-excited electron-hole pairs. The apparent quantum efficiency of CdS- MoS_2-MXene at 420 nm was found to be 26.7 %. it was concluded that MXene with good conductivity helps the transportation of electrons and promotes the HER.

Asides from MXene-derived photo-catalysts and MXene-based photo-catalysts, notably completely and partially oxidized MXenes have piqued the interest of HER researchers. Li et al. [58] designed a unique 2D-2D-2D structure of Ti_3C_2@TiO_2@MoS_2 nanocomposite. This design features electrons and holes that are photo-generated on the most active photo-catalysis surface TiO_2. Fig. 20 a-b presents the scanning electron microscopy (SEM) images used to analyze the morphology of Ti_3C_2 MXene, Ti_3C_2@TiO_2composites. The (15 wt% MoS_2) of Ti_3C_2@TiO_2@-MoS_2 composites achieve an optimum HER rate of 6425.297 μmol

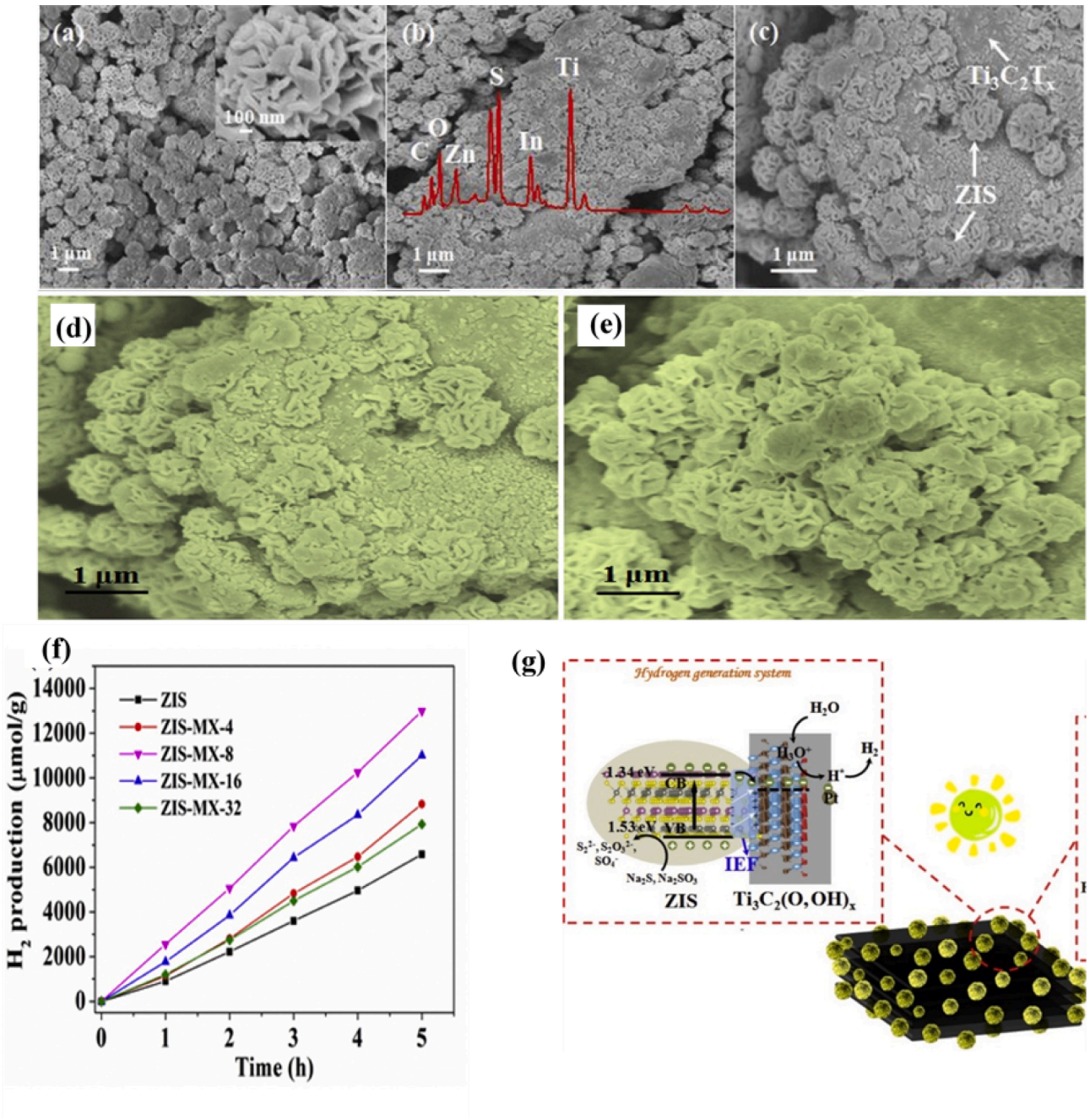

Fig. 18. FESEM images of (a) pure $Zn_2In_2S_5$ (ZIS), (b,c) $Zn_2In_2S_5/Ti_3C_2(OH, O)_x$ hybrids (with SEM-EDS spectra overlay). Futurization of $Zn_2In_2S_5$-$Ti_3C_2(OH, O)_x$ composite (i.e ZIS-MX-8) before and after photo-catalytic $H_{2.gen}$ (d) SEM image before photo-catalysis; and (e) SEM image after photo-catalytic HER: (f) cumulative H_2 as a function of time using different $Zn_2In_2S_5$-$Ti_3C_2(OH, O)_x$ composite with different amount of $Ti_3C_2(OH, O)_x$ (8 mg for ZIS-MX-8, 16 mg for ZIS-MX-16..etc); (g) The proposed mechanism for $H_{2,\ gen}$ over the $Zn_2In_2S_5/Ti_3C_2(OH, O)_x$ hybrids under the irradiation with visible light. Reprinted with permission from Ref. [110].

$g^{-1}h^{-1}$ which is much higher than other samples (Fig. 20 c-d). It is also quite stable under the reaction condition. The Ti_3C_2 MXene high electronic conductivity works as a titanium source to improve charge separation efficiency and the proposed photo-catalytic mechanism is shown in Fig. 20 e. In another study, conducted by the same researchers, a simple hydrothermal technique was used to generate TiO_2 nanosheets on the surface of Ti_3C_2 MXenes [118]. The SEM is used to characterize the morphology and structure of the acquired samples as shown in Fig. 21a-b. The $NaBH_4$ was employed as a reducing agent to decrease the portion of the Mo^{4+} in MoS_2 and generate vacancies of molybdenum which play important role in carrier recombination inhibition (Fig. 21 c). The newly constructed $Mo_xS@TiO_2@Ti_3C_2$ composites have much enhanced photo-catalytic HER rate 10505.8 µmol $g^{-1}h^{-1}$ which has also significantly improved stability.

The electrostatic self-assembly approach was also employed to prepare a 1D/2D TiO_2/Ti_3C_2 photo-catalyst [55]. The as-prepared TiO_2/-Ti_3C_2 nanocomposites have a maximum rate of generation of H_2 of 6.979 mmol $g^{-1}h^{-1}$ which is 3.8 times greater than pure TiO_2 nanofibers. The enhancement in the photo-catalytic generation of H_2 over TiO_2/Ti_3C_2 is due to the heterogeneous interface between Ti_3C_2 nanosheets and TiO_2 NFs. Yang et al. [119] described the deposition of PtO nanodots on the *in-situ* produced TiO_2-Ti_3C_2 MXene composites for the photo-catalytic generation of hydrogen. The Ti_3C_2 MXene in the $PtO@Ti_3C_2/TiO_2$ photo-catalyst functions as a hole acceptor for TiO_2 and PtO, while PtO nanodots capture electrons for the $H_{2,\ gen}$. reaction and inhibit the hydrogen reverse oxidation reaction resulting in a

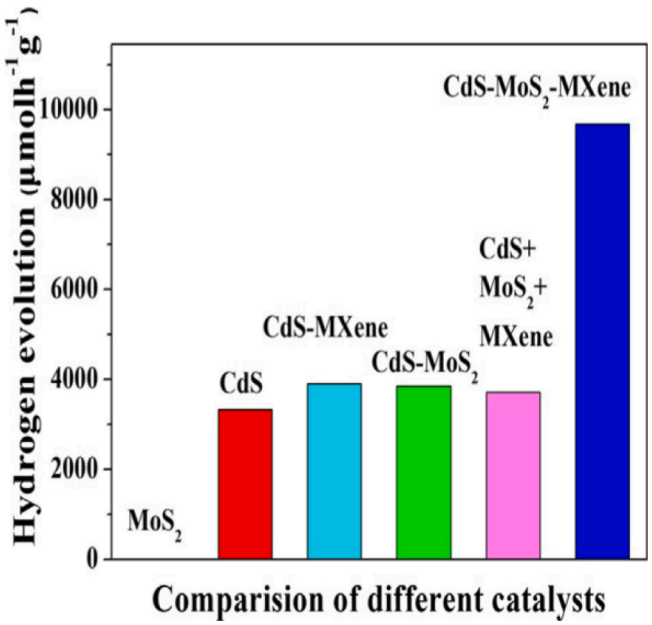

Fig. 19. Photo-catalytic $H_{2,gen}$ over MoS_2, CdS, CdS-MoS_2, CdS-MXene, physical mixture of (CdS, MoS_2 and MXene), CdS-MoS_2-MXene. Reprinted with permission from Ref. [48].

significant improvement in separation efficiency of photo-generated carriers. Thus, this composite resulted in a significantly improved photo-catalytic $H_{2,\ gen}$. efficiency with a rate of 12054 µmol $g^{-1}h^{-1}$. Peng et al. [57] proposed the preparation of Cu/TiO_2@$Ti_3C_2T_x$ nanocomposite by hydrothermal reduction method followed by photo-deposition. The $^{-}$OH terminated 2D $Ti_3C_2T_x$ was used as a hole mediator due to its low work function to inhibit the migration of holes from TiO_2 to MXenes as shown in Fig. 22a. This encouraged the photo-deposition of the earth-abundant copper on TiO_2 as a reduction co-catalyst. The utilization of two co-catalysts ensured that photo-generated carriers were effectively separated and that extremely active HER occurred over metallic copper particles. The activity for HER was increased by up to tenfolds (2200–3800 µmol g^{-1}).

As shown in Fig. 22b, the photo-catalytic $H_{2,\ gen}$. during 5-h irradiation of the TiO_2@$Ti_3C_2T_x$-12 h without Cu exhibits a relatively low activity (325 mol g1), but in the presence of copper, the activity is dramatically increased by up to 10 times (2200–3800 mol g1). The maximum rate of $H_{2,\ gen}$. over the Cu_4/TiO_2@$Ti_3C_2T_x$-12 h catalyst was 764 mol g h 1. The addition of Cu2O nanoparticles to the composite decreased the active sites at Cu-TiO_2 interfaces, which also led to a decrease in $H_{2,\ gen}$. The stability and reusability of the ideal Cu_4/TiO_2@$Ti_3C_2T_x$-12 h catalysts were tested and there was no change in the $H_{2,\ gen}$. after five consecutive W*sp* experiments (see Fig. 22c). The results showed that the photocatalyst had excellent stability against the commonly reported photo-leaching and photo-corrosion of Cu-based catalysts.

A wet-chemistry reduction approach was used to synthesize the Cu_2O/(001)TiO_2@$Ti_3C_2T_x$ photo-catalyst [120]. The Cu_2O surface coverage rose as copper loading increased, while particle size remained fixed. The mechanism and photo-Cat_A of ternary Cu_2O/TiO_2@Ti_3C_2Tx are strongly influenced by the surface covering of copper species. The monomer Photo-catalyst Ti_3C_2Tx and TiO_2 have very good photo-Cat_A compared with pure Cu_2O as shown in Fig. 23a. It was determined that the absence of active sites for $H_{2,\ gen}$. makes the monomer catalysts Cu_2O, $Ti_3C_2T_x$, and TiO_2-32 h exhibit relatively poor photo-catalytic activity. The maximum $H_{2,\ gen}$. over binary TiO_2@$Ti_3C_2T_x$ photo-catalyst did not exceed 165 mmol. h^{-1}/g^{-1} (Fig. 23b). Upon adding Cu_2O nanoparticles to this photo-catalyst the HER was significantly enhanced. The cumulative H_2 generation during 6 h of irradiation was increased to 3677 and 3462 mmol.g^{-1}mmol/g for the photo-catalyst loaded with 5 % and 25 % Cu_2O, respectively. Fig. 23a shows that the HER performance of the photo-catalyst increased by increasing the loading amount of Cu_2O reaches 25 %. The HER rate decreased to 954 mol/g and 782 mol.g-1, respectively, when the loading amount of Cu_2O nanoparticles was raised to 45 % and 65 %. The Ti_3C_2Tx served as a hole reservoir for the inadequate surface coverage of the photo-catalyst by Cu_2O. The in situ Cu_2O was first reduced to metallic copper by excited electrons. The reverse movement of carriers results in a considerable HER rate of>1100 µmol.$h^{-1}g^{-1}$ enabled the spatial separation of photo-generated electron-hole pairs. The $H_{2,\ gen}$. rate for the photo-catalyst with a low loading amount of Cu_2O (5 %) reached 1496 µmol.h^{-1}.g^{-1} as shown in Fig. 23b. The mechanism and charge transfer over the Cu_2O/TiO_2@$Ti_3C_2T_x$ photo-catalyst with low and high Cu_2O coverage is shown in Fig. 23 c and d. At low loading amounts of Cu2O, the nanoparticles are dispersed on the surface of TiO_2@$Ti_3C_2T_x$ photo-catalyst as support. Since the TiO_2 is the dominant phase, the excited electron-hole pairs will be produced on its surface and the TiO_2 and photo-catalysts reaction pathway will be based on the migration of the photo-generated holes to the $Ti_3C_2T_x$ with the hole trapping. Even though the CB of Cu_2O (1.4 eV) was more negative than that of TiO_2, the photo-generated electrons will collect on the CB of TiO_2 (0.3 eV). The CB of Cu2O, on the other hand, might be reduced to metallic Cu by the electrons that have accumulated on the CB of TiO_2.

Under a high Cu_2O loading amount (Fig. 23d), intercepted light excites both Cu_2O and TiO_2 to produce photo-generated electron-hole pairs and contribute to the generation of hydrogen. Increasing the surface coverage and thickness of Cu_2O layer would reduce the absorption of light by the TiO_2. The light excitation is therefore solely based on Cu_2O. As a result, the photo-induced holes flow from VB of TiO_2 to Cu_2O whereas the photo-generated electrons primarily move from CB of Cu_2O to CB of TiO_2. The $H_{2,\ gen}$. was only moderately high because there was no $H_{2,gen}$ at a high Cu_2O loading level.

The UiO-66-NH_2 and annealed $Ti_3C_2T_x$ MXenes were utilized as electron acceptors to produce interfacial charge transfer channels and enhance the photo-catalytic W*sp* response and activity [95]. The developed Ti_3C_2/TiO_2/UiO-66-NH_2 photo-catalyst demonstrated outstanding photo-catalytic HER performance with a rate of 1980 µmol h^{-1} g^{-1}. Over the years, carbon in Ti_3C_2 has garnered a lot of interest as a photo-catalyst for the $H_{2,\ gen}$. For example, a one-step calcination procedure was used to build the 2D/3D g-C_3N_4/Ti_3C_2 heterojunction as Schottky catalyst. Fig. 24a presents the schematic of the proposed mechanism for photo-catalytic H_2 generation over g-C_3N_4/Ti_3C_2 composite.

Irradiation of the g-C_3N_4/Ti_3C_2 photo-catalysis by visible light excite the electrons from the VB to CB of g-C_3N_4 generating photo-induced e^{-}-h^{+} pairs. Due to its superior conductivity and lower E_f the Ti_3C_2 acts as an electron sink. As a result, the excited electrons easily migrate to Ti_3C_2 while the corresponding holes stay in the VB of g-C_3N_4. Schottky junction and wide intimate interface on the structure of the g-C_3N_4/Ti_3C_2 photo-catalysis support this migration process. In addition, metallic conductivity help in the separation of the photo-induced e^{-}-h^{+} pairs and capturing the electrons by Ti_3C_2. This will help the formation of different active sites on Ti_3C_2 to produce H_2. The immobilized holes in the VB of g-C_3N_4 will oxidize the organic matter in the water and contribute to the $H_{2,\ gen}$. Therefore, it was concluded the electron sink and charge separation properties of g-C_3N_4/Ti_3C_2 MXene photo-catalysis provide active sites to enhance the rate of HER [59]. The results show that lamellar g-C_3N_4 strongly bonds with Ti_3C_2, and the resulting composites have 6 times more charge separation efficiency than pure g-C_3N_4.

As shown in Fig. 24b, Ti_3C_2 alone exhibits no photo-catalytic HER activity under visible-light irradiation. While g-C_3N_4 has very low activity (17.5 µmol. $h^{-1}g^{-1}$) for the production of H_2 under visible light. However, coupling g-C_3N_4 with Ti_3C_2 photo-catalysis showed enhanced photo-catalytic performances and its potential for the production of H_2 is gradually enhanced by increasing the amount of g-C_3N_4. The g-C_3N_4

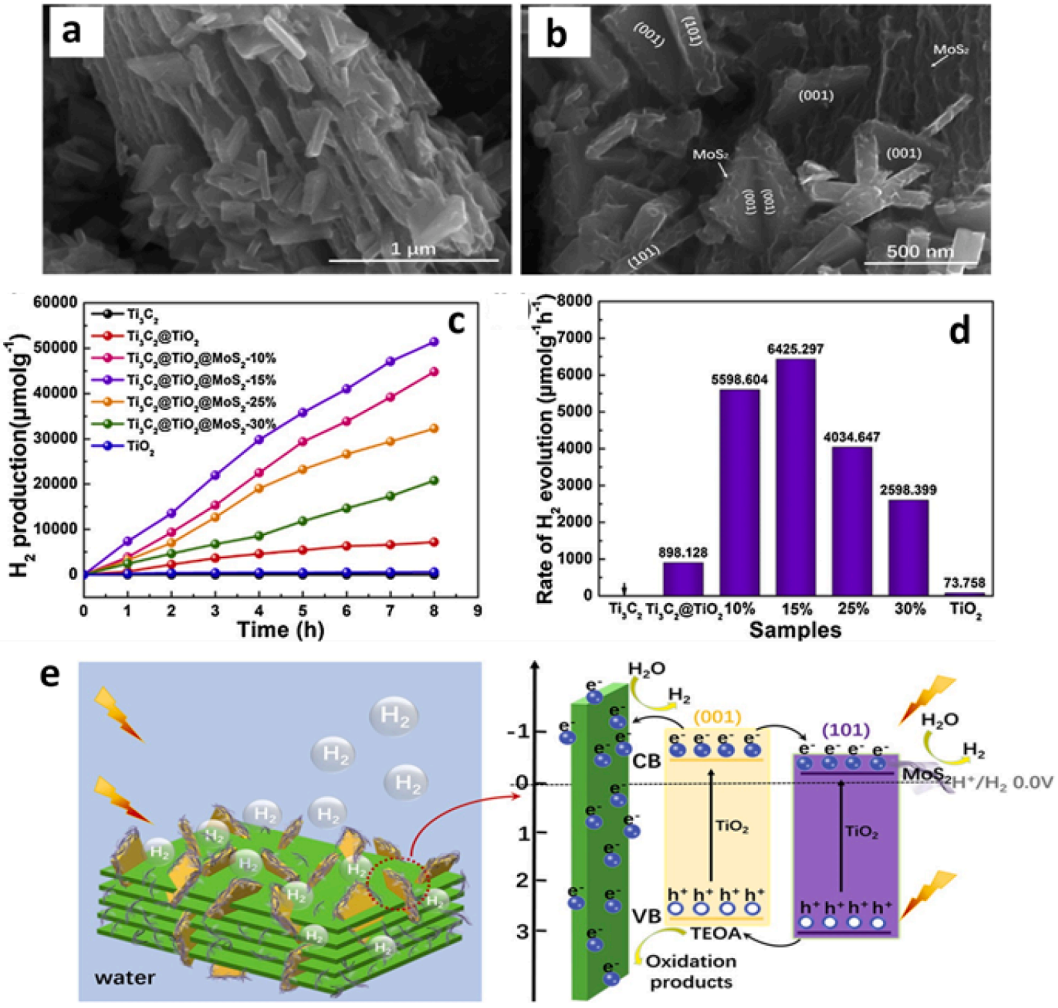

Fig. 20. SEM images of (a, b) Ti_3C_2@TiO_2@MoS_2 composites (15 wt% MoS_2). (c) Photo-catalytic H_2, gen and (d) photo-catalytic $H_{2,gen}$ rate for different catalysts in an aqueous solution of acetone with TEOA. (e) The proposed mechanism for the photo-catalytic HER over Ti_3C_2@TiO_2@MoS_2 composites under the irradiation of solar light. Reprinted with permission from Ref. [58].

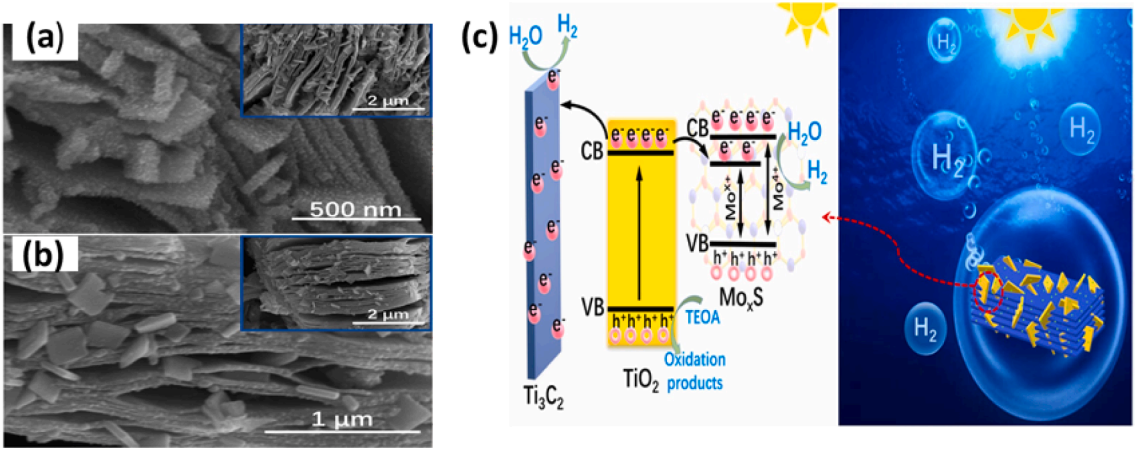

Fig. 21. SEM images of (a) MoS_2@TiO_2@Ti_3C_2-160 °C and (b) Mo_xS@TiO_2@Ti_3C_2-160 °C. (c) The proposed mechanism for the photo-catalytic HER over Mo_xS@TiO_2@Ti_3C_2 composites. Reprinted with permission from Ref. [118].

Ti_3C_2 photo-catalysis with a g-C_3N_4 mass fraction of 80 wt% achieved the maximum HER production rate of 116.2 μmol. $h^{-1}g^{-1}$, which is 6 times higher than g-C_3N_4. Increasing the mass fraction of g-C_3N_4 higher than 80 %, significantly decreased the photo-catalytic HER rate due to the decrease of active sites covered by excessive g-C_3N_4. The ability of conductive Ti_3C_2 to remove electrons from considerably limited electron-hole recombination, as such, many functional groups on Ti_3C_2′s surface offered enough active sites for HER. In another study on the

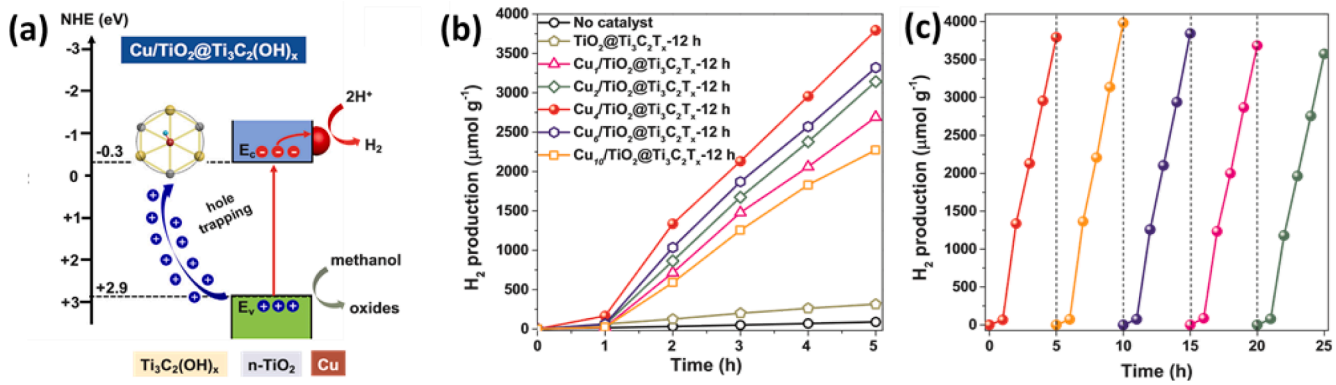

Fig. 22. (a) Charge-transfer at Cu/TiO_2@$Ti_3C_2(OH)_x$ interface after the induction period of W*sp* reaction. (b) HER over Cu_y/TiO_2@$Ti_3C_2T_x$-12 h, (c) W*sp* reaction for the recycling test over Cu_4/TiO_2@$Ti_3C_2T_x$-12 h. Reprinted with permission from Ref. [57].

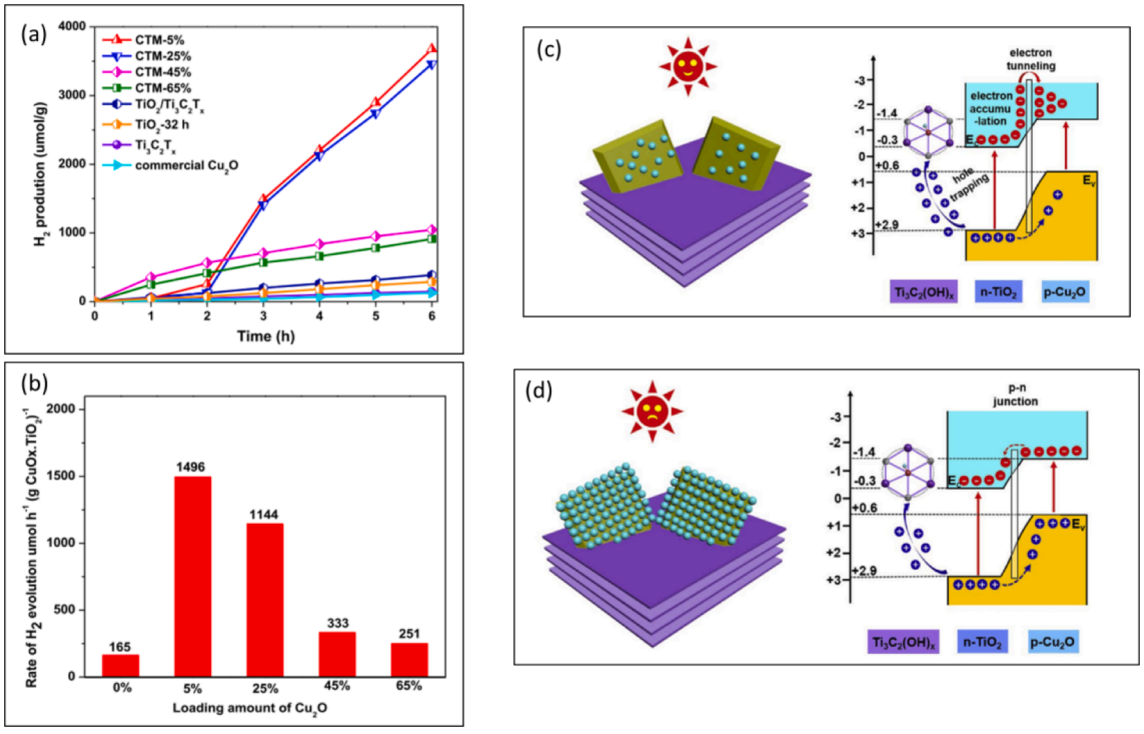

Fig. 23. (a) HER via W*sp* over TiO_2@$Ti_3C_2T_x$ photo-catalyst (CTM) photo-catalysts, TiO_2, Cu_2O and $Ti_3C_2T_x$. (b) HER rates as a function of the loading amounts of Cu_2O. Photo-catalytic reaction mechanism and charge-transfer at the ternary Cu_2O/TiO_2@$Ti_3C_2T_x$ photo-catalysts interface with (c) low and (d) high Cu_2O loading. Reprinted with permission from Ref. [120].

coupling between g-C_3N_4 and Ti_3C_2, an annealing approach was used to make 2D O-doped g-C_3N_4 nanosheets, followed by an in-situ electrostatic assembly of positively charged O-doped g-C_3N_4 nanosheets and negatively charged Ti3C2 MXene to make a 2D/2D Ti_3C_2 MXene/O-doped g-C_3N_4 Schottky-junction [54]. When compared to Ti_3C_2 MXene/pristine C_3N_4 (15573 mol/g/h) and pristine O-doped g-C_3N_4 (13745 mol/g/h), the Ti_3C_2 MXene/O-doped g-C_3N_4 Schottky-junction has nearly twofold improved HER rate (25124 mol/g/h) as shown in (Fig. 25a and b). According to fully characterizations and theory calculations, the improvement in photo-catalytic performance could be ascribed to the construction of the Schottky-junction and the synergistic effect of intimate 2D/2D interfacial contact, resulting in efficient separation of the photo-generated charge and short charge transport distance from HCN to Ti_3C_2 MXene (Fig. 25 c). Moreover, Han et al. [121] fabricated the C-TiO_2/g-C_3N_4 photo-catalysts, Ti_3C_2 was used as the only carbon precursor. The generation of hydrogen via photo-catalytic mechanism for the C-TiO_2/g-C_3N_4 photo-catalysts is explained in Fig. 26a.

The photo-catalytic $H_{2,\ gen}$. mechanism for the C-TiO_2/g-C_3N_4 photo-catalysts is based on the narrow bandgap for C-TiO_2 and g-C_3N_4, which resulted in the generation of electrons and holes upon irradiation with visible light. The generated electrons of the well-defined heterojunction system in the CB of g-C_3N_4 rapidly transfer to the CB of C-TiO_2, while the holes transfer from the VB of C-TiO_2 to the VB of g-C3N4. Subsequently, the photo-generated electrons in the CB of C-TiO_2 combine with H ions in the water through the co-catalyst, and the holes react with sacrificial reagent. Thus, the system accelerates transportations and prevents recombination of photo-generated holes and electrons, and enhances the photo-catalytic generation of H_2 process. It was concluded that C-TiO_2/g-C_3N_4 displays an enhanced H_2 yield (1409 μmol/h/g) when compared to pure C-TiO_2 and g- C_3N_4 and as depicted in Fig. 26 b.

A polymer, carbon nitride (CN) was presented as a promising photo-catalytic material of W*sp* and $H_{2,\ gen}$. this type of photo-catalysis has limitations stemming from low photo-conversion efficiency due to

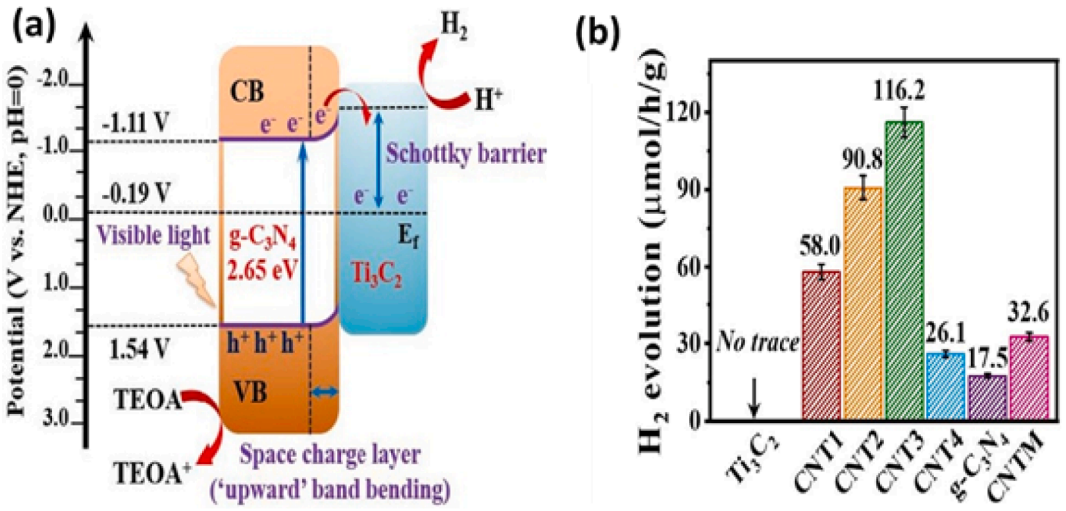

Fig. 24. (a) The proposed mechanism for the photo-catalytic HER for photo-catalytic $H_{2,\ gen}$ over g-C_3N_4/Ti_3C_2 composite; (b) photo-catalytic $H_{2,\ gen}$ over different g-C_3N_4/Ti_3C_2 composites. Reprinted with permission from Ref. [59].

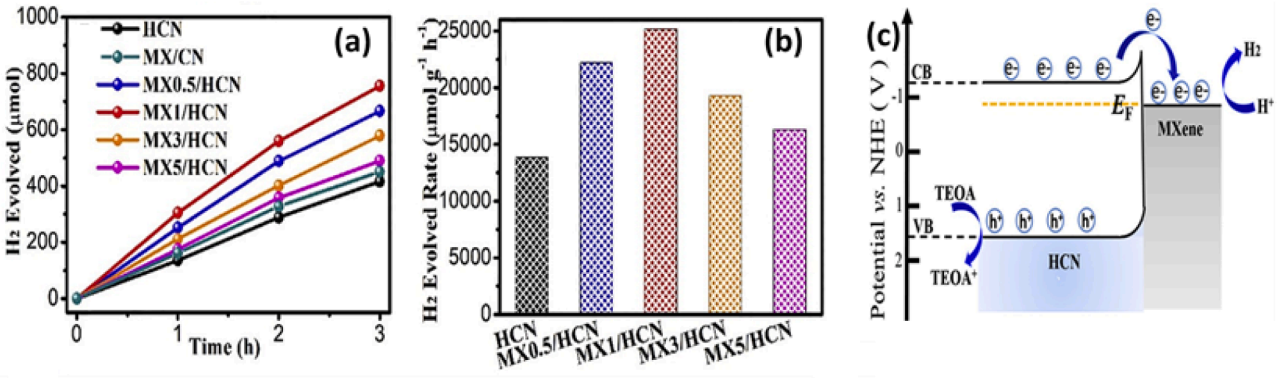

Fig. 25. (a) $H_{2,\ gen}$ over different photo-catalysis as a function of time and (b) Rates of HER in HCN and MX/HCN samples; (c) MX1/HCN Schottky-junction photo-catalytic HER mechanism. Reprinted with permission from Ref. [54].

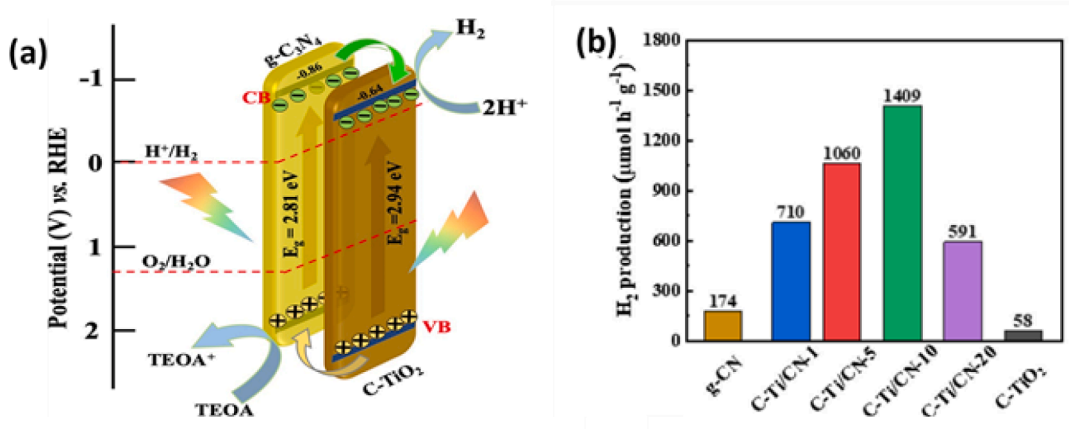

Fig. 26. (a) The mechanism of the photo-catalytic $H_{2,\ gen}$ over g-C_3N_4/Ti_3C_2 composite. (b) the $H_{2,\ gen}$ rate over a g-CN photo-catalyst. Reprinted with permission from Ref. [121].

having high defect density and the recombination of the photo-excited carrier. These limitations can be reduced by surface engineering to add CN crystals. Li et al. [122] successfully constructed an ordered Schottky heterojunction of crystalline carbon nitride (heptazine-based) and Ti_3C_2 MXene using an ion-thermal technique. The HCN/Ti_3C_2 composite exhibited an excellent HER rate of 4225 μmol $g^{-1}h^{-1}$, which is approximately 2 and 8 times higher than pristine HCN and bulk CN, respectively. In addition, the HCN/Ti_3C_2 showed excellent stability upon cycle use. Recently, 2D hierarchical g-C_3N_4 nanosheets were placed onto 2D exfoliated titanium carbide (TiC) multilayers etched

with in situ produced TiO_2 [123]. Because of the excellent migration and transfer of the charge carrier, 1.26 times more H_2 was produced by hierarchical g-C_3N_4 than by bulk g-C_3N_4. The improved TiC/HCN 2D/2D heterojunction achieved a 310 μmol $g^{-1}h^{-1}$ generation rate of H_2.

Chlorophylls (Chls), the most well-known natural pigment serves sential role in the intake of light and transfer of energy to the reaction centers in natural photo-synthesis [124–126]. However, pristine Chls have several flaws, including a low ability to absorb solar light, high recombination efficiency of photo-excited electron-hole pairs, and an insufficient active site, all of which limit their use in highly efficient HER. Several investigations have been carried out in an attempt to boost its photo-Cat_A [127]. For example, three derivatives of aggregate-forming chlorophyll (Chl-n; n = 1–3) are compared as antenna pigments with light-harvesting characteristics. With the Chl-3@$Ti_3C_2T_x$ composite, the finest HER performance was determined to be up to 122 μmol.h^{-1}.g^{-1} (Fig. 27 a) [126]. The mechanism of the photo-catalytic HER over the Chls@Ti_3C_2Tx system was proposed to clarify the effects of the Ti_3C_2Tx deposited by different Chl derivatives Chl-n, as shown in (Fig. 27 b and c). Moreover, five chlorophyll derivatives were produced and used as effective visible light harvesters [127]. The (2D) $Ti_3C_2T_x$ MXene was utilized as an excellent electron capturer. The Co-Chl@$Ti_3C_2T_x$ hybrid was discovered to have the best HER performance, reaching 49000 μmol.$h^{-1}g^{-1}$ as shown in Fig. 29 a. This is the result of high electron-hole pair separation efficiency and best light-harvesting capabilities of Co-Chl@$Ti_3C_2T_x$ composite. The energy level depiction of the five M−Chls as photo-catalyst is shown in Fig. 28 b.

Factors affecting photo-catalytic properties

A good photo-catalyst should have a good absorption in the visible range, a reasonable band gap, a long charge separation lifetime, as well as a suitable redox potential [40]. The preparation method and the morphology of MXenes can adjust their electronic and electrical conductivity. Doping, changing phase, changing surface termination, or replacing the outer metal layers with another metal are all methods for controlling the electrical characteristics of MXenes. The MXenes' "hybrid" metallic-semiconductor properties make them ideal for use as great electromagnetic wave absorbers in light-to-heat conversion materials [129]. For example, the photo-Cat_A of Ti_3C_2-TiO_2 composites prepared by Zong et al. [53] is higher than that of Ti_3C_2-TiO_2 composites reported in early literature shown in Table 2 [32–138]. This was aimed at the high energy of TiO_2 and higher photo-catalytic activity, as well as well-established morphology and size control than *in-situ* prepared counterparts (Fig 0.29 a to c). The $H_{2,gen}$ linearly increases as a function of reaction time for all the used photo-catalysts. The HER rates for TiO_2, 3.3 %Ti_3C_2-TiO_2, 6.7 % Ti_3C_2-TiO_2 and 10 % Ti_3C_2-TiO_2 were found to be 190.47, 199.02, 390.92, and 270.31 μmol. h^{-1}, respectively. The Ti_3C_2-TiO_2 photo-catalysts have higher photo-catalytic $H_{2,gen}$ activity than pure TiO2. The photo-catalytic $H_{2,gen}$ significantly increase by increasing the mass fraction of Ti_3C_2 to 6.7 % after that the activity decreased because of the light shielding effect of excessive Ti3C2 nanosheets. The obtained composite has HER rate of 310.55 μmol. h^{-1} (Fig. 29d). Long-term absorption of light, 101-faceted surface exposure, and improved charge separation efficiency are factors responsible for the remarkable photo-catalytic performance of TiO_2 nanoparticles. The proposed photo-catalytic mechanism for Ti_3C_2-TiO_2 composites is shown in Fig. 29e. The TiO_2 displays an adsorption onset of 385 nm, indicating a value of 3.2 eV as the wide band-gap energy, which is consistent with that of anatase TiO_2. The combination of TiO_2 and Ti_3C_2 nanosheets can somewhat reduce TiO_2′s band gap energy, which will benefit photo-catalytic HER applications. In another study, the electrostatic self-assembly approach is employed to create a novel 1D/2D photo-catalyst of TiO_2/Ti_3C_2 [55]. The TiO_2/Ti_3C_2 nanocomposites have a maximum generation rate of H_2 of 6.979 mmol.h^{-1}. g^{-1}, which is 3.8 times higher than pure TiO_2 nanofibers. The improved photo-catalytic H_2 generation of TiO_2/Ti_3C_2 is due to the heterogeneous interface between Ti_3C_2 nanosheets and TiO_2 NFs. Fig. 30 shows that the visible range absorbance of the TT_3 sample is significantly higher than that of pure TiO_2. The dark color of Ti_3C_2 is said to be responsible for the enhanced light absorption, implying that the TT_3 sample has a higher $H_{2,\ gen}$ performance. Furthermore, the prohibited bandwidth of TiO_2 estimated using the TAUC approach is around 3.07 eV.

Monolayer co-catalysts not only have more exposed active sites and larger SSA for photo-catalytic reactions than multilayer co-catalysts, but they also lower the distance for migration of photo-generated charges. Hence, monolayer co-catalysts can serve as effective catalysts for the separation of photo-generated holes and electrons [137]. In contrast to monolayer sulfide, the hydrophilic functionalities of $Ti_3C_2T_x$ (T_x = F, O, OH) can encourage significant interactions with the molecules of water [139]. Additionally, the exposure of metal terminal sites on $Ti_3C_2T_x$ may increase redox reactivity. Su et al. [137] reported $Ti_3C_2T_x$ multilayer and monolayer production and application as co-catalysts for commercial TiO_2P_{25}. Monolayer $Ti_3C_2T_x$ has an ultrathin nature and a high electronic conductivity that is essential for electrons migration from TiO_2 to $Ti_3C_2T_x$, resulting in greater photo-catalytic $H_{2,\ gen}$ and electron-hole pair separation efficiency than $Ti_3C_2T_x$ multilayer co-catalyst. The Ti_3C_2Tx/TiO_2 composites photo-Cat_A is greater than that of pure TiO_2.

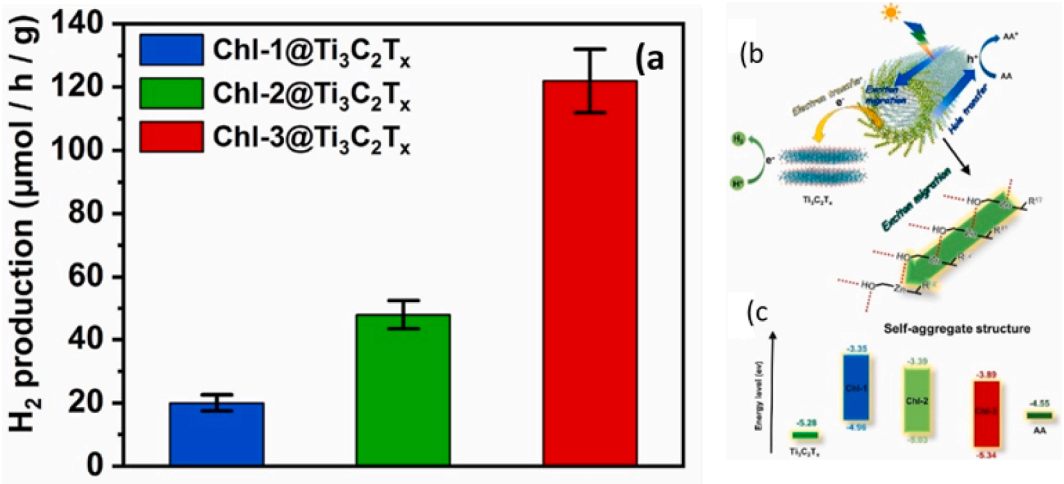

Fig. 27. (a) $H_{2,\ gen}$ over different Chl-n@$Ti_3C_2T_x$ composites (b) Schematic illustration of Chl-n@$Ti_3C_2T_x$ composites over Chl-n@$Ti_3C_2T_x$ composites under the irradiation of visible light and (c) energy-level illustration. Reprinted with permission from Ref. [128].

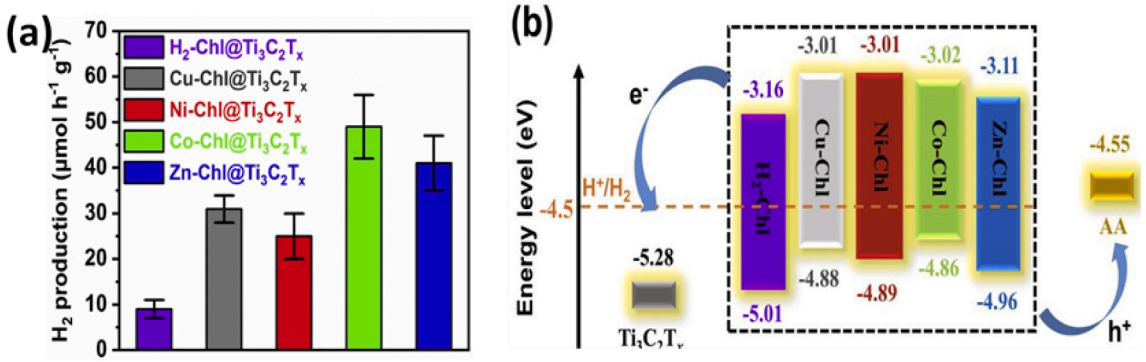

Fig. 28. (a) Optimized Chl-n@$Ti_3C_2T_x$ composites over M-Chl@$Ti_3C_2T_x$ composites: 4% H_2/Cu/Mn/Co-Chl@$Ti_3C_2T_x$ and 2% ZnChl@$Ti_3C_2T_x$. (b) energy level of five M-Chls photo-catalyst. Reprinted with permission from Ref. [127].

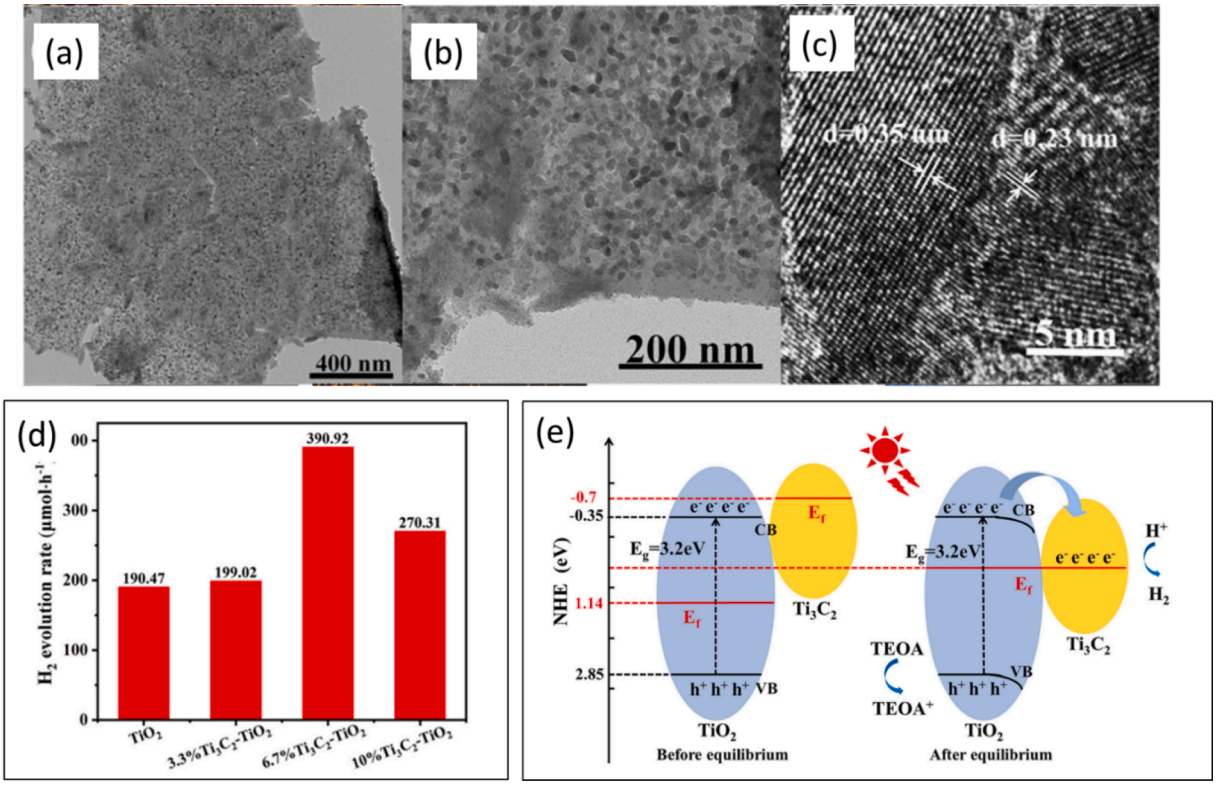

Fig. 29. (a, b, c) TEM image and HRTEM image of Ti_3C_2-TiO_2 composites. (d) The photo-catalytic $H_{2,gen}$ rate over TiO_2 and Ti_3C_2-TiO_2 composites. (e) The mechanism of the photo-catalytic $H_{2,gen}$ under solar light irradiation over Ti_3C_2-TiO_2 composites. Reprinted with permission from Ref. [53].

Furthermore, better separation of photo-induced electrons and holes in TiO_2 increases the HER rate until the composition of monolayer of $Ti_3C_2T_x$ reaches 5.0 wt%, the 5-TC/TO sample generates the highest HER of 2.65 mmol h^{-1} g^{-1}, which is greater than that of pure TiO_2 (0.29 mmol h^{-1} g^{-1}) by 9.1-fold. According to the results, the 2D monolayer $Ti_3C_2T_x$ is better as a co-catalyst for charge separation in TiO_2 than the multilayer $Ti_3C_2T_x$. By HT_O method, in-situ manufacture of Ti_3C_2 MXene embedded with TiO_2 nanosheets (M@TiO_2) a peculiar hierarchical Ti_3C_2 MXene@TiO_2/$ZnIn_2S_4$ (Fig. 31a and b) photo-catalyst with quick charge transfer channels were created for efficient $H_{2,\ gen}$ [138]. The $H_{2,\ gen}$ rate by hybridized photo-catalyst with optimized ZIS quantity was found to be 1185.8 μmol. g^{-1}.h^{-1}, which is higher than that of pure ZIS and M@TiO_2as shown in Fig. 31c and d. This resulted from ZIS and Ti_3C_2′s excellent light harvesting, Ti_3C_2′s ample active sites, effective separation, close interfacial contact and photo-generated charges being transferred through heterojunction. The advantageous methods of charge transfer were Type II heterojunctions between TiO_2 nanosheets and ZIS, Schottky junctions of Ti_3C_2/semiconductor, and high conductivity metallic Ti_3C_2.

Recently, a hydrothermal technique was used to fabricate the ZnCdS/TiO_2/Na-MXene composites [136]. Under hydrothermal conditions, there is a retardation of additional oxidation of Ti_3C_2 MXene to TiO_2, and the usage efficiency of MXene in composite materials is increased. When MB undergoes photo-catalytic degradation using ZnCdS/TiO_2/Na-MXene composites. MXene's great adsorption ability to MB could enhance the degradation efficiency considerably, and as such, a greater MXene content was important. The photo-catalytic reduction activity of Na-doped MXene was boosted even further. ZTNM-3 optimal $H_{2,\ gen}$ efficiency at 8436.58 μmol. g^{-1}.h^{-1} was higher by 3.3-fold in comparison to that of ZnCdS nanoparticles.

Table 2
Typical MXene-derived and MXene-based photo-catalysts with their preparation procedure used for the production of H_2 from W*sp*.

No.	Photo-catalysts	Preparation method	Sacrificial reagent	H_2 production rate ($\mu mol \cdot g^{-1} \cdot h^{-1}$)	Power of Light source (W)	Type	Wavelength	Ref
1	$Ti_3C_2/MoS_2/TiO_2$	two-step hydrothermal method	triethanolamine (TEOA)	6425.297	300 W	Xe arc lamp	> 420 nm	[51]
2	TiO_2/Ti_3C_2	electrostatic self-assembly	Methanol	6979	300	Xe arc lamp	> 420 nm	[133]
3	Monolayer $Ti_3C_2T_x/TiO_2$	sonication	Methanol/ water	2650	200	Hg lamp	285–325 nm cutoff filter	[81]
4	Ti_3C_2-TiO_2	simple two-phase assembling method	triethanolamine	390.92	300	Xe lamp	> 420 nm	[134]
5	TiO_2 nanosheets/C	hydrothermal and annealing	Not mentioned	69	–	visible light irradiation	> 420 nm	[124]
6	small- sized TiO_2/large-sized Ti_3C_2-MXene	ultrasonic treatments	triethanolamine (TEOA)	62.5	300	Xe lamp	> 420 nm	[50]
7	NPT-TiO_2/C (Ti_3C_2TX)	Heating 2 h at 700 °C	Not mentioned	29	–	-visible light-simulated sunlight		[124]
8	Cu/TiO_2@$Ti_3C_2T_x$	HT_O method followed by photo-deposition	methanol	860	300	Xe lamp	> 420 nm	[49]
9	Cu_2O/(0 0 1)TiO_2@$Ti_3C_2T_x$	solvent reduction method	methanol	1496	300	Xe lamp	> 420 nm	[80]
10	Ti_3C_2 MXene@TiO_2/$CuInS_2$ (M@T/CIS)	two-step hydrothermal	methanol	356.27	300	Xe lamp	320 nm ~ 1100 nm	[127]
11	Chl- n/$Ti_3C_2T_x$	Mechanical	ascorbic acid	20	300	Xe lamp	> 420 nm	[118]
12	Co-Chl@$Ti_3C_2T_x$	stirring at room temp		49,000	–	Visible light	λ > 420 nm	[117]
13	$CdLa_2S_4/Ti_3C_2$ MXene	facile hydrothermal	Na_2SO_3 and Na_2S	11182.4	300	Xe lamp	λ > 420 nm	[102]
14	CdS@Mxene	Ultrasonic	Na_2SO_3 and Na_2S	17,500	–	Visible-light, UV filter	400 nm.	[100]
15	1D/2D CdS nanorod@Ti_3C_2	hydrothermal method	Not mentioned	63.53	–	simulated solar light	simulated solar light	[99]
16	CdS@Ti_3C_2@CoO	Ultrasound treatment	No	134.46	300	Xe lamp	λ > 420 nm	[39]
17	1D CdS/2D Ti_3C_2 MXene	electrostatic	lactic acid	2407	300	Xe lamp	λ > 420 nm	[42]
18	TiO_2-C/CdS	alkaline treatment	lactic acid	1480	300	Xe lamp	λ > 420 nm	[43]
19	$Zn_{0.5}Cd_{0.5}S/Ti_2C/TiO_2$	hydrothermal method	Na_2SO_3 and Na_2S	32,570	300 (l 400 nm))	Xe lamp		[128]
20	$Cd_xZn_{1-x}S/Ti_3C_2$ ultrathin MXene	facile electrostatic assembly		15,035.81	–	visible-light	visible-light	[45]
21	$Zn_2In_2S_5/Ti_3C_2(O, OH)_x$	hydrothermal		12,983.80	–	Visible-light	Visible-light	[103]
22	ZnO nanorods/MXene	ultrasonic oscillation	ethanol	456	300	Xe lamp	λ > 420 nm	[135]
23	ZnCdS/TiO_2/Na- Ti_3C_2 MXene	Hydrothermal	lactic acid	8436.58	300 420 nm	Xe lamp	λ > 420 nm	[41]
24	Ti_3C_2 MXene@TiO_2/$ZnIn_2S_4$	two-step hydrothermal	Na_2SO_3 and Na_2S	1185.81	300	Xe lamp	λ > 420 nm	[79]
25	ZnS/ Ti_3C_2 MXene	exfoliation, and solvothermal	lactic acid:water	502.61	300	Xe lamp		[121]
26	ZnS NPs/MXene	ultrasonic oscillation	Not mentioned	212	–	visible light	visible light	[111]
27	Mo_2C MXene/CdS	hydrothermal	lactic acid	17 964	–	visible-light	visible-light	[103]
28	MoS_2/Ti_3C_2	hydrothermal method	methanol	6144.7	300	Xe lamp	> 420 nm	[136]
29	Mo_xS@TiO_2@Ti_3C_2	two-step hydrothermal method	TEOA	10505.8	300 200	Xe lamp	200 to 1200 nm	[112]
30	CdS-MoS_2-MXenes	simple hydrothermal method	Na_2SO_3 and Na_2S	9679	300	Xe lamp	> 420 nm	[94]
31	2D/2D Ti_3C_2 MXene/O-doped g-C_3N_4	electrostatic assembly	triethanolamine	25,124	300	Xe lamp	> 420 nm	[130]
32	TiC/HCN MXene	single step ultrasonic	methanol	310	35	HID lamp	> 420 nm	[137]
33	HCN/Ti_3C_2	ionothermal method	triethanolamine	4225	–	LED lamps	> 420 nm	[113]
34	PtO@Ti_3C_2/TiO_2	sonication	Methanol and water	12,054	–	Xe lamp	365 nm	[120]
35	Ti_3C_2/TiO_2/UiO-66-NH_2	facile hydrothermal	Na_2SO_3 and Na_2S	1980	300	Xe lamp	$350 < l < 780$ nm	[88]
36	2D/2D BiOBr/Ti_3C_2	facile hydrothermal		8.04 mM/g	300	Xe lamp	< 400 nm	[129]
37	2D/2D $Bi_4O_5Br_2$/TL-Ti_3C_2	alcoholysis method	CH_3OH	83.5	300	Xe lamp	420 nm	[131]
38	2D/3D g-C_3N_4/Ti_3C_2 (MXene)	one-step calcination process	triethanolamine	116.2	300	xenon lamp	λ > 420 nm	[138]
39	C-TiO_2/g-C_3N_4	facile heat treatment	triethanolamine	1409		visible light	420 nm	[77]

5. Conclusions and perspective:

Due to intrinsic benefits of high hydrophilicity, metallic conductivity, large surface area, and rich surface functionalities, MXenes have lately garnered widespread interest for electro-catalytic and photo-catalytic W*sp*. This paper summarizes MXenes' fundamental properties, synthesis technique of virgin MXene and its composites, as well as current advances, challenges, and application prospects in photo-catalysis and electro-catalysis. Pure MXenes are limited in their practical application due to their intrinsic low catalytic activity, hazardous

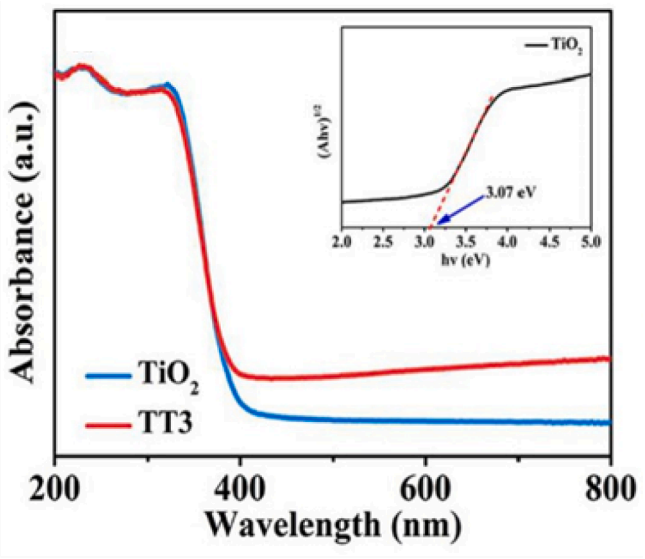

Fig. 30. UV–vis diffuse reflectance spectra and plot of $(Ahv)^{1/2}$ versus energy $(hv)^2$ for TiO_2 band gap energies. Reprinted with permission from Ref. [55].

production method and poor environmental stability. To overcome the aforementioned defects, we summarized the main topics to explore in future research on the route to industrial-scale applications of MXenes-based materials for electro and photo-catalytic W*sp*.

Firstly, wet-chemical etching is the most frequent method of MXene production, even though it requires the usage of a deleterious and corrosive HF-based etchant. The preparation of MXene as well as the disposal of MXene-based items have a detrimental influence on the environment. As a result, new ecologically friendly and safer preparation methods should be investigated. Furthermore, MXenes are more quickly oxidized under severe circumstances due to a large number of metal atoms that are exposed at the surface. MXenes' structure and metallic conductivity can be destroyed by oxidation, which should be considered to prevent oxidation of Mxenes at high temperatures and pressure. The appropriate preparation procedures may be chosen based on the qualities and needs of the materials to attain an optimized performance. Secondly, numerous research has demonstrated that nitride-based MXenes have numerous promising benefits over their carbide-based Mxenes, including aqueous medium stability and excellent conductivity. Unlike carbide MXenes, which have received substantial research in electro-catalytic and photo-catalytic W*sp*, nitride MXenes have received just a few experimental observations. The main research focus should be geared towards the appropriate preparation procedures and functions of nitride MXenes in photo-catalytic and electro-catalytic W*sp*. To expand the MXene family, new varieties of MXene must be produced. Thirdly, MXene surface terminals influence catalytic activity. A single surface terminal group (e.g. -CL, –F, or –OH) should be uniform and regulated. Lastly, MXene can act as a receiver of electrons and offer a pathway for connecting with other photo-catalysts and electro-catalysts to achieve outstanding efficiency, as such, the development of heterojunction composites that are MXene-based with optimal photo-catalytic and electro-catalytic performance is a priority. MXenes' 2D structure and certain surface terminations allow the creation of 2D/2D designs, as well as heterojunctions that are low-dimensional (0D/2D and 1D/2D) and 3D architectures for improved photo-catalytic and electro-catalytic activity.

MXene-TiO_2 derived materials can have a different structure that acts as co-catalysts with schottky junction of electrically conductive Ti_3C_2 and optically active TiO_2, which can overturn the charge recombination and exhibit high Cat_A under irradiation with visible and UV light. In such combinations, MXene-TiO_2 provides a layered platform to stimulate the photo-generated charge separation. Future research perspectives of electro and photo-catalytic $H_{2,gen}$ over MXene-based materials are as follows:

1. It is critical to select the right conditions and procedure to synthesize the desired MXene-derived materials for different application
2. Most of the studied MXene derivatives were based on mono-metal MXene, with only a few cases involving bimetallic-MXene. As a result, more research work on bimetal MXene and its derivative should be investigated. Monolayer MXene-derived materials can efficiently improve the photo- Cat_A by shortening the charge transportation pathway. As a result, research in this area is eagerly anticipated.
3. MXenes-metal oxide nanocomposite has interesting intensifying properties with limitless potential in various fields. As a result, it is expected that a large number of MXenes-metal oxide nanocomposite will be investigated in the near future.
4. Strategies for improving the effectiveness of the MXene-based nanocomposites system should be pursued, including a thorough investigation of the fundamental mechanistic path for charge separation in relation to catalytic activity. MXene/ TiO_2 nanohybrids were proposed in different photo-catalytic applications as a result of the easy synthesis procedure, improved. Smaller interlayer spacing and enhanced optical absorbability. Nonetheless, the performance of MXene based composites I still low compared with derived systems in photo-catalytic applications. Such strategies should focus on improving the overall process performance

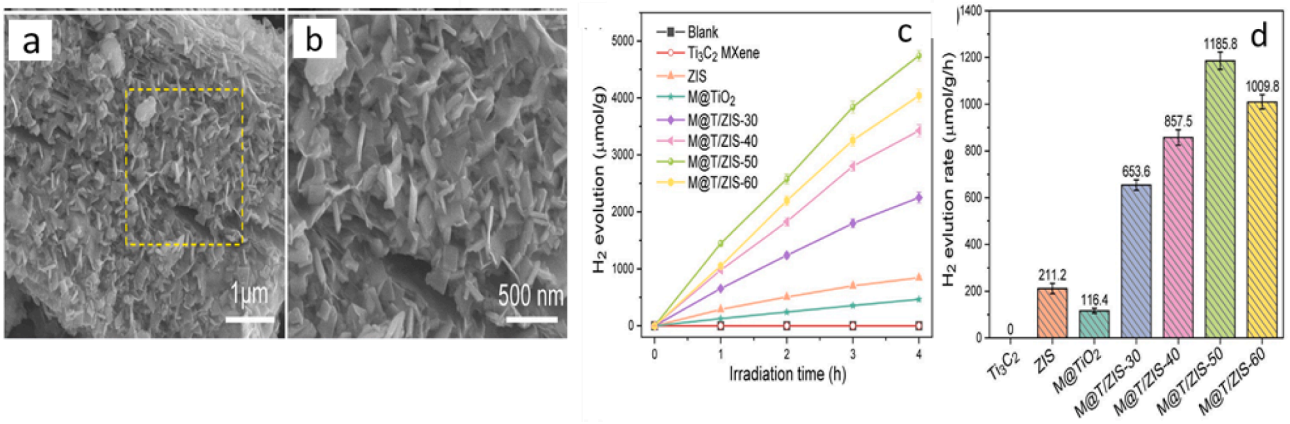

Fig. 31. FESEM images of (a, b) M@T/ZIS-50; (c) photo-catalytic $H_{2,gen}$ over different M@T/ZIS-50 photo-catalysts, (d) corresponding $H_{2,gen}$ rate. Reprinted with permission from Ref. [138].

5. Future research should concentrate on combining MXenes with various semiconducting materials such as g-C3N4, CeO2, ZnO, MoS2, and BiVO4 to improve photocatalytic performance.
6. The advancement 2D MXenes materials deliver has a promising future as electrode material in energy storage devices due to several advantages such as avoiding the problem of restacking, improved electronic conductivity and stability, easy ion/electron transfer and their hydrophilic surfaces. As a result, it is concluded that future advancements in the synthesis of MXene should focus on this kind of application. The development of MXene-based material with an effective interlayer distance that enhances energy storage is highly recommended. MXene hybrid material would pave the way for further research into energy storage applications.

CRediT authorship contribution statement

Fares Almomani: Conceptualization, Project administration, Supervision, Investigation, Methodology, Data curation, Writing – original draft, Writing – review & editing. **Amani Al-Rababah:** Investigation, Data curation, Formal analysis, Writing – original draft, Writing – review & editing. **Muhammad Tawalbeh:** Conceptualization, Project administration, Investigation, Methodology, Formal analysis, Writing – original draft, Writing – review & editing. **Amani Al-Othman:** Conceptualization, Methodology, Investigation, Formal analysis, Writing – original draft, Writing – review & editing.

Declaration of Competing Interest

The authors declare that they have no known competing financial interests or personal relationships that could have appeared to influence the work reported in this paper.

Data availability

Data will be made available on request.

Acknowledgments

The authors would like to acknowledge the financial support from the University of Sharjah, United Arab Emirates, through the seed research grant project number: 1702040663-P.

References

[1] Qureshi F, Yusuf M, Pasha AA, Khan HW, Imteyaz B, Irshad K. Sustainable and energy efficient hydrogen production via glycerol reforming techniques: a review. Int J Hydrogen Energy 2022.
[2] Yusuf M, Farooqi AS, Keong LK, Hellgardt K, Abdullah B. Contemporary trends in composite Ni-based catalysts for CO2 reforming of methane. Chem Eng Sci 2021;229:116072.
[3] Wei J, Zhou M, Long A, Xue Y, Liao H, Wei C, et al. Heterostructured electrocatalysts for hydrogen evolution reaction under alkaline conditions. Nano-micro letters 2018;10(4):1–15.
[4] Rosdin RDb, Yusuf M, Abdullah B. Dry reforming of methane over Ni-based catalysts: Effect of ZrO2 and MgO addition as support. Materials Letters: X 2021;12:100095.
[5] Zheng Y, Jiao Y, Jaroniec M, Qiao SZ. Advancing the electrochemistry of the hydrogen-evolution reaction through combining experiment and theory. Angew Chem Int Ed 2015;54(1):52–65.
[6] Debe MK. Electrocatalyst approaches and challenges for automotive fuel cells. Nature 2012;486(7401):43–51.
[7] Yusuf M, Bazli L, Alam MA, Masood F, Keong LK, Noor A, et al. Hydrogen production via natural gas reforming: A comparative study between DRM, SRM and BRM techniques. 2021 Third International Sustainability and Resilience Conference: Climate Change. 2021:155-8.
[8] Chen Z, Duan X, Wei W, Wang S, Ni B-J. Recent advances in transition metal-based electrocatalysts for alkaline hydrogen evolution. J Mater Chem A 2019;7(25):14971–5005.
[9] You B, Sun Y. Innovative Strategies for Electrocatalytic Water Splitting. Acc Chem Res 2018;51(7):1571–80.
[10] Du C-F, Liang Q, Dangol R, Zhao J, Ren H, Madhavi S, et al. Layered trichalcogenidophosphate: a new catalyst family for water splitting. Nano-Micro Lett 2018;10(4):1–15.
[11] Wei Y, Soomro RA, Xie X, Xu B. Design of efficient electrocatalysts for hydrogen evolution reaction based on 2D MXenes. J Energy Chem 2021;55:244–55.
[12] Lim KRG, Handoko AD, Nemani SK, Wyatt B, Jiang H-Y, Tang J, et al. Rational design of two-dimensional transition metal carbide/nitride (MXene) hybrids and nanocomposites for catalytic energy storage and conversion. ACS Nano 2020;14(9):10834–64.
[13] Zhao G, Li P, Cheng N, Dou SX, Sun W. An Ir/Ni (OH) 2 heterostructured electrocatalyst for the oxygen evolution reaction: breaking the scaling relation, stabilizing iridium (V), and beyond. Adv Mater 2020;32(24):2000872.
[14] Di J, Yan C, Handoko AD, Seh ZW, Li H, Liu ZJMT. Ultrathin two-dimensional materials for photo-and electrocatalytic hydrogen evolution. 2018;21(7):749-70.
[15] Prasad C, Yang X, Liu Q, Tang H, Rammohan A, Zulfiqar S, et al. Recent advances in MXenes supported semiconductors based photocatalysts: properties, synthesis and photocatalytic applications. J Ind Eng Chem 2020;85:1–33.
[16] Cheng L, Li X, Zhang H, Xiang Q. Two-dimensional transition metal MXene-based photocatalysts for solar fuel generation. J Phys Chem Lett 2019;10(12):3488–94.
[17] Novoselov KS, Geim AK, Morozov SV, Jiang D-e, Zhang Y, Dubonos SV, et al. Electric field effect in atomically thin carbon films. Science 2004;306(5696):666–9.
[18] Berkani M, Smaali A, Almomani F, Vasseghian Y. Recent advances in MXene-based nanomaterials for desalination at water interfaces. Environ Res 2022;203:111845.
[19] Zhang L, Ji X, Ren X, Ma Y, Shi X, Tian Z, et al. Electrochemical ammonia synthesis via nitrogen reduction reaction on a MoS2 catalyst: theoretical and experimental studies. Adv Mater 2018;30(28):1800191.
[20] Jin C, Regan EC, Yan A, Iqbal Bakti Utama M, Wang D, Zhao S, et al. Observation of moiré excitons in WSe2/WS2 heterostructure superlattices. Nature 2019;567(7746):76–80.
[21] Jiang L, Li J, Wang K, Zhang G, Li Y, Wu XJACBE. Low boiling point solvent mediated strategy to synthesize functionalized monolayer carbon nitride for superior photocatalytic hydrogen evolution. 2020;260:118181.
[22] Wang K, Li Y, Li J, Zhang G. Boosting interfacial charge separation of Ba5Nb4O15/g-C3N4 photocatalysts by 2D/2D nanojunction towards efficient visible-light driven H2 generation. Appl Catal B 2020;263:117730.
[23] Liu J, Zhang G. Recent advances in synthesis and applications of clay-based photocatalysts: a review. PCCP 2014;16(18):8178–92.
[24] Yu J, Wang Q, O'Hare D, Sun L. Preparation of two dimensional layered double hydroxide nanosheets and their applications. Chem Soc Rev 2017;46(19):5950–74.
[25] Al-Othman A, Hassan MF, Tawalbeh M, Ka'ki A. Proton conductivity studies in zirconium phosphate/MXenes in PEM fuel cells. In: 2022 Advances in Science and Engineering Technology International Conferences (ASET); 2022. p. 1–5.
[26] Nauman Javed RM, Al-Othman A, Tawalbeh M, Olabi AG. Recent developments in graphene and graphene oxide materials for polymer electrolyte membrane fuel cells applications. Renew Sustain Energy Rev 2022;168:112836.
[27] Tawalbeh M, Muhammad Nauman Javed R, Al-Othman A, Almomani F. The novel advancements of nanomaterials in biofuel cells with a focus on electrodes' applications. Fuel 2022;322:124237.
[28] Al-Othman A, Tawalbeh M, Martis R, Dhou S, Orhan M, Qasim M, et al. Artificial intelligence and numerical models in hybrid renewable energy systems with fuel cells: Advances and prospects. Energy Convers Manage 2022;253:115154.
[29] Wang K, Zhang G, Li J, Li Y, Wu X. 0D/2D Z-scheme heterojunctions of bismuth tantalate quantum dots/ultrathin g-C3N4 nanosheets for highly efficient visible light photocatalytic degradation of antibiotics. ACS Appl Mater Interfaces 2017;9(50):43704–15.
[30] Chia X, Pumera M. Characteristics and performance of two-dimensional materials for electrocatalysis. Nat Catal 2018;1(12):909–21.
[31] Wang Y, Mao J, Meng X, Yu L, Deng D, Bao X. Catalysis with two-dimensional materials confining single atoms: concept, design, and applications. Chem Rev 2018;119(3):1806–54.
[32] Vasseghian Y, Dragoi E-N, Almomani F, Le VT. A comprehensive review on MXenes as new nanomaterials for degradation of hazardous pollutants: Deployment as heterogeneous sonocatalysis. Chemosphere 2022;287:132387.
[33] Wang K, Li J, Zhang G. Ag-bridged Z-scheme 2D/2D Bi5FeTi3O15/g-C3N4 heterojunction for enhanced photocatalysis: mediator-induced interfacial charge transfer and mechanism insights. ACS Appl Mater Interfaces 2019;11(31):27686–96.
[34] Naguib M, Kurtoglu M, Presser V, Lu J, Niu J, Heon M, et al. Two-dimensional nanocrystals produced by exfoliation of Ti3AlC2. Adv Mater 2011;23(37):4248–53.
[35] Naguib M, Mochalin VN, Barsoum MW, Gogotsi Y. 25th anniversary article: MXenes: a new family of two-dimensional materials. Adv Mater 2014;26(7):992–1005.
[36] VahidMohammadi A, Rosen J, Gogotsi Y. The world of two-dimensional carbides and nitrides (MXenes). Science 2021;372(6547):eabf1581.
[37] Ghidiu M, Lukatskaya MR, Zhao M-Q, Gogotsi Y, Barsoum MW. Conductive two-dimensional titanium carbide 'clay'with high volumetric capacitance. Nature 2014;516(7529):78–81.
[38] Peng J, Chen X, Ong W-J, Zhao X, Li NJC. Surface and heterointerface engineering of 2D MXenes and their nanocomposites: insights into electro-and photocatalysis. 2019;5(1):18-50.

[39] Ronchi RM, Arantes JT, Santos SF. Synthesis, structure, properties and applications of MXenes: current status and perspectives. Ceram Int 2019;45(15):18167–88.
[40] Sinopoli A, Othman Z, Rasool K, Mahmoud KA. Electrocatalytic/photocatalytic properties and aqueous media applications of 2D transition metal carbides (MXenes). Curr Opin Solid State Mater Sci 2019;23(5):100760.
[41] Yu H, Wang Y, Jing Y, Ma J, Du CF, Yan Q. Surface modified MXene-based nanocomposites for electrochemical energy conversion and storage. Small 2019;15(25):1901503.
[42] Luo J, Matios E, Wang H, Tao X, Li W. Interfacial structure design of MXene-based nanomaterials for electrochemical energy storage and conversion. InfoMat 2020;2(6):1057–76.
[43] Kong A, Peng M, Gu H, Zhao S, Lv Y, Liu M, et al. Synergetic control of Ru/MXene 3D electrode with superhydrophilicity and superaerophobicity for overall water splitting. Chem Eng J 2021;426:131234.
[44] Ning X, Wu Y, Ma X, Zhang Z, Gao R, Chen J, et al. A novel charge transfer channel to simultaneously enhance photocatalytic water splitting activity and stability of CdS. 2019;29(40):1902992.
[45] Liu X, Liu Q, Chen C. Ultrasonic oscillation synthesized ZnS nanoparticles/layered MXene sheet with outstanding photocatalytic activity under visible light. Vacuum 2021;183:109834.
[46] Wang J, Chen J, Wang P, Hou J, Wang C, Ao Y. Robust photocatalytic hydrogen evolution over amorphous ruthenium phosphide quantum dots modified g-C3N4 nanosheet. Appl Catal B 2018;239:578–85.
[47] Chang H, Li X, Shi L, Zhu Y-R, Yi T-FJCEJ. Towards high-performance electrocatalysts and photocatalyst: Design and construction of MXenes-based nanocomposites for water splitting. 2021:129944.
[48] Chen R, Wang P, Chen J, Wang C, Ao Y. Synergetic effect of MoS2 and MXene on the enhanced H2 evolution performance of CdS under visible light irradiation. Appl Surf Sci 2019;473:11–9.
[49] Huang J-J, Liu X-Q, Meng F-F, He L-Q, Wang J-X, Wu J-C, et al. A facile method to produce MoSe2/MXene hybrid nanoflowers with enhanced electrocatalytic activity for hydrogen evolution. J Electroanal Chem 2020;856:113727.
[50] Tie L, Yang S, Yu C, Chen H, Liu Y, Dong S, et al. In situ decoration of ZnS nanoparticles with Ti3C2 MXene nanosheets for efficient photocatalytic hydrogen evolution. J Colloid Interface Sci 2019;545:63–70.
[51] Xiao R, Zhao C, Zou Z, Chen Z, Tian L, Xu H, et al. In situ fabrication of 1D CdS nanorod/2D Ti3C2 MXene nanosheet Schottky heterojunction toward enhanced photocatalytic hydrogen evolution. Appl Catal B 2020;268:118382.
[52] Wang J, He P, Shen Y, Dai L, Li Z, Wu Y, et al. FeNi nanoparticles on Mo2TiC2Tx MXene@ nickel foam as robust electrocatalysts for overall water splitting. Nano Res 2021;14(10):3474–81.
[53] Zong S, Liu J, Huang Z, Liu L, Liu J, Zheng J, et al. Mxene-TiO2 composite with exposed 101 facets for the improved photocatalytic hydrogen evolution activity. J Alloy Compd 2022;896:163039.
[54] Lin P, Shen J, Yu X, Liu Q, Li D, Tang H. Construction of Ti3C2 MXene/O-doped g-C3N4 2D–2D Schottky-junction for enhanced photocatalytic hydrogen evolution. Ceram Int 2019;45(18):24656–63.
[55] Zhuang Y, Liu Y, Meng X. Fabrication of TiO2 nanofibers/MXene Ti3C2 nanocomposites for photocatalytic H2 evolution by electrostatic self-assembly. Appl Surf Sci 2019;496:143647.
[56] Zheng S, Peng S, Wang Z, Huang J, Luo X, Han L, et al. Schottky-structured 0D/2D composites via electrostatic self-assembly for efficient photocatalytic hydrogen evolution. Ceram Int 2021;47(20):28304–11.
[57] Peng C, Wei P, Li X, Liu Y, Cao Y, Wang H, et al. High efficiency photocatalytic hydrogen production over ternary Cu/TiO2@ Ti3C2Tx enabled by low-work-function 2D titanium carbide. Nano Energy 2018;53:97–107.
[58] Li Y, Yin Z, Ji G, Liang Z, Xue Y, Guo Y, et al. 2D/2D/2D heterojunction of Ti3C2 MXene/MoS2 nanosheets/TiO2 nanosheets with exposed (001) facets toward enhanced photocatalytic hydrogen production activity. Appl Catal B 2019;246:12–20.
[59] Li J, Zhao L, Wang S, Li J, Wang G, Wang J. In situ fabrication of 2D/3D g-C3N4/Ti3C2 (MXene) heterojunction for efficient visible-light photocatalytic hydrogen evolution. Appl Surf Sci 2020;515:145922.
[60] He L, Liu J, Liu Y, Cui B, Hu B, Wang M, et al. Titanium dioxide encapsulated carbon-nitride nanosheets derived from MXene and melamine-cyanuric acid composite as a multifunctional electrocatalyst for hydrogen and oxygen evolution reaction and oxygen reduction reaction. Appl Catal B 2019;248:366–79.
[61] Yu M, Wang Z, Liu J, Sun F, Yang P, Qiu J. A hierarchically porous and hydrophilic 3D nickel–iron/MXene electrode for accelerating oxygen and hydrogen evolution at high current densities. Nano Energy 2019;63:103880.
[62] Jiang Y, Sun T, Xie X, Jiang W, Li J, Tian B, et al. Oxygen-functionalized ultrathin Ti3C2Tx MXene for enhanced electrocatalytic hydrogen evolution. ChemSusChem 2019;12(7):1368–73.
[63] Zhang J, Zhao Y, Guo X, Chen C, Dong C-L, Liu R-S, et al. Single platinum atoms immobilized on an MXene as an efficient catalyst for the hydrogen evolution reaction. Nat Catal 2018;1(12):985–92.
[64] Kuznetsov DA, Chen Z, Kumar PV, Tsoukalou A, Kierzkowska A, Abdala PM, et al. Single site cobalt substitution in 2D molybdenum carbide (MXene) enhances catalytic activity in the hydrogen evolution reaction. J Am Chem Soc 2019;141(44):17809–16.
[65] Cui C, Cheng R, Zhang H, Zhang C, Ma Y, Shi C, et al. Ultrastable MXene@ Pt/SWCNTs' nanocatalysts for hydrogen evolution reaction. Adv Funct Mater 2020;30(47):2000693.
[66] Yuan Y, Li H, Wang L, Zhang L, Shi D, Hong Y, et al. Achieving highly efficient catalysts for hydrogen evolution reaction by electronic state modification of platinum on versatile Ti3C2T x (MXene). ACS Sustainable Chem Eng 2019;7(4):4266–73.
[67] Jiao Y, Zheng Y, Jaroniec M, Qiao SZ. Design of electrocatalysts for oxygen-and hydrogen-involving energy conversion reactions. Chem Soc Rev 2015;44(8):2060–86.
[68] Zhong X, Tang J, Wang J, Shao M, Chai J, Wang S, et al. 3D heterostructured pure and N-doped Ni3S2/VS2 nanosheets for high efficient overall water splitting. Electrochim Acta 2018;269:55–61.
[69] Zhong X, Zhang L, Tang J, Chai J, Xu J, Cao L, et al. Efficient coupling of a hierarchical V 2 O 5@ Ni 3 S 2 hybrid nanoarray for pseudocapacitors and hydrogen production. J Mater Chem A 2017;5(34):17954–62.
[70] Bai X, Ling C, Shi L, Ouyang Y, Li Q, Wang J. Insight into the catalytic activity of MXenes for hydrogen evolution reaction. Sci Bull 2018;63(21):1397–403.
[71] Li S, Tuo P, Xie J, Zhang X, Xu J, Bao J, et al. Ultrathin MXene nanosheets with rich fluorine termination groups realizing efficient electrocatalytic hydrogen evolution. Nano Energy 2018;47:512–8.
[72] Tan Y, Zhu Z, Zhang X, Zhang J, Zhou Y, Li H, et al. Nb4C3Tx (MXene) as a new stable catalyst for the hydrogen evolution reaction. Int J Hydrogen Energy 2021;46(2):1955–66.
[73] Gao G, O'Mullane AP, Du A. 2D MXenes: a new family of promising catalysts for the hydrogen evolution reaction. ACS Catal 2017;7(1):494–500.
[74] Intikhab S, Natu V, Li J, Li Y, Tao Q, Rosen J, et al. Stoichiometry and surface structure dependence of hydrogen evolution reaction activity and stability of MoxC MXenes. J Catal 2019;371:325–32.
[75] Liang J, Ding C, Liu J, Chen T, Peng W, Li Y, et al. Heterostructure engineering of Co-doped MoS2 coupled with Mo2CTx MXene for enhanced hydrogen evolution in alkaline media. Nanoscale 2019;11(22):10992–1000.
[76] Khan R, Mehran MT, Naqvi SR, Khoja AH, Baig MM, Akram MA, et al. A highly efficient A-site deficient perovskite interlaced within two dimensional MXene nanosheets as an active electrocatalyst for hydrogen production. International Journal of Hydrogen Energy 2021.
[77] Zhang X, Shao B, Sun Z, Gao Z, Qin Y, Zhang C, et al. Platinum nanoparticle-deposited Ti3C2T x MXene for hydrogen evolution reaction. Ind Eng Chem Res 2020;59(5):1822–8.
[78] Kuang P, He M, Zhu B, Yu J, Fan K, Jaroniec M. 0D/2D NiS2/V-MXene composite for electrocatalytic H2 evolution. J Catal 2019;375:8–20.
[79] Zong H, Yu K, Zhu Z. Heterostructure nanohybrids of Ni-doped MoSe2 coupled with Ti2NTx toward efficient overall water splitting. Electrochim Acta 2020;353:136598.
[80] Li X, Lv X, Sun X, Yang C, Zheng Y-Z, Yang L, et al. Edge-oriented, high-percentage 1T′-phase MoS2 nanosheets stabilize Ti3C2 MXene for efficient electrocatalytic hydrogen evolution. Appl Catal B 2021;284:119708.
[81] Lim KRG, Handoko AD, Johnson LR, Meng X, Lin M, Subramanian GS, et al. 2h-Mos2 on Mo2ct X Mxene nanohybrid for efficient and durable electrocatalytic hydrogen evolution. ACS Nano 2020;14(11):16140–55.
[82] Wang Z, Yu K, Feng Y, Qi R, Ren J, Zhu Z. Stabilizing Ti3C2Tx-MXenes with TiOF2 nanospheres intercalation to improve hydrogen evolution reaction and humidity-sensing performance. Appl Surf Sci 2019;496:143729.
[83] Ling C, Shi L, Ouyang Y, Chen Q, Wang J. Transition metal-promoted V2CO2 (MXenes): a new and highly active catalyst for hydrogen evolution reaction. Adv Sci 2016;3(11):1600180.
[84] Yuan W, Cheng L, An Y, Wu H, Yao N, Fan X, et al. MXene nanofibers as highly active catalysts for hydrogen evolution reaction. ACS Sustainable Chem Eng 2018;6(7):8976–82.
[85] Yu J, Zhou W, Xiong T, Wang A, Chen S, Chu B. Enhanced electrocatalytic activity of Co@ N-doped carbon nanotubes by ultrasmall defect-rich TiO2 nanoparticles for hydrogen evolution reaction. Nano Res 2017;10(8):2599–609.
[86] Deng S, Zhong Y, Zeng Y, Wang Y, Wang X, Lu X, et al. Hollow TiO2@ Co9S8 core–branch arrays as bifunctional electrocatalysts for efficient oxygen/hydrogen production. Adv Sci 2018;5(3):1700772.
[87] Tsai C, Abild-Pedersen F, Nørskov JK. Tuning the MoS2 edge-site activity for hydrogen evolution via support interactions. Nano Lett 2014;14(3):1381–7.
[88] Hinnemann B, Moses PG, Bonde J, Jørgensen KP, Nielsen JH, Horch S, et al. Biomimetic hydrogen evolution: MoS2 nanoparticles as catalyst for hydrogen evolution. J Am Chem Soc 2005;127(15):5308–9.
[89] Zhang H, Zuo S, Qiu M, Wang S, Zhang Y, Zhang J, et al. Direct probing of atomically dispersed Ru species over multi-edged TiO2 for highly efficient photocatalytic hydrogen evolution. Sci Adv 2020;6(39):eabb9823.
[90] Meng A, Zhang L, Cheng B, Yu J. Dual cocatalysts in TiO2 photocatalysis. Adv Mater 2019;31(30):1807660.
[91] Tahir M, Tasleem S, Tahir B. Recent development in band engineering of binary semiconductor materials for solar driven photocatalytic hydrogen production. Int J Hydrogen Energy 2020;45(32):15985–6038.
[92] Zhang H, Dong Y, Zhao S, Wang G, Jiang P, Zhong J, et al. Photochemical preparation of atomically dispersed nickel on cadmium sulfide for superior photocatalytic hydrogen evolution. Appl Catal B 2020;261:118233.
[93] Sharifian K, Mahdikhah V, Sheibani S. Ternary Ag@ SrTiO3@ CNT plasmonic nanocomposites for the efficient photodegradation of organic dyes under the visible light irradiation. Ceram Int 2021;47(16):22741–52.
[94] Zhang J, Xing C, Shi F. MoS2/Ti3C2 heterostructure for efficient visible-light photocatalytic hydrogen generation. Int J Hydrogen Energy 2020;45(11):6291–301.
[95] Tian P, He X, Zhao L, Li W, Fang W, Chen H, et al. Enhanced charge transfer for efficient photocatalytic H2 evolution over UiO-66-NH2 with annealed Ti3C2Tx MXenes. Int J Hydrogen Energy 2019;44(2):788–800.

[96] Hu H, Qian D, Lin P, Ding Z, Cui C. Oxygen vacancies mediated in-situ growth of noble-metal (Ag, Au, Pt) nanoparticles on 3D TiO2 hierarchical spheres for efficient photocatalytic hydrogen evolution from water splitting. international journal of hydrogen energy 2020;45(1):629–39.
[97] Sun Y, Jin D, Sun Y, Meng X, Gao Y, Dall'Agnese Y, et al. gC 3 N 4/Ti 3 C 2 T x (MXenes) composite with oxidized surface groups for efficient photocatalytic hydrogen evolution. J Mater Chem A 2018;6(19):9124–31.
[98] Xie X, Zhang N, Tang Z-R, Anpo M, Xu Y-J. Ti3C2Tx MXene as a Janus cocatalyst for concurrent promoted photoactivity and inhibited photocorrosion. Appl Catal B 2018;237:43–9.
[99] Zhu X-D, Xie Y, Liu Y-T. Exploring the synergy of 2D MXene-supported black phosphorus quantum dots in hydrogen and oxygen evolution reactions. J Mater Chem A 2018;6(43):21255–60.
[100] Cai T, Wang L, Liu Y, Zhang S, Dong W, Chen H, et al. Ag3PO4/Ti3C2 MXene interface materials as a Schottky catalyst with enhanced photocatalytic activities and anti-photocorrosion performance. Appl Catal B 2018;239:545–54.
[101] Ji L, Zhou S, Liu X, Gong M, Xu T. Synthesis of carbon-and nitrogen-doped TiO2/carbon composite fibers by a surface-hydrolyzed PAN fiber and their photocatalytic property. J Mater Sci 2020;55(6):2471–81.
[102] Liu H, Wang C, Wang G. Photocatalytic advanced oxidation processes for water treatment: recent advances and perspective. Chem Asian J 2020;15(20):3239–53.
[103] Ji L, Qin X, Zheng J, Zhou S, Xu T, Shi G. Synthesis of Ag–Carbon–TiO2 composite tubes and their antibacterial and organic degradation properties. J Sol-Gel Sci Technol 2020;93(2):291–301.
[104] Nguyen TP, Nguyen DMT, Le HK, Vo D-VN, Lam SS, Varma RS, et al. MXenes: Applications in electrocatalytic, photocatalytic hydrogen evolution reaction and CO2 reduction. Molecular Catalysis 2020;486:110850.
[105] Sun B, Qiu P, Liang Z, Xue Y, Zhang X, Yang L, et al. The fabrication of 1D/2D CdS nanorod@ Ti3C2 MXene composites for good photocatalytic activity of hydrogen generation and ammonia synthesis. Chem Eng J 2021;406:127177.
[106] Zhang H, Li Y, Li W, Zhuang C, Gao C, Jiang W, et al. Designing large-sized cocatalysts for fast charge separation towards highly efficient visible-light-driven hydrogen evolution. Int J Hydrogen Energy 2021;46(56):28545–53.
[107] Jin S, Shi Z, Jing H, Wang L, Hu Q, Chen D, et al. Mo2C-MXene/CdS heterostructures as visible-light photocatalysts with an ultrahigh hydrogen production rate. ACS Applied Energy Materials 2021;4(11):12754–66.
[108] Cheng L, Chen Q, Li J, Liu H. Boosting the photocatalytic activity of CdLa2S4 for hydrogen production using Ti3C2 MXene as a co-catalyst. Appl Catal B 2020;267:118379.
[109] Zhou W, Yin Z, Du Y, Huang X, Zeng Z, Fan Z, et al. Synthesis of few-layer MoS2 nanosheet-coated TiO2 nanobelt heterostructures for enhanced photocatalytic activities. small 2013;9(1):140–7.
[110] Wang H, Sun Y, Wu Y, Tu W, Wu S, Yuan X, et al. Electrical promotion of spatially photoinduced charge separation via interfacial-built-in quasi-alloying effect in hierarchical Zn2In2S5/Ti3C2 (O, OH) x hybrids toward efficient photocatalytic hydrogen evolution and environmental remediation. Appl Catal B 2019;245:290–301.
[111] Chang K, Li M, Wang T, Ouyang S, Li P, Liu L, et al. Drastic layer-number-dependent activity enhancement in photocatalytic H2 evolution over nMoS2/CdS (n≥ 1) under visible light. Adv Energy Mater 2015;5(10):1402279.
[112] Chen W-F, Wang C-H, Sasaki K, Marinkovic N, Xu W, Muckerman JT, et al. Highly active and durable nanostructured molybdenum carbide electrocatalysts for hydrogen production. Energy Environ Sci 2013;6(3):943–51.
[113] Ghassemi H, Harlow W, Mashtalir O, Beidaghi M, Lukatskaya M, Gogotsi Y, et al. In situ environmental transmission electron microscopy study of oxidation of two-dimensional Ti 3 C 2 and formation of carbon-supported TiO 2. J Mater Chem A 2014;2(35):14339–43.
[114] Splendiani A, Sun L, Zhang Y, Li T, Kim J, Chim C-Y, et al. Emerging photoluminescence in monolayer MoS2. Nano Lett 2010;10(4):1271–5.
[115] Xie J, Zhang H, Li S, Wang R, Sun X, Zhou M, et al. Defect-rich MoS2 ultrathin nanosheets with additional active edge sites for enhanced electrocatalytic hydrogen evolution. Adv Mater 2013;25(40):5807–13.
[116] Bai S, Zhang N, Gao C, Xiong Y. Defect engineering in photocatalytic materials. Nano Energy 2018;53:296–336.
[117] Liu S, Li F, Wang D, Huang C, Zhao Y, Baek JB, et al. 3D macroporous MoxC@ N-C with incorporated Mo vacancies as anodes for high-performance lithium-ion batteries. Small Methods 2018;2(8):1800040.
[118] Li Y, Ding L, Liang Z, Xue Y, Cui H, Tian J. Synergetic effect of defects rich MoS2 and Ti3C2 MXene as cocatalysts for enhanced photocatalytic H2 production activity of TiO2. Chem Eng J 2020;383:123178.
[119] Yang J-X, Yu W-B, Li C-F, Dong W-D, Jiang L-Q, Zhou N, et al. PtO nanodots promoting Ti3C2 MXene in-situ converted Ti3C2/TiO2 composites for photocatalytic hydrogen production. Chem Eng J 2021;420:129695.
[120] Peng C, Xu W, Wei P, Liu M, Guo L, Wu P, et al. Manipulating photocatalytic pathway and activity of ternary Cu2O/(001) TiO2@ Ti3C2Tx catalysts for H2 evolution: effect of surface coverage. Int J Hydrogen Energy 2019;44(57):29975–85.
[121] Han X, An L, Hu Y, Li Y, Hou C, Wang H, et al. Ti3C2 MXene-derived carbon-doped TiO2 coupled with g-C3N4 as the visible-light photocatalysts for photocatalytic H2 generation. Appl Catal B 2020;265:118539.
[122] Li J, Li J, Wu C, Li Z, Cai L, Tang H, et al. Crystalline carbon nitride anchored on MXene as an ordered Schottky heterojunction photocatalyst for enhanced visible-light hydrogen evolution. Carbon 2021;179:387–99.
[123] Tahir M. Investigating the influential effect of etchant time in constructing 2 D/2D HCN/MXene heterojunction with controlled growth of TiO2 NPs for stimulating photocatalytic H2 production. Energy Fuels 2021;35(8):6807–22.
[124] Qiu N, Jiang D, Wang X, Wang B, Zhou F. Advances in the members and biosynthesis of chlorophyll family. Photosynthetica 2019;57(4):974–84.
[125] Voloshin RA, Brady NG, Zharmukhamedov SK, Feyziyev YM, Huseynova IM, Najafpour MM, et al. Influence of osmolytes on the stability of thylakoid-based dye-sensitized solar cells. Int J Energy Res 2019;43(14):8878–89.
[126] Ryan AA, Senge MO. How green is green chemistry? Chlorophylls as a bioresource from biorefineries and their commercial potential in medicine and photovoltaics. Photochem Photobiol Sci 2015;14(4):638–60.
[127] Li Y, Zheng T, Liu Y, Dall'Agnese Y, Dall'Agnese C, Liu C-L, et al. Chlorophyll derivatives/MXene hybrids for photocatalytic hydrogen evolution: dependence of performance on the central coordinating metals. Int J Hydrogen Energy 2022;47(6):3824–33.
[128] Li Y, Liu Y, Sun X, Zheng T, Dall'Agnese Y, Dall'Agnese C, et al. Aggregate-forming semi-synthetic chlorophyll derivatives/Ti3C2Tx MXene hybrids for photocatalytic hydrogen evolution. Dyes and Pigments 2021;194:109583.
[129] Hantanasirisakul K, Gogotsi Y. Electronic and optical properties of 2D transition metal carbides and nitrides (MXenes). Adv Mater 2018;30(52):1804779.
[130] Li W, Zhuang C, Li Y, Gao C, Jiang W, Sun Z, et al. Anchoring ultra-small TiO2 quantum dots onto ultra-thin and large-sized Mxene nanosheets for highly efficient photocatalytic water splitting. Ceram Int 2021;47(15):21769–76.
[131] Wang J, Shen Y, Liu S, Zhang Y. Single 2D MXene precursor-derived TiO2 nanosheets with a uniform decoration of amorphous carbon for enhancing photocatalytic water splitting. Appl Catal B 2020;270:118885.
[132] Kong X, Gao P, Jiang R, Feng J, Yang P, Gai S, et al. Orderly layer-by-layered TiO2/carbon superstructures based on MXene's defect engineering for efficient hydrogen evolution. Appl Catal A 2020;590:117341.
[133] Liu X, Chen C. Mxene enhanced the photocatalytic activity of ZnO nanorods under visible light. Mater Lett 2020;261:127127.
[134] Ai Z, Zhang K, Chang B, Shao Y, Zhang L, Wu Y, et al. Construction of CdS@ Ti3C2@ CoO hierarchical tandem pn heterojunction for boosting photocatalytic hydrogen production in pure water. Chem Eng J 2020;383:123130.
[135] Zhao N, Hu Y, Du J, Liu G, Dong B, Yang Y, et al. Ti3C2Tx MXene-derived amorphous TiO2-C nanosheet cocatalysts coupled CdS nanostructures for enhanced photocatalytic hydrogen evolution. Appl Surf Sci 2020;530:147247.
[136] Qin X, Cao R, Gong W, Luo L, Shi G, Ji L, et al. Hydrothermal growth of ZnCdS/TiO2 nanoparticles on the surface of the Ti3C2 MXene sheet to enhance photocatalytic performance under visible light. J Solid State Chem 2022;306:122750.
[137] Su T, Hood ZD, Naguib M, Bai L, Luo S, Rouleau CM, et al. Monolayer Ti3C2 T x as an effective co-catalyst for enhanced photocatalytic hydrogen production over TiO2. ACS Appl Energy Mater 2019;2(7):4640–51.
[138] Huang K, Li C, Meng X. In-situ construction of ternary Ti3C2 MXene@ TiO2/ZnIn2S4 composites for highly efficient photocatalytic hydrogen evolution. J Colloid Interface Sci 2020;580:669–80.
[139] Ghidiu M, Kota S, Drozd V, Barsoum MW. Pressure-induced shear and interlayer expansion in Ti3C2 MXene in the presence of water. Science advances 2018;4(1):eaao6850.